UNIVERSITÀ DEGLI STUDI DI NAPOLI
FACOLTÀ DI INGEGNERIA

Dipartimento di Ingegneria Elettrica

Tesi di dottorato

A high-precision position measurement instrument for particle accelerator collimators

Coordinatore:
Prof. Guido **Carpinelli**

Relatori:
Prof. Pasquale **Arpaia**

Prof. Massimo **D'Apuzzo**

Co-relatore:
Dott. Ing. Alessandro **Masi**

Candidato:
Ing. Michele **Martino**

ANNO 2011

to my family

Acknowledgments

First I would like to thank all the people I have been working with at CERN for a long and particularly enriching time. They are too many to be all mentioned. With all of them I shared hard work and a lot of fun from time to time. Without them my research would not have been possible at all. A special thank goes to A. Brielmann, M. Butcher, A. Danisi, G. Conte, G. Golluccio, M. Lamberti, R. Losito, R. Picatoste Ruilope, A. Pierno, G. Spiezia and A. Tacchetti, and, particularly, to my CERN supervisor and old friend A. Masi, for sharing with me the burden and the honor of communicating the results achieved in many different international conferences and publishing them in many different journals. I would also like to thank Prof. F. Cennamo and Prof. V.G. Vaccaro I have been working for when my collaboration with CERN started and particularly Prof. N. Polese and Prof. M. D'Apuzzo for their tutorship during my Ph.D. studies. I would also like to express my sincere gratitude to Prof. Pasquale Arpaia. I consider him my scientific mentor; Pasquale, it has been an honor working with you! I am also sincerely thankful to my old and new friends: Mirco, Giovanni, Carlo, Simona, Francesco, Ivan, Marco, Federico, Tatiana, Stefano, and all the others, for their support in this journey.

Contents

List of Figures

List of Tables

Abstract

An innovative high-precision digital instrument for position measurement of particle accelerators collimators is proposed. The instrument relies on Linear Variable Differential Transformers by exploiting the three-parameter sine fit to estimate the amplitudes of their secondary signals.

Moreover, the crucial problem of interfering magnetic fields is analyzed by means of two different models: analytical, aimed at capturing the main physics of the phenomenon, and predictive, based on Finite Elements Method, for assessing the interference effects accurately.

Both the models were validated by means of simulations and experimental tests. They provided a sound basis for defining design guidelines to an application-independent solution of the interference problem.

The experimental validation of the models included the development of a measurement method and a measurement system for the general characterization of external magnetic fields as influence quantities for the position measurement by means of Linear Variable Differential Transformers. Different prototypes were also built and characterized in laboratory.

Preliminary on-field results, gathered during Large Hadron Collider commissioning and operations at the European Organization for Nuclear Research (CERN), confirming the laboratory results and discussed.

1

Therefore, the instrument was qualified as complying with the demanding requirements of Large Hadron Collider at CERN and is currently integrated in its collimators control system.

Introduction

Particle accelerators and, in particular the *LHC* (Large Hadron Collider) at CERN in Geneva [1], are, or are meant to be, birthplaces of new physics discoveries. But they have proven to be, often, birthplaces of new technologies too: the tremendous technical problems arising from their realizations often trigger the development of new technologies or quickly *accelerate* their maturation.

Key components of particle accelerators are the collimators protecting such expensive machines and helping in cleaning the beam in order to let the experiments enter into *physics* [2], [3]. Increasing energy implies increasingly demanding requirements for the collimators. The accuracy required in collimators positioning is no exception; indeed collimators are required to be positioned with increasing accuracy as the dimensions of the beam decrease according to the energy.

Most of the scientific literature on beam collimation addresses physics [4], [5], [6], [7] or material science/engineering [8], [9] issues, whereas little or no attention is paid to the more and more challenging technical issues related to its measurement and actuation systems. This thesis is intended to, partially, fill this gap.

Given the current limitations on the magnetic fields produced even by

the most advanced superconducting magnets, increasing energy means large accelerators: *LHC* is 27 *km* long. Moreover, high energy also means that collimators have the most radiation *activation*, thus no electronics can directly equip them or could reliably operate in their immediate closeness. Measurement and power electronics equipping collimators is put in special alcoves up to 800 *m* far in the case of *LHC* [3]. Radiation-hard, robust, and mature technologies have to be employed for actuating the collimators motion and *sensing* their position.

In particle accelerators all over the world, *LVDTs* (Linear Variables Differential Transformers) have long proven to possess the needed requirements as at *Tevatron* [10] and at *PEP-II* [11], just to cite a few examples. Such constraints, in an environment highly populated by many different devices, make impossible to exert a reasonable control on the *influence quantities* that might jeopardize the accuracy of the collimators' position measurement. Such an environment is expected to be characterized, in principle, by low *SNR* (Signal-to-Noise Ratio), and thus opportune design solutions must be adopted. Moreover, a cost-performance trade-off has to be accepted in the choice of the cable connecting LVDTs to the measurement electronics: multi-wire cables are adopted, thus increasing the risk of cross-talks between different LVDTs signals.

Nevertheless, even exploiting the mature and proven technology of *LVDT*, major new challenges for the position measurement can arise. Indeed an effect barely mentioned in the technical and scientific literature about LVDTs turns out to be critical for collimators in the immediate closeness of trays accommodating cables supplying *quasi-DC* currents to the accelerator pulsed magnets [12], [13]. Such currents produce slowly-varying magnetic fields,

with respect to the operating frequencies of LVDTs, that can significantly *interfere* with the LVDT nominal operation. However this effect, fleetingly mentioned in no more than a couple of datasheets, has never been correctly *characterized* or even *quantified*. Moreover, being such *external* fields pulsed and not purely DC, their effect cannot be corrected by a calibration operated at a given value of the currents. In *LHC* transfer lines, such an interaction resulted in deviations of the measurements, with respect to a condition of pulsed currents absence, up to few hundreds of μm, whereas the target uncertainty at top energy is $\pm 20\ \mu m$ (roughly one tenth of the to- energy beam transversal dimension). The external fields slowly varies with respect to the LVDT's internal fields, thus the *interaction* is not related to the variation of magnetic flux experienced by the sensors, but rather to the field itself.

In this thesis, after a recognition of the state of the art in Chapters 1 - 3, the architecture of an innovative digital position measurement instrument coping with all these issues is presented in Chapter 4. At the heart of the instrument there is the *IEEE Standard 1241* sine fit algorithm. In Chapter 5, an original analytical metrological characterization is proposed, first in a theoretical frame and, then, for the actual multi-channel real-time design of the of LVDTs' secondary voltages amplitude estimator.

Given the novelty of the problem of magnetic field interference on LVDTs or, more specifically, the lack of technical documentation about it, a general approach, comprising measurements, modeling and eventually design guidelines, has been followed. Although measurements, modeling and design are deeply interconnected in an iterative flow, a methodological organization has been operated. The first step consists in modeling the interference: at this aim in Chapter 6, two different models are proposed: *(i)* in Section 6.3, an

analytical simplified model aimed at capturing the main physics of the interaction, including magnetic hysteresis, is presented; and *(ii)* in Section 6.4 a more *quantitative* F.E.M. (Finite Elements Method), and therefore more accurate, model although not able to deal with hysteresis.

An *ad hoc* measurement method has been conceived both to validate the proposed models and to serve as a reference for the characterization of the interference of suitable prototypes and, more generally, commercially available LVDTs; such method is presented in Section 6.5.

Validated models are the base of any successful design; in particular, accurate quantitative models, such the proposed F.E.M. model, are irreplaceable design tools: any idea can be quickly tested in simulation and optimizations or worst-case analysis can be thoroughly simulated before building any prototype. Design guidelines to drastically lessen the *influence* of external magnetic fields on LVDT sensors are outlined in Chapter 7: they consist in an innovative multi-layer magnetic shielding and a tuned DC polarization of the primary circuit of an abstracted LVDT.

Chapter 8 is devoted to the illustration and validation, by simulations, of the analytical results obtained for the amplitude estimator. Simulation results of the accurate F.E.M. model are exploited, in Chapter 9, in order to validate the concept of the *coil equivalent permeability*, which has been introduced in Chapter 6 and is the core of the analytical simplified model of the interference. The F.E.M. model itself is fully characterized in Chapter 10: the nominal characteristics of the sensor together with the deviation of the position measurement as a function of the intensity of the longitudinal external field are simulated, both with voltage and current LVDT primary supplies (assuming, therefore, an idealized behavior of the rest of the instru-

ment). The validation of the proposed design guidelines is developed along Chapter 11 by means of simulations of the F.E.M. model.

The experimental characterization of the proposed amplitude estimator running on the hardware/software layer of the instrument, in laboratory conditions, is developed along Chapter 12. Contextually, the measurement repeatability of the whole instrument equipped with *ratiometric* LVDTs (a high precision type of LVDT [14]) and configured to closely meet the *LHC* conditions was evaluated too.

The measurement method of the magnetic interference on LVDTs has been introduced in Chapter 6; in Chapter 13, the actual system for its measurement, which partially, relies on the software and hardware architecture of the position measurement instrument, is thoroughly described and its metrological performance is characterized. Furthermore, as the proposed method claims to be a reference method for the characterization of the interference of commercially available LVDTs, extensive experimental results are presented for two different types of LVDTs, both for voltage and current supplies, thus potentially different inaccuracies due to external fields can be highlighted. The measurement uncertainty of the proposed system, a few μm, is small enough for the system to be confidently used for the validation of the proposed models. The experimental validation of the F.E.M. model was carried out by means of an *ad hoc* prototype which has been built according to the specifications of the LVDT F.E.M. model and extensively described in Chapter 14. All the simulation conditions described in Chapter 10 were reproduced experimentally. As a figure of merit, the deviation of the position measurement due to the external longitudinal field was considered. Chapter 15 describes the validation of the simplified analytical model. A prototype

LVDT has been built expressly with non annealed magnetic materials, in order to highlight the impact of magnetic hysteresis; the experimental tests aimed at measuring the variation of the coil equivalent permeability of the LVDT secondary coils as a function of the intensity of the longitudinal external field.

In Chapter 16, preliminary *on-field* results are presented summarizing many different tests conducted during *LHC* commissioning and operations, between 2009 and 2011, by the team responsible of machine operation. Such results, which confirm the metrological performance of the instrument presented in Chapter 12, represent an important, third-party validation of the proposed instrument which has been considered to be fully complying with the demanding requirements of *LHC* collimation.

Part I: State of the Art

Chapter 1

Particle Accelerators

1.1 The steps of a particle acceleration process

Particle accelerators exist in many shapes and sizes, but the smallest accelerators share common elements with the larger devices. First, all accelerators must have a source that generates electrically charged particles, electrons or protons, and their antiparticles in the case of larger accelerators. All accelerators must have electric fields to accelerate the particles, and they must have magnetic fields to control the paths of the particles. Also, the particles must travel through a good vacuum, that is, in a container with as little residual air as possible. Finally, all accelerators must have some means of detecting, counting, and measuring the particles after they have been accelerated.

1.1.1 Particles Generation

Electrons and protons, the particles most commonly used in accelerators, are found in all materials, but for an accelerator the appropriate particles must be separated out. Electrons are usually produced in a device known as electron "gun". The gun contains a cathode (negative electrode) in a

vacuum, which is heated and electrons break away from the atoms in the cathode material [1]. The emitted electrons, which are negatively charged, are attracted toward an anode (positive electrode), where they pass through a hole. The gun itself is in effect a simple accelerator, because the electrons move through an electric field, as described below. As with electrons, there are protons in all materials, but only the nuclei of hydrogen atoms consist of single protons, thus hydrogen gas is the source of particles for proton accelerators. In this case the gas is ionized (the electrons and protons are separated in an electric field) and the protons escape through a hole. In large high-energy particle accelerators, protons are often produced initially in the form of negative hydrogen ions. These are hydrogen atoms with an extra electron, which are also formed when the gas, originally in the form of molecules of two atoms, is ionized. Negative hydrogen ions prove easier to handle in the initial stages of large accelerators. They are later passed through thin foils to strip off the electrons before the protons move to the final stage of acceleration [1].

1.1.2 Particles Acceleration

The key feature of any particle accelerator is the accelerating electric field. The simplest example is a uniform static field between positive and negative electric potentials (voltages). In such a field an electron, bearing a negative charge, feels a force that directs it toward the positive potential. This force accelerates the electron, and if there is nothing to impede the electron, its velocity and its energy will increase. Electrons moving toward a positive potential along a wire or even in air will collide with atoms and lose energy, but if the electrons pass through a vacuum, they will accelerate as they move

toward the positive potential. The difference in electric potential between the position where the electron begins moving through the field and the place where it leaves the field determines the energy that the electron acquires. The energy an electron gains in traveling through a potential difference of 1 Volt is known as 1 electron Volt (eV). This is a tiny amount of energy, equivalent to 1.6×10^{-19} Joules. Many particle accelerators reach high energies, measured in Megaelectron Volts (MeV, or million eV), Gigaelectron Volts (GeV, or billion eV), or Teraelectron Volts (TeV, or trillion eV) [1]. A practical realization is to make repeated use of weak electric fields set up by low voltages. This is the principle involved in two common categories of modern particle accelerators: Linear Accelerators (or LINACs) and Cyclic Accelerators.
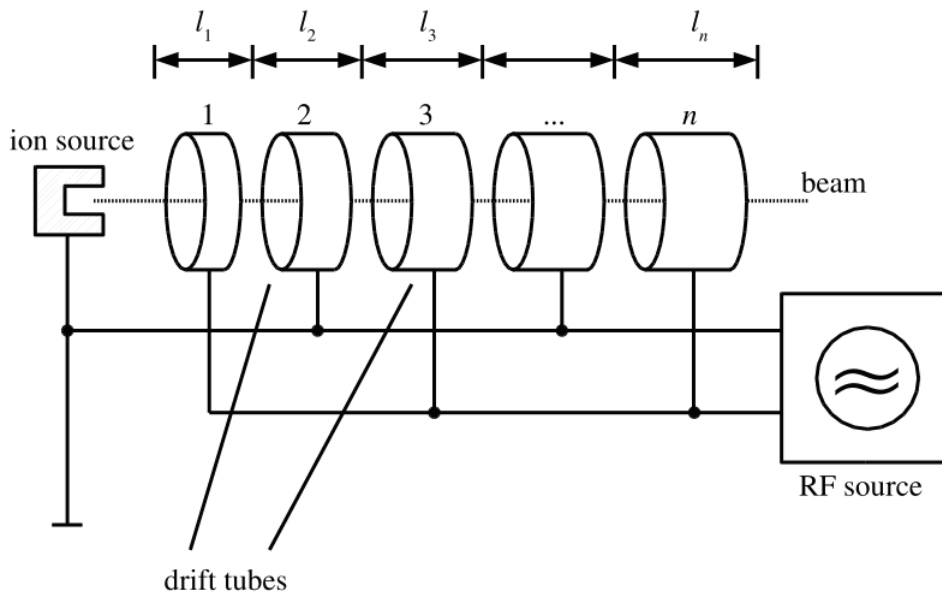
Figure 1.1: Schematic of a Linear Accelerator.

In a linear accelerator, the particles pass once through a sequence of accelerating fields, whereas in a cyclic machine they are guided on a circular

path many times through the same relatively small electric fields. In both cases the final energy of the particles depends on the cumulative effect of the fields as shown in Fig. 1.1. The repetitive structure of a linear accelerator naturally suggests the use of alternating rather than constant voltages to create the electric fields. A positively charged particle accelerated toward a negative potential, for example, will receive a renewed push if the potential becomes positive as the particle passes by. In practice the voltages must change very rapidly. For example, at an energy of 1 MeV a proton is already traveling at very high speeds (46 % of the speed of light) thus it covers a distance of about 1.4 m in 0.01 μs. This implies that in a repeated structure several meters long, the electric fields must alternate (that is, change direction) at a frequency of at least 100 MHz. Both linear and cyclic accelerators generally accelerate particles by using the alternating electric fields present in electromagnetic waves, typically at frequencies from 100 to 3000 MHz, ranging from radiowaves to microwaves. An electromagnetic wave is in effect a combination of oscillating electric and magnetic fields vibrating at right angles to each other. The key with a particle accelerator is to set up the wave in such a way that, when the particles arrive, the electric field is in the direction needed to accelerate the particles. This can be done with a standing wave (a combination of waves moving in opposite directions in an enclosed space). Alternatively, for very fast-moving electrons, which travel very close to the speed of light (in other words, close to the speed of the wave itself), a traveling wave can be used for acceleration [1]. An important effect that comes into play in acceleration in an alternating electric field is that of *phase stability*. If a particle with increasing velocity arrives too soon as the field rises, it will not experience as high a field as it should and thus

will not receive as big a push. However, when it reaches the next region of accelerating fields, it will arrive late and thus will receive a higher field, in other words, too big a push. The net effect will be phase stability, that is, the particle will be kept in phase with the field in each accelerating region. Another effect will be a grouping of the particles in time, in such a way that they will form a train of bunches rather than a continuous beam of particles.

1.1.3   Particles Guide

Magnetic fields also play an important role in particle accelerators, as they can change the direction of charged particles, according to the Lorentz's force:

$$\tilde{\mathbf{F}} = q\tilde{\mathbf{E}} + q\tilde{\mathbf{v}} \times \tilde{\mathbf{B}} \tag{1.1}$$

where $\tilde{\mathbf{B}}$ is the magnetic flux density, q is the charge, $\tilde{\mathbf{v}}$ the speed and $\tilde{\mathbf{E}}$ the electric field. This means that they can be used to *bend* particle beams around a circular path in order to pass repeatedly through the same accelerating regions. In the simplest case a charged particle moving in a direction at right angles to the direction of a uniform magnetic field feels a force at right angles both to the particle's direction and to the field. The effect of this force is to make the particle move on a circular path, perpendicular to the field, until it leaves the region of magnetic force or another force acts upon it. This effect comes into play in cyclic accelerators such as *cyclotrons* and *synchrotrons*.

A second important function of electromagnets in particle accelerators is to focus the particle beams in order to keep them as narrow and intense as possible. The simplest form of focusing magnet is a quadrupole, a magnet built with four poles (two norths and two souths) arranged opposite each

other. This arrangement pushes particles toward the center in one direction but allows them to spread in the perpendicular direction. A quadrupole designed to focus a beam horizontally, therefore, will let the beam go out of focus vertically. In order to provide proper focusing, quadrupole magnets must be used in pairs, each member arranged to have the opposite effect as shown in Fig. 1.3. More-complex magnets with larger numbers of poles (sextupoles and octupoles) are also used for more-sophisticated focusing. As the energy of the circulating particles increases, the strength of the magnetic field guiding them is increased, which thus keeps the particles on the same path. A *pulse* of particles is injected into the ring and accelerated to the desired energy before it is extracted and delivered to experiments. Extraction is usually achieved by *kicker* magnets, electromagnets that switch on just long enough to *kick* the particles out of the synchrotron ring and along a beam line. The fields in the dipole magnets are then ramped down, and the machine is ready to receive its next pulse of particles.

1.1.4 Particles Collision

Most of the particle accelerators used in medicine and industry produce a beam of particles for a specific purpose, for example, for radiation therapy or ion implantation. This means that the particles are used once and then discarded. For many years the same was true for accelerators used in particle physics research. However, in the 1970s, rings where two beams of particles circulate in opposite directions and collide on each circuit of the machine were developed. A major advantage of such machines is that when two beams collide head-on, the energy of the particles goes directly into the energy of the interactions between them. This contrasts with what happens when an

energetic beam collides with material at rest: in this case much of the energy is lost in setting the target material in motion, in accord with the principle of conservation of momentum [1]. Some colliding-beam machines have been built with two rings that cross at two or more positions, with beams of the same kind circulating in opposite directions. More common yet have been particle-antiparticle colliders. An antiparticle has opposite electric charge to its related particle. For example, an antielectron (or positron) has positive charge, while the electron has negative charge. This means that an electric field that accelerates an electron will decelerate a positron moving in the same direction as the electron. But if the positron is traveling through the field in the opposite direction, it will feel an opposite force and will be accelerated. Similarly, an electron moving through a magnetic field will be bent in one direction (left, say) while a positron moving the same way will be bent in the opposite direction (to the right). If, however, the positron moves through the magnetic field in the opposite direction to the electron, its path will still bend to the right, but along the same curve taken by the leftward-bending electron. Taken together, these effects mean that an antielectron can travel around a synchrotron ring guided by the same magnets and accelerated by the same electric fields that affect an electron traveling the opposite way. Many of the highest-energy colliding-beam machines have been particle-antiparticle colliders, as only one accelerator ring is needed.

As already pointed out, the beam in a synchrotron is not a continuous stream of particles but is clustered into *bunches*. A bunch may be a few centimeters long and a tenth of a millimeter across, and it may contain about 10^{12} particles, the actual numbers depending on the specific machine. However, this is not very dense; normal matter of similar dimensions contains

about 10^{23} atoms. Thus when particle beams, or, more accurately, particle bunches, cross in a colliding-beam machine, there is only a small chance that two particles will interact. In practice the bunches can continue around the ring and intersect again. To enable this repeated beam crossing, the vacuum in the rings of colliding-beam machines must be particularly good for the particles to circulate for many hours without being lost through collisions with residual air molecules. The rings are therefore also referred to as storage rings, as the particle beams are in effect stored within them for several hours.
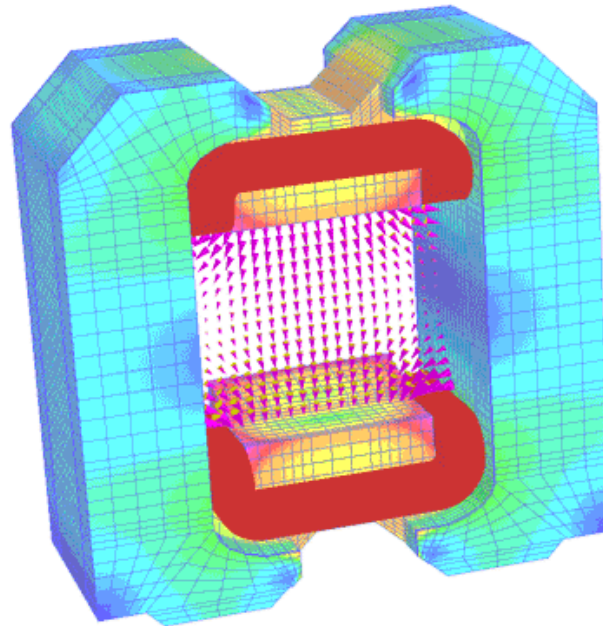
(a) Dipole Magnet.
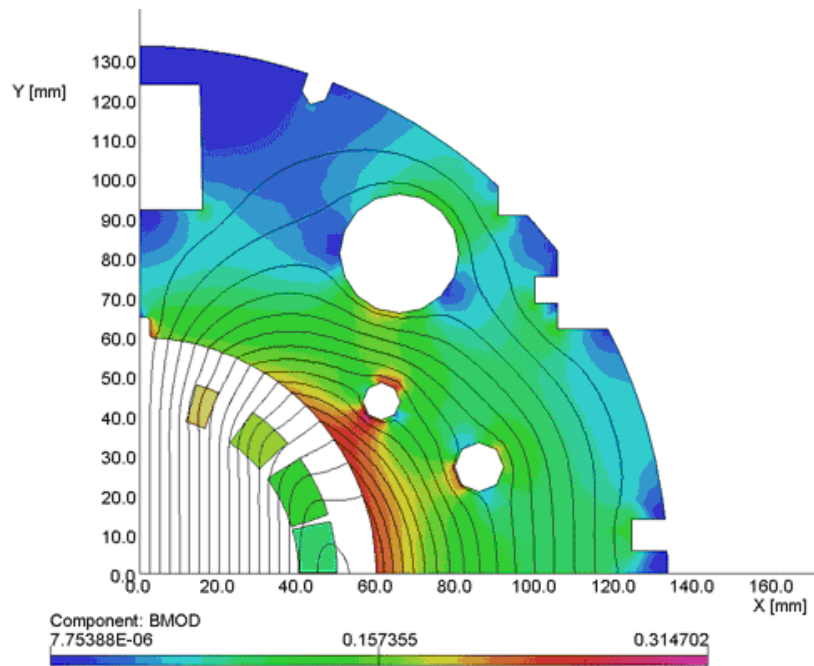
(b) Synchrotron Bending Magnet

Figure 1.2: Magnetic fields configuration for different types of magnets: (a) flux density levels and field distribution in a dipole magnet, (b) flux density and lines in a synchrotron bending magnet.
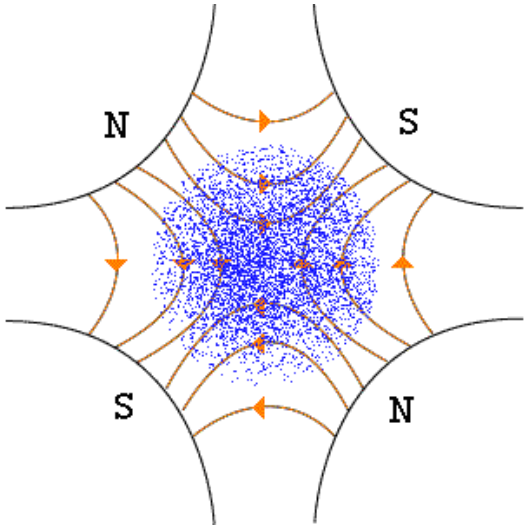
(a) Single Focusing.
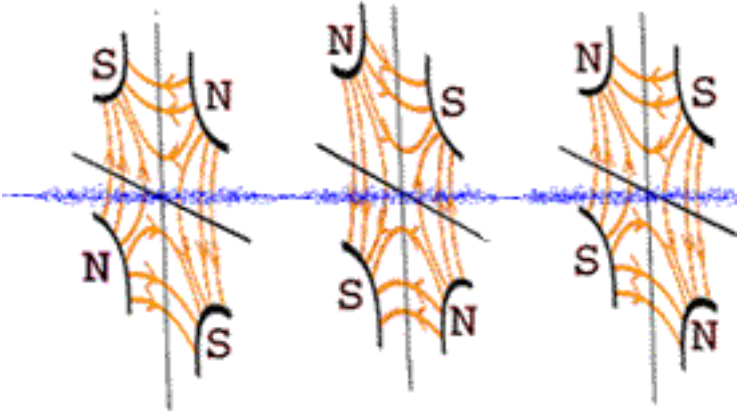
(b) Focusing Defocusing.

Figure 1.3: Quadrupoles Magnets.: (a) Focusing, (b) Focusing Defocusing Strategy.
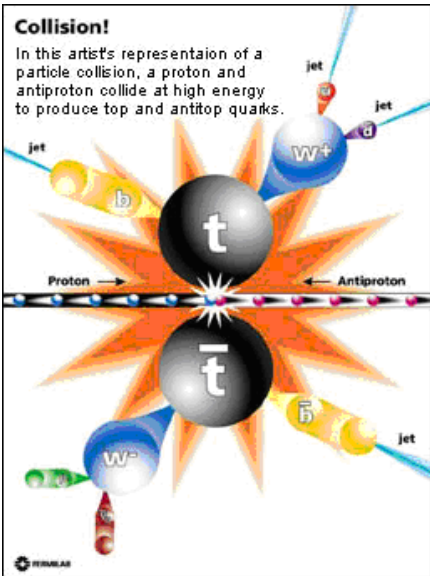
(a)
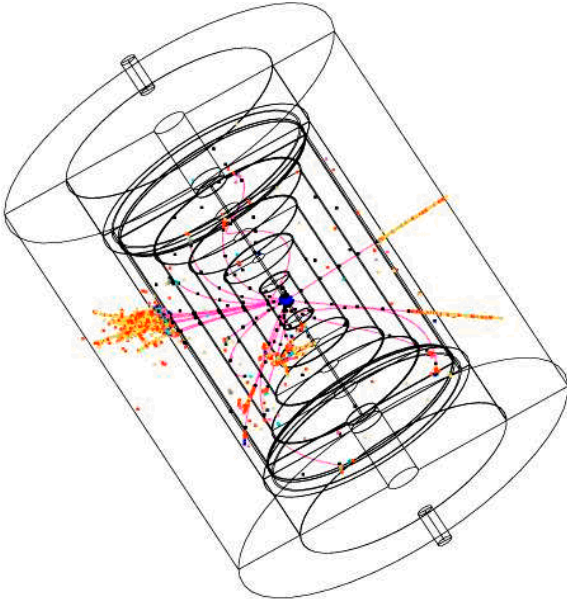
(b)

Figure 1.4: Collisions: (a) Pictorial representation of a collision, (b) Simulation at ILC detector of the signature of a neutralino.

1.2   Circular Accelerators

In the circular accelerator, particles move in a circle until they reach sufficient energy. As already said before, the particle track is typically bent into a circle using electromagnets. The advantage of circular accelerators over linear accelerators is that the ring topology allows continuous acceleration, as the particle can transit indefinitely. Another advantage is that a circular accelerator is relatively smaller than a linear accelerator of comparable power (a LINAC would have to be extremely long to have the equivalent power of a circular accelerator). Depending on the energy and the particle being accelerated, circular accelerators suffer a disadvantage in that the particles emit synchrotron radiation. When any charged particle is accelerated, it emits electromagnetic radiation and secondary emissions. As a particle traveling in a circle is always accelerating towards the center of the circle, it continuously radiates towards the tangent of the circle. This radiation is called synchrotron light and depends highly on the mass of the accelerating particle. For this reason, many high energy electron accelerators are LINACs. Since the special theory of relativity requires that matter always travels slower than the speed of light in a vacuum, in high-energy accelerators, as the energy increases the particle speed approaches the speed of light as a limit, never quite attained. Therefore particle physicists do not generally think in terms of speed, but rather in terms of a particle's energy, in electron volts (eV). An important principle for circular accelerators, and particle beams in general, is that the curvature (inverse of the curvature radius) of the particle trajectory is proportional to the particle charge and to the magnetic field, but inversely proportional to the (typically relativistic) momentum.

$$\frac{1}{R} \propto \frac{qB}{p} \qquad (1.2)$$

The equilibrium expression results in the following expression:

$$E = q \cdot B \cdot c \cdot R \qquad (1.3)$$

where E is is the energy of a particle of charge q, B is the bending field of the magnets (modulus), R is the bending radius of the circular accelerator, and c is the speed of light.

1.2.1 Synchrotrons

A synchrotron is an accelerator in which the particles are accelerated in a ring of constant radius. As already said, since the particle momentum increases during acceleration, it is necessary to turn up the magnetic field B in proportion to maintain constant curvature of the orbit. In consequence synchrotrons cannot accelerate particles continuously, but must operate cyclically, supplying particles in bunches, which are delivered to a target or an external beam in beam "spills" typically every few seconds. Since high energy synchrotrons do most of their work on particles that are already traveling at nearly the speed of light c, the time to complete one orbit of the ring is nearly constant, as is the frequency of the RF cavity resonators used to drive the acceleration. Note also a further point about modern synchrotrons: because the beam aperture is small and the magnetic field does not cover the entire area of the particle orbit, several necessary functions can be separated. Instead of one huge magnet, one has a line of hundreds of bending magnets, enclosing (or enclosed by) vacuum connecting pipes. The focusing of the beam

is handled independently by specialized quadrupole magnets, while the acceleration itself is accomplished in separate RF sections, rather similar to short linear accelerators. Also, there is no necessity that cyclic machines be circular, but rather the beam pipe may have straight sections between magnets where beams may collide. More complex modern synchrotrons such as the *Tevatron*, *LEP*, and *LHC* may deliver the particle bunches into storage rings of magnets with constant B, where they can continue to orbit for long periods for experimentation or further acceleration.
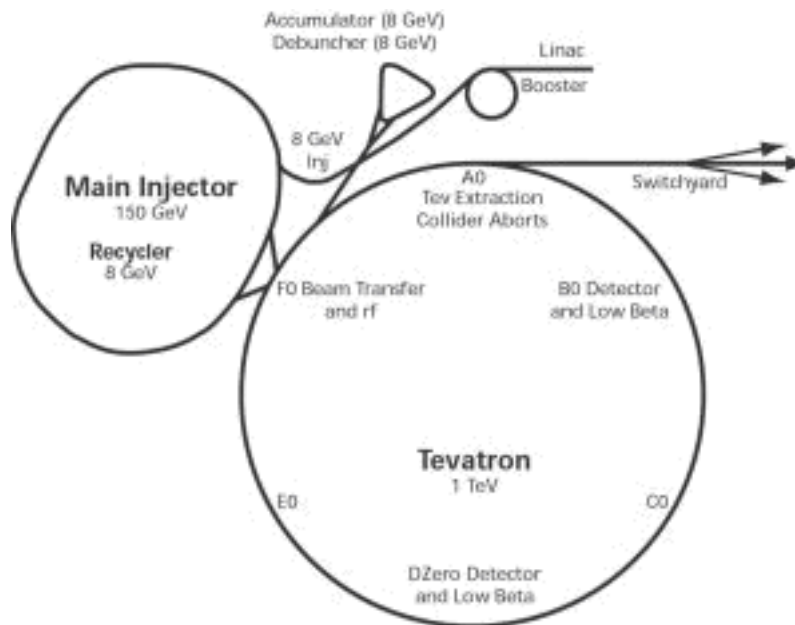
Figure 1.5: The Fermilab's *Tevatron* synchrotron.

The highest-energy machines such as the *Tevatron* and *LHC* are actually accelerator complexes, with a cascade of specialized elements in series, including linear accelerators for initial beam creation, one or more low energy synchrotrons to reach intermediate energy, storage rings where beams can be accumulated or *cooled* (reducing the magnet aperture required and permitting tighter focusing), and a last large ring for final acceleration and

experimentation.

1.3   The Large Hadron Collider

The Large Hadron Collider (*LHC*) is an example of circular particle accelerator. It has been built by the European Organization for Nuclear Research (CERN) near Geneva, across the Swiss-France border. The *LHC* has been completed on July 2008 and tested for the first time on September, 10, 2008 with its first circulating beam [15].

Figure 1.6: Overview of the Geneva area with superposed the track of the *LHC*.

1.3.1   Purpose

It is theorized that the collider will produce the elusive Higgs boson, the last unobserved particle among those predicted by the Standard Model. The

verification of the existence of the Higgs boson would also explain the mechanism of electroweak symmetry breaking, through which the particles of the Standard Model are thought to acquire their mass. In addition to the Higgs boson, new particles predicted by possible extensions of the Standard Model might be produced at the *LHC* [1]. The *LHC* physics program is mainly based on proton-proton collisions. However, shorter running periods, typically one month per year, with heavy-ion collisions are included in the program. While lighter ions are considered as well, the baseline scheme deals with lead ions. This will allow an advancement in the experimental program currently in progress at the Relativistic Heavy Ion Collider (*RHIC*). The aim of the heavy-ion program is to provide a window on a state of matter known as Quark-gluon plasma, which characterized the early stage of the life of the Universe.

1.3.2 LHC Project

The *LHC* is the world's largest and highest-energy particle accelerator. The collider is contained in a circular tunnel, with a circumference of 27 kilometers, at a depth ranging from 50 to 175 meters underground [15].

The 3.8 *m* wide concrete-lined tunnel, constructed between 1983 and 1988, was formerly used to house the Large Electron-Positron Collider (*LEP*). It crosses the border between Switzerland and France at four points, with most of it in France. Surface buildings hold ancillary equipment such as compressors, ventilation equipment, control electronics and refrigeration plants [1]. The collider tunnel contains two adjacent parallel beam pipes that intersect at four points, each containing a proton beam, which travel in opposite directions around the ring. Some 1232 dipole magnets keep the beams on
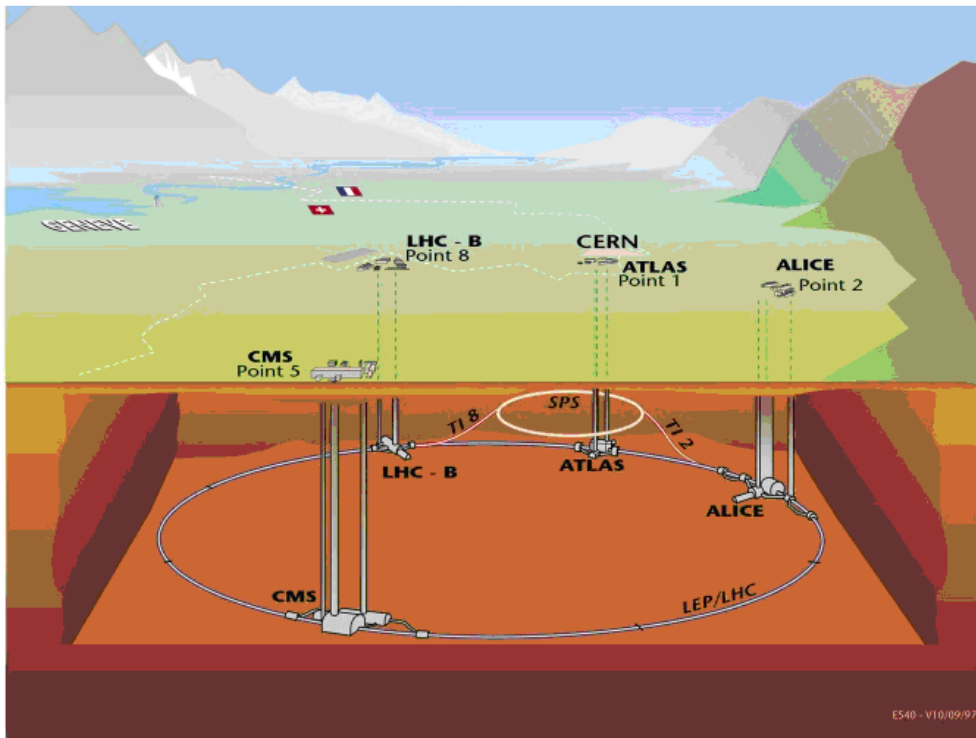
Figure 1.7: Overall view of the LHC and its experiments.

their circular path, while an additional 392 quadrupole magnets are used to keep the beams focused, in order to maximize the chances of interaction between the particles in the four intersection points, where the two beams will cross. In total, over 1600 superconducting magnets are installed, with most weighing over 27 tons. The technical data regarding the dipole magnets are summarized in Tab. 1.1. Approximately 96 tons of liquid helium are needed to keep the magnets at their operating temperature, making the LHC the largest cryogenic facility in the world at liquid helium temperature. Superconducting quadrupole electromagnets are used to direct the beams to four intersection points, where interactions between protons will take place.

Once or twice a day, as the protons are accelerated from 450 GeV to 7 TeV, the field of the superconducting dipole magnets will be increased

Magnetic Length	14.3 m
Operating Temperature	1.9 K
Current at injection (0.45 TeV)	739 A
Bending radius	2803.928 m
Number of beams per magnet	2
Nominal current	11850 A
Bending angle per magnet	5.1000 $mrad$
Peak field in coil	8.76 T
Field at injection	0.535 T
Field at 7 TeV	8.33 T
Inductance per magnet	0.108 H
Mass of cold mass	23800 kg

Table 1.1: Dipole magnets general data.

from 0.54 to 8.3 Tesla (T). The protons will each have an energy of 7 TeV, giving a total collision energy of 14 TeV. At this energy the protons have a Lorentz factor of about 7500, as defined by the following equation, and move at about 99.9999991 % of the speed of light.

$$\gamma = \frac{c}{\sqrt{c^2 - u^2}} = \frac{1}{\sqrt{1 - \beta^2}} = \frac{dt}{d\tau} \tag{1.4}$$

In (1.4) $\beta = u/c$ is the velocity in terms of the speed of light, u is the velocity as observed in the reference frame where time t is measured,τ is the proper time, and c is the speed of light.

It will take less than 90 μs for a proton to travel once around the main ring (a frequency of about 11000 revolutions per second). Rather than continuous beams, the protons will be bunched together, into 2808 bunches, thus interactions between the two beams will take place at discrete intervals never shorter than 25ns.

Prior to being injected into the main accelerator, the particles are pre-
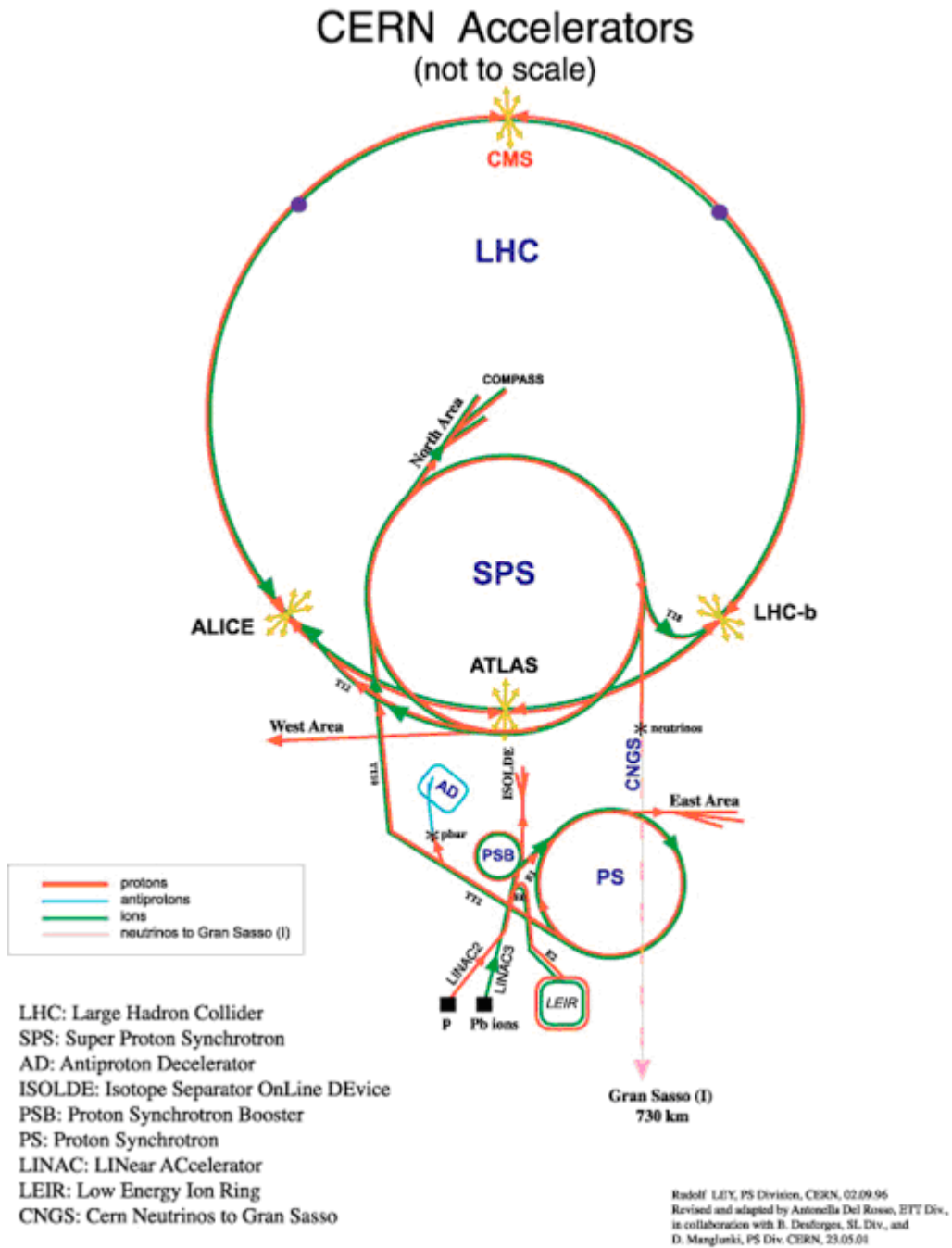
Figure 1.8: Acceleration systems for the *LHC* preliminary acceleration.

pared by a series of systems that successively increase their energy, as depicted in Fig. 1.8. The first system is the linear particle accelerator *LINAC*

2 generating 50 MeV protons, which feeds the Proton Synchrotron Booster (PSB). There the protons are accelerated to 1.4 GeV and injected into the Proton Synchrotron (PS), where they are accelerated to 26 GeV. Finally the Super Proton Synchrotron (SPS) is used to further increase their energy to 450 GeV before they are at last injected (over a period of 20 minutes) into the main ring [15]. Here the proton bunches are accumulated, accelerated (over a period of 20 minutes) to their peak 7 TeV energy, and finally circulated for 10 to 24 hours while collisions occur at the four intersection points. The general technical data are summarized in Tab. 1.2

Maximum kinetic of a proton	7 TeV
Strength of dipole magnets	8.33 T
Number of particles per bunch	1.1×10^{11}
Circulating current per beam	0.54 A
RMS bunch length	7.5 cm
Bunch spacing	25 ns
Tunnel circumference	27 km
Number of bunches around ring	2808
Number of dipole magnets	1232
Length of each dipole magnets	14.3 m
Maximum proton velocity	$0.99999991c$
Injection Energy	450 GeV
Energy loss per turn	6.7 keV

Table 1.2: General technical data for the Large Hadron Collider.

The LHC will also be used to collide lead (Pb) heavy ions. The Pb ions will be first accelerated by the linear accelerator $LINAC$ 3, and the Low-Energy Injector Ring ($LEIR$) will be used as an ion storage and cooler unit. The ions then will be further accelerated by the PS and SPS before being injected into LHC ring, where they will reach an energy of 2.76 TeV per nucleon.

1.3.3 LHC Detectors

Six detectors have been constructed at the *LHC*, located underground in large caverns excavated at the *LHC*'s intersection points. Two of them, the *ATLAS* experiment and the Compact Muon Solenoid (*CMS*), are large, general purpose particle detectors. A Large Ion Collider Experiment (*ALICE*) and *LHCb* have more specific roles and the last two *TOTEM* and *LHCf* are very much smaller and are for very specialized research.
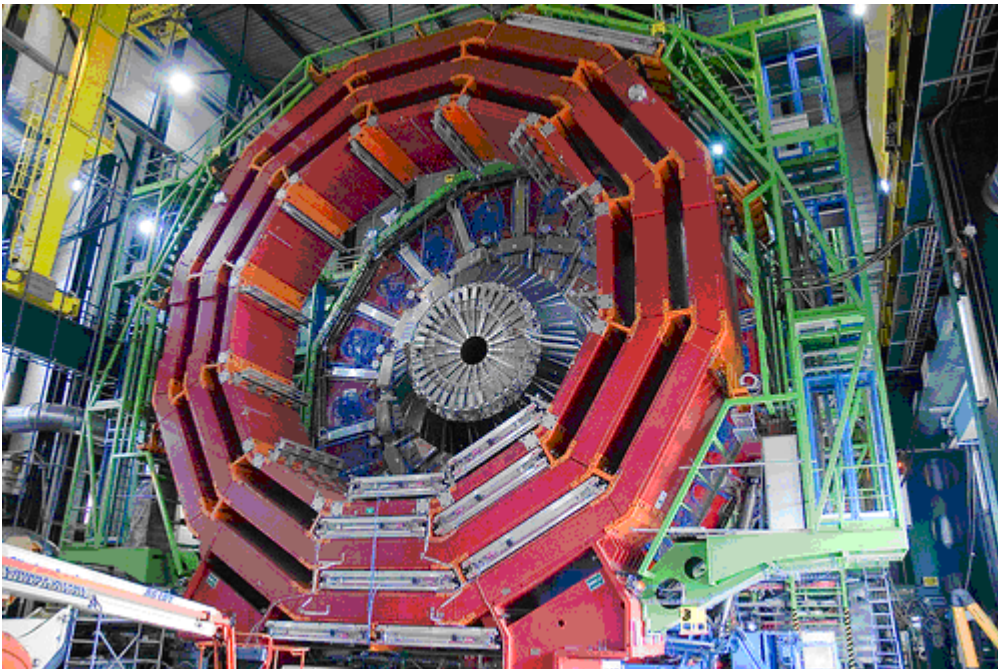
Figure 1.9: The CERN Compact Muon Solenoid detector (*CMS*).

ATLAS is one of two so-called general purpose detectors. *ATLAS* will be used to look for signs of new physics, including the origins of mass and extra dimensions. *CMS* is the other general purpose detector will, like *ATLAS*, hunt for the Higgs boson and look for clues to the nature of dark matter. *ALICE* will study a *liquid* form of matter called quark-gluon plasma that existed shortly after the Big Bang. Equal amounts of matter and anti-matter

were created in the Big Bang. *LHCb* will try to investigate what happened to the *missing* anti-matter.

1.3.4   Future Upgrades

After some years of running, any particle physics experiment typically begins to suffer from diminishing returns; each additional year of operation discovers less than the year before. The way around the diminishing returns is to upgrade the experiment, either in energy or in luminosity. Luminosity is defined by:

$$L = \frac{N_1 \cdot N_2}{4\pi \cdot \sigma_x \cdot \sigma_y \cdot n \cdot f_{rev}} \tag{1.5}$$

where N_1 and N_2 are the number of particles per bunch for each beam, σ_x and σ_y are the beam sizes in the transverse cross-section, n is the number of bunches in each beam, f_{rev} the revolution frequency.

A luminosity upgrade of the *LHC*, called the Super *LHC*, has been proposed, to be made after ten years of *LHC* operation. The optimal path for the *LHC* luminosity upgrade includes an increase in the beam current (i.e., the number of protons in the beams) and the modification of the two high-luminosity interaction regions, *ATLAS* and *CMS*. To achieve these increases, the energy of the beams at the point that they are injected into the (Super) *LHC* should also be increased to 1 *TeV*. This will require an upgrade of the full pre-injector system, the needed changes in the Super Proton Synchrotron being the most expensive. The size of the *LHC* constitutes an exceptional engineering challenge with unique operational issues on account of the huge energy stored in the magnets and the beams. While operating, the total energy stored in the magnets is 10 *GJ* (equivalent to one and a half barrels

of oil or 2.4 tons of TNT) and the total energy carried by the two beams reaches 724 MJ (about a tenth of a barrel of oil, or half a lightning bolt). Loss of only one ten-millionth part (10^{-7}) of the beam is sufficient to quench a superconducting magnet, while the beam dump must absorb 362 MJ, an energy equivalent to that of burning eight kilograms of oil, for each of the two beams. These immense energies are even more impressive considering how little matter is carrying it: under nominal operating conditions (2.808 bunches per beam, 1.1×10^{11} protons per bunch), the beam pipes contain 1.0×10^{-9} gram of hydrogen, which, in standard conditions for temperature and pressure, would fill the volume of one grain of fine sand.

Chapter 2

Collimators' Positioning Systems

In hadron colliders, as in any other accelerator, the creation of beam halo is unavoidable. This happens because of beam-gas interactions, intra-beam scattering, proton-proton (antiproton) collisions in the interaction points IP, and particle diffusion due to RF noise, ground motion and resonances excited by the accelerator magnet nonlinearities and power supplies ripple. As a result of halo interactions with limiting apertures, hadronic and electromagnetic showers are induced in accelerator and detector components causing numerous deleterious effects ranging from minor to severe. An accidental beam loss caused by an unsynchronized abort launched at abort system malfunction can cause catastrophic damage to the collider equipment [10]. Only with a very efficient beam collimation system can one reduce uncontrolled beam losses in the machine to an allowable level. Beam collimation is mandatory at any superconducting, SC, hadron collider to protect components against excessive irradiation, minimize backgrounds in the experiments, maintain operational reliability over the life of the machine (quench stability among other things), and reduce the impact of radiation on the environment [10].

It provides:

- reduction of beam loss in the vicinity of IPs (Interaction Points) to sustain favorable experimental conditions;

- minimization of radiation impact on personnel and the environment by localizing beam loss in the predetermined regions and using appropriate shielding in these regions;

- protection of accelerator components against irradiation caused by operational beam loss and enhancement of reliability of the machine;

- prevention of quenching of SC (Super-Conducting) magnets and protection of other machine components from unpredictable abort and injection kicker prefires/misfires and unsynchronized aborts.

2.1 LHC Collimation System

In the particular case of the Large Hadron Collider, each of the two rings handles a stored beam energy of up to 350 MJ (3×10^{14} protons at 7 TeV). Comparing transverse energy densities, LHC advances the state of the art by even three orders of magnitude, from 1 MJ/mm^2 to 1 GJ/mm^2. This makes the LHC beams highly destructive [16]. At the same time the superconducting magnets in the LHC would quench at 7 TeV if small amounts of energy (on the level of 30 mJ/cm^3, induced by a local transient loss of 4×10^7 protons) are deposited into the superconducting magnet coils. Any significant beam loss into the cold aperture must therefore be avoided. However, beam losses cannot be completely suppressed. A so-called *primary beam halo* will continuously be filled by various beam dynamics processes and the beam
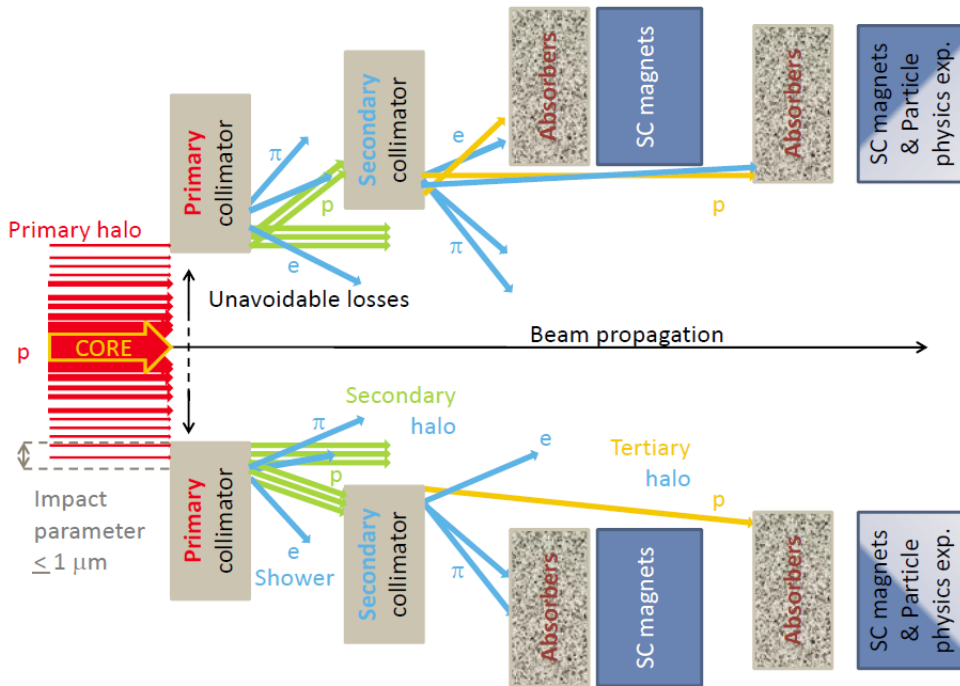
Figure 2.1: Example of Multi Stage Collimation [4]

current lifetime will be finite. The handling of the high intensity LHC beams and the associated high loss rates of protons requires a powerful collimation system with the following functionalities [17]:

- efficient cleaning of the beam halo during the full LHC beam cycle, such that beam-induced quenches of the super-conducting magnets are avoided during routine operation;

- minimization of halo-induced backgrounds in the particle physics experiments;

- passive protection of the machine aperture against abnormal beam loss. Beam loss monitors at the collimators detect any unusually high loss rates and generate a beam abort trigger;

- scraping of beam tails and diagnostics of halo population;

- abort gap cleaning in order to avoid spurious quenches after normal beam dumps.

The collimators are sufficiently robust to fulfill these tasks without being damaged both during normal and abnormal operational conditions. Nevertheless the collimators can only resist a small fraction of the *LHC* beam.

2.1.1 Collimators Main Physical Features

The maximum beam load that is expected on the collimators has been estimated in order to make an appropriate design. Experience from operating accelerators has shown that beam losses are always higher than the theoretical optimum. Real-world beam losses are driven by imperfections, operational problems, unexpected beam physics processes, technical components operating out of specification, human errors and failures of equipment. Based on these estimates the required cleaning efficiency has been derived and a few main features for the layout of the collimation system are summarized.

2.1.1.1 Maximum collimator beam load

Beam impact at the collimators is divided into normal and abnormal processes. Normal proton losses can occur due to beam dynamics (particle diffusion, scattering processes, instabilities) or operational variations (orbit, tune, chromaticity changes, squeeze, collision). These losses must be minimized but cannot be avoided completely. Abnormal losses result from failure or irregular behavior of accelerator components. The design of the collimation system relies on the specified normal and abnormal operational conditions and when these conditions are met the collimation system works

correctly and its components are not damaged. It is foreseen that the beams are dumped when the proton loss rates exceed the specified maximum rates.

Mode	T [s]	τ [h]	R_{loss} [p/s]	P_{loss} [kW]
Injection (min)	cont	1.0	0.8×10^{11}	6
Injection (max)	10	0.1	8.6×10^{11}	63
Ramp	≈ 1	0.006	1.6×10^{13}	1200
Top energy (min)	cont	1.0	0.8×10^{11}	97
Top energy (max)	10	0.2	4.3×10^{11}	487

Table 2.1: Specified minimum beam lifetimes τ, their duration T, the proton loss rate R_{loss}, and maximum power deposition P_{loss} in the cleaning insertion.

Based also on the experience with other accelerators, it has been estimated that the beam lifetime during a fill of the LHC will sometimes drop substantially below the normal value. The collimation system is able to handle increased particle losses, in order to avoid beam aborts and to allow correction of parameters and restoration of nominal conditions [17]. In particular, the range of acceptable lifetime allows commissioning of the machine and performance tuning in nominal running. For periods of up to 10 s beam lifetimes of 0.1 h (injection) and 0.2 h (top energy) are accepted. The peak loss rate at injection energy occurs at the start of the ramp with an expected beam lifetime of 20 s for the first second of the ramp. For continuous losses a minimum possible lifetime of 1 h has been specified for injection and top energy. In Tab. 2.1 are summarized the specified lifetimes and the corresponding maximum power deposition in the cleaning insertion. The collimators are able to withstand the specified beam load. At injection the protons impact on the material at a few μm from the collimator edge. At 7 TeV this transverse impact parameter can be as small as a few hundred nanometer [17]. Low beam lifetimes can occur due to orbit and optics

changes, e.g. during injection, start of ramp, or squeeze. Proton losses can therefore occur locally at a single collimator jaw, where they develop into nuclear showers. The lost energy is only to a small extent dissipated in the jaw itself; the downstream elements and the surrounding materials absorb most of the proton energy. As far as the abnormal proton losses are concerned, much effort has been invested into a powerful LHC machine protection system, designed to handle equipment failures. Primary proton losses will occur at the collimators when they are at nominal positions. The beam loss at the jaws is continuously monitored with fast Beam Loss Monitors. In case an abnormal increase of beam loss signal is detected, a beam abort is initiated and will be completed within 2-3 turns ($178 - 267 \ \mu s$). The beam is dumped before it can damage any accelerator components, including the collimators. The reliability of this process must be very high. Here it is assumed that in case of equipment failure the disturbed beam will always end up in the beam dump. However, this machine protection philosophy does not protect against single turn problems like irregularities of the beam dump itself and abnormally injected beam [16]. For these fast losses any jaw can be hit, because the primary collimators only cover one phase space location and the overall LHC tune will vary. The collimator hardware has been designed to withstand the beam impact during abnormal proton losses without damage.

2.1.2 Collimators Mechanical Features

The mechanical design of collimators that can withstand the high intensity LHC beam has been a hard task. Collimators do not only need to be very robust but at the same time quite long (high energy protons) and very precise (small collimation gaps). The small minimum gap size of 0.5 mm and the

small beam size at the collimators (200 μm rms) implies tight mechanical tolerances. These are relaxed for initial running. For beam-based alignment the jaws (*jaws* are blocks (one or two) made up of Graphite (C) or Carbon-Carbon (C-C) which have to be positioned close the beam in order to absorb energetic particles) are remotely movable with high precision and positioned with low uncertainty of 20 μm. Reproducibility of settings is crucial in order to avoid lengthy re-optimizations. The absolute opening of the collimator gap is safety-critical and must be known at all times with good accuracy. A movement orthogonal to the collimation plane allows provision of spare surface, e.g. after coating has been locally damaged by the beam.

2.1.2.1 Technical layout

The present technical layout (Fig. 2.2) is the result of the analysis of a wide spectrum of options and alternatives; the guiding principle for the mechanical design has been the use and optimization of proven technologies, mainly drawn from *LEP* collimator experience. However, due to the unprecedented specification, it was also necessary to make use of innovative technologies and novel materials, such as Carbon/Carbon composites. The main technical features of the *LHC* secondary collimators are [15]:

1. An internal alignment system allowing both lateral displacement and angular adjustment.

2. A jaw clamping system to ensure good thermal conductance and free thermal expansion.

3. An efficient cooling system.

4. A plug-in external alignment system, allowing a quick and simple positioning of the collimator assembly in the machine.

5. A precise actuation system including a semi-automatic mechanical return and a misalignment prevention device.

6. A motorization and a control set.
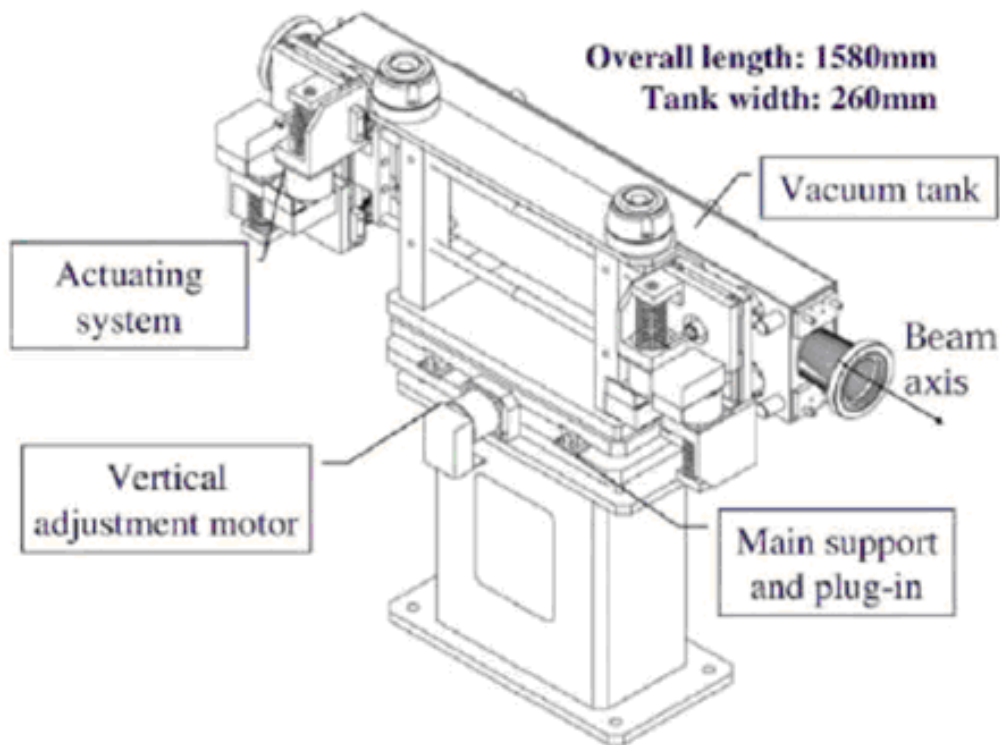
Figure 2.2: Layout of a *LHC* secondary collimator (vertical configuration).

The system is free from the effect of vacuum force.

2.1.2.2 The jaw assembly

The jaw assembly is held together by steel plates (Fig. 2.3). To minimize the thermal path from the hottest spot, where the beam impact takes place, to

the cooling pipes, the jaw width has been reduced to an allowable minimum (25 mm), as demanded by preliminary thermo-mechanical analysis. Since the thermal expansion coefficient of copper is three times (or more) larger than graphite's, a fixed joint between the jaw and the copper plate is not possible, if one wants to avoid unacceptable distortions; hence, the contact must allow for relative sliding between the two surfaces. At the same time, to ensure proper heat conduction at the contact interface, a certain pressure has to be applied between these surfaces.
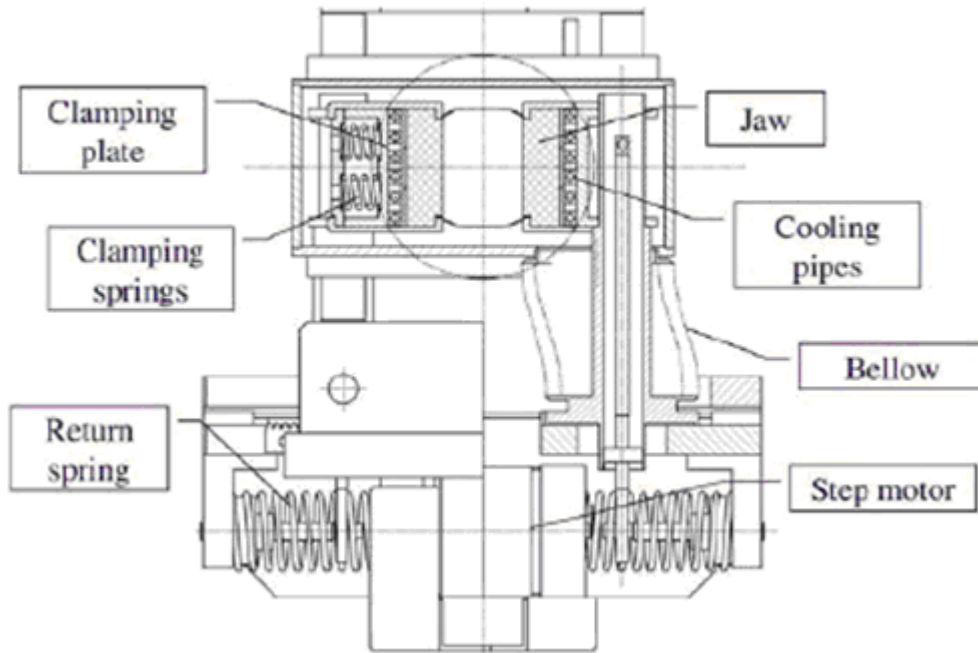
Figure 2.3: Mechanical assembly of an *LHC* secondary collimator

A higher pressure leads to better conductance, but, in turn, it means higher mechanical stresses on the jaw. Therefore a trade-off has been found: the nominal pressure on the interface is set to 500 kPa (5 bar). To minimize the effect of differential thermal expansion on the jaw surface precision, the transverse distance from the two supporting axles to the internal reference

surface of the jaw has been fixed to 40 mm.

2.1.2.3 Motorization and actuation system

Each jaw is independently actuated by two stepper-motors (Fig. 2.4). This allows both lateral displacement (with a nominal stroke of 30 mm plus 5 mm of extra-stroke) and angular adjustment. Excessive tilt of the jaw is prevented by a rack and pinion system which avoids relative deviation between the two axes larger than 2 mm (i.e. 2 $mrad$).
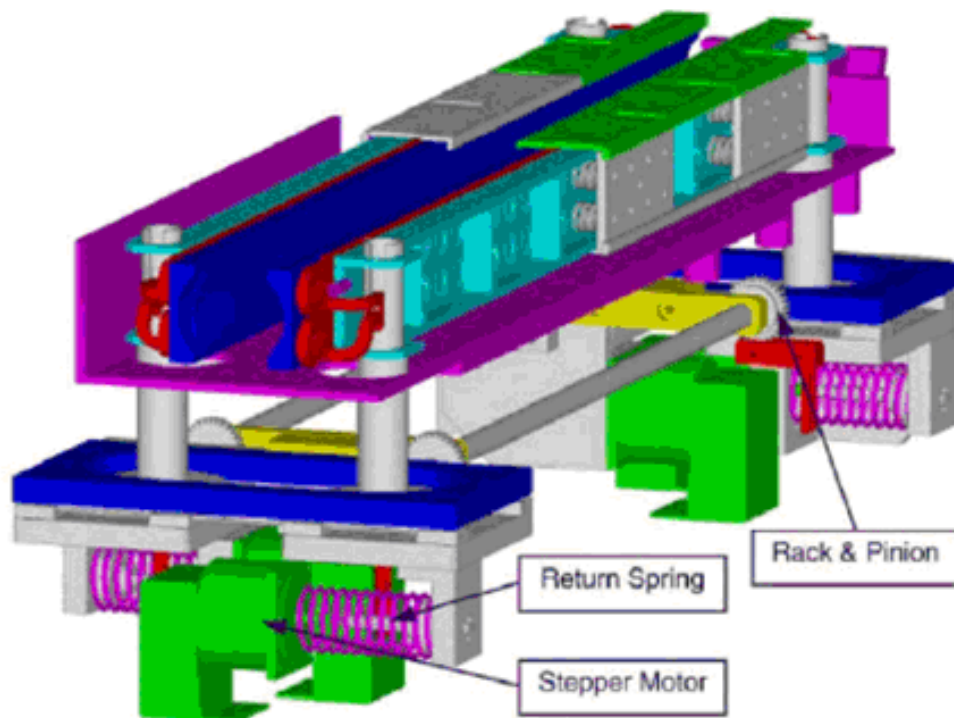
Figure 2.4: *LHC* Collimator's Motorization and Actuation System.

Each motor directly drives, via a roller screw/nut set, a table which allows the precise positioning of the jaw supporting axle. Each table is mounted on anti-friction linear guide-ways. The advancement for each motor step is 5 μm (in half step mode). The system is preloaded by a return spring to

make the system play-free. The return spring also ensures a semi-automatic back-driving of the jaw in case of motor failure. Stops and anti-collision devices for jaw motion are also foreseen.

2.1.2.4 The vacuum tank and the external alignment system

The vacuum tank has a traditional conception. It is manufactured in AISI $316L$ stainless steel and mainly electron-beam welded. The structural design is the same for all the collimator configurations (horizontal, vertical or skew). The tank is supported by brackets whose design depends upon the orientation. The whole system is pre-aligned and then placed on a support table via a plug-in system. A stepper motor allows the adjustment of the whole assembly by 10 mm in order to move the jaws on the plane of collimation and present a fresher surface in the beam impact area in case the initial impact area is damaged. This represents an optional 5th degree of freedom for the collimator's motion.

2.1.3 Local collimator instrumentation

The collimators are equipped with sophisticated instrumentation which will provide extensive diagnostics. The main diagnostics informations are summarized in [17]:

- position of each motor and jaw support point;

- independent measurement of collimator gap at both extremities of collimator tank (average gap and angle between the two jaws);

- independent measurement of one jaw position at both extremities of collimator tank;

RU	Right Upstream
LU	Left Upstream
GU	Gap Upstream
RD	Right Downstream
LD	Left Downstream
GD	Gap Downstream

Table 2.2: Jaws and gaps naming convention

- temperature of each graphite jaw at both extremities: start and end;

- temperature of cooling water at inlet and outlet;

- signals from various switches (in, out, anti-collision, . . .);

- one microphonic sensor per jaw for detection of beam-induced shock waves;

- flow of cooling water per collimator.

The collimators' jaws and gaps naming convention, based on the beam direction, is reported in Tab. 2.2.

The extensive diagnostics allows fail-safe setting of collimator gaps, important checks on self-consistency and detection of abnormal beam load conditions.

Chapter 3

Position Measurement Systems for Collimators

3.1 Collimators Positioning Technology for Particle Accelerators

Collimators' positioning systems of large particle accelerators share the same mature and highly reliable technology all over the world . For the jaws positioning actuation the stepper motor is the preferred solution [18], [2], [19], [20] owing to its (in principle) fully open-loop working. By design the angle is indeed determined, by design, by the stepping mode and the amount of steps produced by its drive. Moreover stepping motors can be easily made radiation-hard [19].

For the jaws position measurements the reference sensor is the LVDT. Apart *LHC*, LVDTs are at the heart of collimators' position measurement for many other particle accelerators, such as *Tevatron* [2], [10], [21] and at *PEP-II* [11].

Scientific and technical literature concerning collimators for particle accelerators is almost completely focused on physics [4], [5], [6], [7] and material

science/engineering [8], [9] especially concerning the *new* crystal collimation. Engineering issues related to sensors and actuators that allow collimators' operation is often neglected. Even mature and well established technologies, when pushed to the edge like in the case of *LHC*, can result in major challenges.
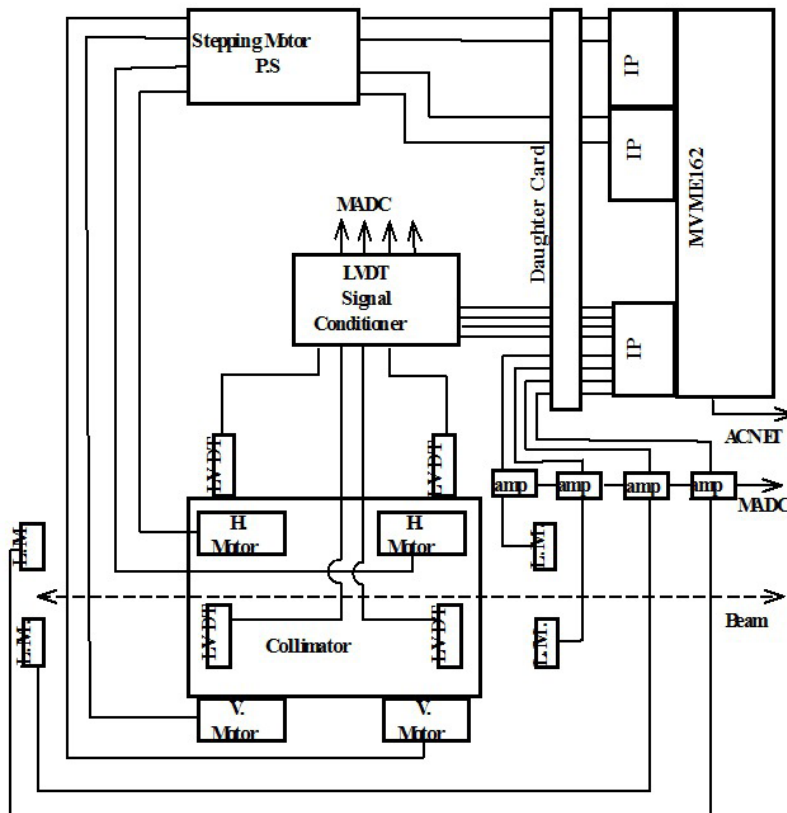
Figure 3.1: Block diagram of Tevatron collimators control system [2]. Courtesy of Fermilab.

3.2 Position Sensors

At the heart of the collimators' positioning system there is the Linear Variable Differential Transformer (LVDT). It is one of the most widespread po-

sition sensor in harsh environments, such as industrial plants, nuclear plants and particle accelerators, thanks to contact-less sensing, good linearity, virtually infinite resolution, low temperature influence, robustness. Popular applications include, therefore, industrial machinery, such as metal forming machines and in-process dimensional verification, as well as automotive and commercial products [22]. Its most important feature in nuclear science and technology is the possibility to easily implement radiation hardness. it has, indeed, been widely used in nuclear plants and research facilities since early seventies [14], [23], [24], [25]. A detailed description of LVDT main features and applications, mainly in non nuclear industrial fields, can be found in [22]; for the scope of this thesis only a brief summary will be given. The LVDT is basically a transformer with one excitation, or primary, coil and two signal, or secondary, coils. The magnetic circuit always ends in air while the shape is usually cylindrical, even though there are exceptions [26]. The movable core of the transformer is concentric to the coils and is bound to the moving element whose position is to be measured. The core moves inside the bore with no contact with the shell of the LVDT neither electrically nor mechanically as schematically shown in Fig. 3.2. There are three electrical circuits: one primary coil and two secondary coils. The actual geometry of the coils can be different from the scheme depicted in Fig. 3.2, i.e. the primary coil can span over the entire length of the sensor.

Basically the two secondary coils are wound along the axis of the cylinder on opposite sides with respect to the primary coil with the same density of turns per length unit; when the core moves toward a coil the amplitude of the flux produced by the primary winding linked to that coil increases and so does the amplitude of the voltage across it. Conversely the one across the

other coil decreases accordingly. When the core extends exactly for one half within each coil the amplitudes of the secondary voltages are ideally equal. In Fig. 3.3 it is graphically summarized the LVDT working principle for the most basic 4-wire, design, where the secondary coils are in series bucking configuration.

The series bucking configuration described in Fig. 3.3 has the main the advantage of simplicity having only one secondary voltage; more accurate,
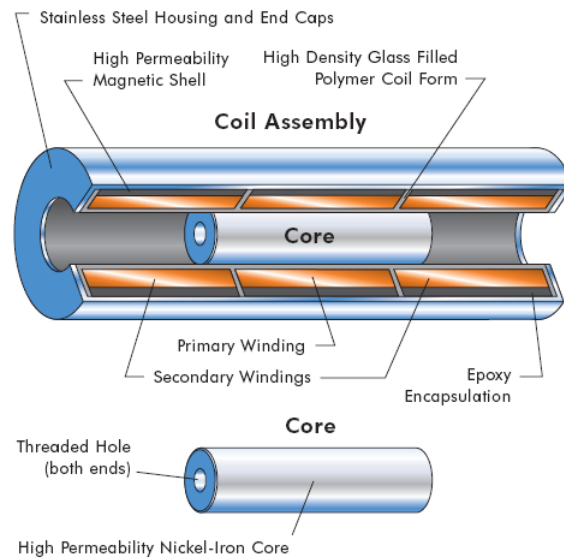
Figure 3.2: LVDT basic geometry. Image: Courtesy of Macrosensors
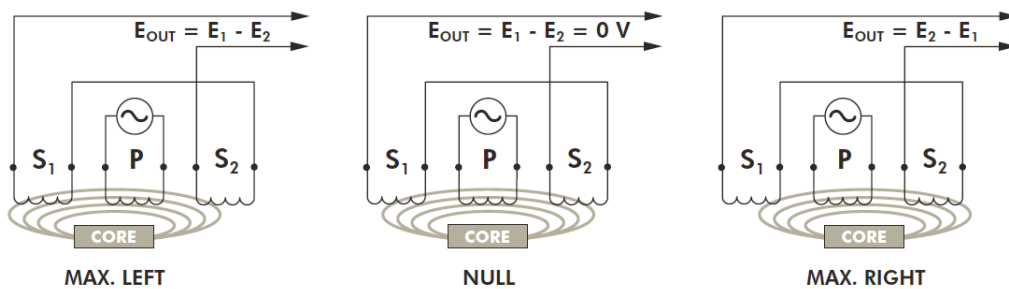
Figure 3.3: 4-wire LVDT Working Principle. Image: Courtesy of Macrosensors.

whether more complex, configurations commonly used are the 5-wire and the 6-wire configurations. The 5-wire configuration gives access to the common of the two secondary coils whereas the 6-wire one presents two sets of fully isolated secondary terminals. Clearly the resolution and the accuracy of such a sensor are strongly determined by the conditioning electronics and the correction algorithm used [27], [28], whereas the influence of temperature and excitation amplitude variations can be drastically reduced by means of *ratiometric* reading [14] which works for the 6-wire configuration.

3.3 LVDT Conditioning

The traditional technique of LVDT signal processing consists in a synchronous demodulation of the differential secondary voltage with respect to the primary [29]. The effect of noise components whose frequencies are far from the frequency of the excitation sine-wave supplying the primary coil is reduced. Fluctuations of the primary signal amplitude are also eliminated at the first order. Nevertheless, most LVDTs present a phase difference ϕ between the signal applied to the primary and the signal resulting from the difference between the two secondaries. The angle depends on the operating point.

The synchronous demodulation is obtained by means of multiplication with a signal synchronous with the carrier and subsequent low pass filtering. As a result the LVDT position measurement depends on the phase difference ϕ which in turn depends on the cable length used to drive the sensor. A manual tuning is therefore needed at installation in order to compensate the phase error related to different cable lengths. This is the case for instance of the integrated circuit *AD698* from Analog Device [30].

Some digital techniques have been developed to estimate the phase error

by means of a *PLL* in order to correct it automatically [31]. This approach provides a greater accuracy, but it maintains the same original dependence on $\cos(\phi)$.

Near the null point, say for measurement below 5 % of the Full Scale (FS), the variability of ϕ increases and moreover, since the differential secondary signal is very low, it will be heavily affected by noise, at the point that phase recovery may become impossible. In addition in large particle accelerators application, such as *LHC*, the long cables between sensors and electronics transform the impedance seen by the conditioner from inductive to capacitive. In this situation phase recovery would require a very sophisticated algorithm.

The *AD598* integrated circuit performs an asynchronous demodulation to correct the effect of phase uncertainty in the null position [32]. It works with a 5-wire configuration and is based on *ratiometric* conditioning. This ensures a compensation of the amplitude drift on the excitation signal. The noise immunity of this solution is not better than that obtained with a synchronous demodulation especially if it is used in a 4-wire configuration [33]. Ratiometric conditioning however implies that the sum of the two secondaries has to be independent of the position of the LVDT core in order to not affect the measurement linearity.

Spectral techniques, for instance the one based on Goertzel algorithm [34], are characterized by a higher noise immunity but suffer of the spectral leakage problem. A window on the sampled signal has to be applied in the frequency domain to reduce this error.

3.4 LHC Collimators' Position Measurement System

A position measurement system (Position Readout and Survey) *PRS* has been defined in order to ensure the level of machine safety required by the *LHC*. The required precision is one tenth of the beam core diameter, which at nominal energy is about 200 μm. Therefore 20 μm is assumed as the design target uncertainty. The *PRS* verifies in real-time the actual position of the jaw. Depending on the type and energy of the circulating beams, the *PRS* is enabled to trigger a beam abort in case of discrepancy between the desired and the measured position of the jaw. Each jaw can be moved on both ends by stepping motors that can position it at a well defined angle and distance with respect to the nominal beam trajectory. The LVDT sensor has been chosen to measure the jaw position; up to 7 specifically-designed LVDTs are installed on each collimator, while each *PRS* controls up to three collimators (primary, secondary and tertiary collimators). Therefore, it should acquire position signals from up to 21 LVDTs at the same time and monitor in real-time, at a rate up to 100 *readings/s*, more than 600 LVDTs (because more than 100 collimators are installed in the machine) [35]. Such a high rate is necessary to assure that the relative position of two jaws in different collimators remains unchanged during the execution of a movement function within a tolerance of 20 μm. A preliminary metrological characterization of the *PRS* was discussed in [13]; its most relevant contribution is the thermal characterization of the LVDTs together with the whole chain of conditioning hardware. Furthermore a very preliminary characterization of DC magnetic field *interference* on LVDT nominal operation was also presented.

Part II: Proposal

Chapter 4

Instrument Architecture

4.1 Requirements

The requirements of the collimator jaws position measurement are quite demanding. The proposed Position Readout and Survey instrument is, indeed, responsible for the crucial task of checking the coherence of actual jaws' positions with those demanded by the Collimator Supervisor System *CSS* [35]. The *PRS* is required to be independent from the *MDC* (Motor Drive Control), the low-level control module directly controlling the movement of the stepping motors, in order to increase the overall reliability of the control system. Therefore, the *PRS* has to run on a different machine than the *MDC*. According to the different configurations of the collimation system throughout *LHC*, a single *PRS* must be able to serve up to three collimators. The target positioning uncertainty demanded by the accelerator physicists is one tenth of the beam transverse dimension: 200 μm at *LHC* top energy. The *PRS* is therefore required to measure the position of the jaws by means of up to seven LVDTs installed on each collimator, at a rate of 100 $readings/s$ with an uncertainty not greater than $pm20$ μm. The high *sampling* rate is necessary to ensure that the relative position of two jaws in different collimators

remains unchanged during the execution of a motion function characterized by a maximum linear speed of 2 mm/s. Furthermore, since the collimators are among the most *activated* equipment of *LHC* no electronics could reliably operate in the immediate closeness of collimators. The electronics of the instruments has been, therefore, put in special alcoves up to 800 m far from them. Such constraint, in an environment which is highly populated by many different devices, makes impossible to exert a reasonable control on the *influence quantities* that might jeopardize the accuracy of the collimators' position measurement. Such environment is expected to be characterized, in principle, by low *SNR* for which opportune design solutions must be adopted. Moreover a cost-performance trade-off has been accepted in the choice of the cable connecting LVDTs to the measurement electronics: multi-wire cables have been adopted, at the cost of an increased risk of cross-talk between the different LVDTs signals. The instrument requirements can be summarized as follows:

- target measurement uncertainty of ±20 μm,

- 100 $readings/s$,

- high immunity to wide-spectrum noise,

- high immunity to cross-talk,

- compliance with cable lengths up to 800 m,

- high reliability,

- up to 3 collimators per single instrument,

- up to 7 LVDTs per single collimator.

4.2 Concept Design

In Fig. 4.1 the conceptual design of the instrument is depicted. At the heart of the instrument there is the position sensor LVDT. Among different types of LVDTs the most accurate one is the 6-wire *ratiometric*; its primary, sinusoidal, voltage is generated by the electronics equipping the instrument and delivered to the primary coil of the sensor by means of a cable with a length up to 800 m. The secondary coils are connected to DAQ channels by means of long cables as well.

The ideally sinusoidal secondary voltage signals are sampled, synchronously, at high sampling rate; the acquired samples constitute the input of the core algorithm of the instrument (expressly highlighted in the figure), that estimates the amplitude of the signal, or more precisely, the amplitude of the signal harmonics at the known frequency of the generator. The estimated amplitudes are then used to evaluate the *ratiometric* that is linearly proportional to the *measurand* position with excellent approximation (on the right of Fig. 4.1). By means of calibration tables the measurement result is eventually obtained. On the left of Fig. 4.1 a peculiar, and crucial problem, non characterized in literature before, arising when LVDTs experience DC or slowly varying external magnetic field, is depicetd. This problem has to be taken into account in the design; magnetic shielding together with a DC polarization of the LVDT primary circuit are the design solutions proposed (highlighted in the figure).

The rest of this Chapter details the *Hardware/Software Layer* depicted in Fig. 4.1, whereas Chapter 5 is devoted to the analysis and design of the key algorithm for the amplitude estimation. Chapters 6 and 7, instead, deal

with the critical issue related to the *Physical Layer*. In particular, Chapter 6 introduces the problem of how critically magnetic fields interfere with the measurement process and, then, develops a strategy for its analysis. Such an analysis constitutes the basis of the conception of design guidelines, presented in Chapter 7, aimed at solving such a problem in its general terms.
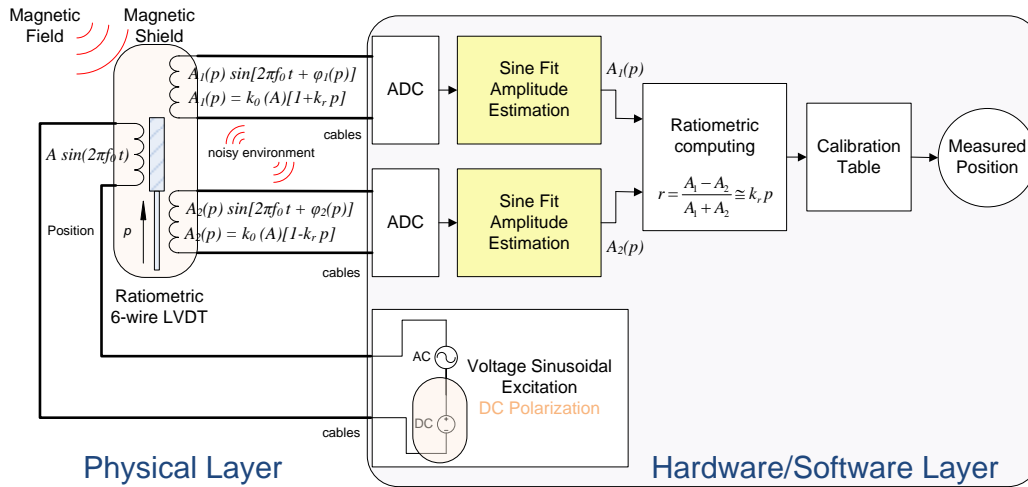
Figure 4.1: Concept Design of the Instrument.

4.3   Hardware Architecture

In Fig. 4.2 the description of the hardware architecture of a *PRS* configured for 3 collimators is depicted. A *National Instruments PXI* chassis is equipped with an RT controller *NI-PXI 8106* based on an Intel Core 2 Duo Processor at 2.16 *GHz*. For each collimator controlled by the specific chassis, two *DAQ* cards *NI PXI 6143* with 8 simultaneous differential analog inputs sampled at 16 *bit* and 250 *kS/s* are used to acquire the 14 signals coming from the secondary coils of the 7 LVDTs installed on each collimator; a picture of the *PRS* equipped for 3 collimators in shown in Fig. 4.3. Data acquired are transferred to the CPU via *DMA* using circular buffers as shown in Fig. 4.2.

In this way, the acquisition of the signals coming from the LVDT secondaries is decoupled from their processing, releasing CPU resources. Furthermore, an *FPGA* card *NI PXI 7831R* having 8 analog outputs is used to generate the primary signals for the *21* LVDTs. Seven outputs are used to generate sine waves of different frequencies, orthogonal with respect to the frequency response of the sine-fit algorithm used (an important property of the algorithm that will be detailed in Chapter 5). All the signals sent to or coming from the LVDTs are interfaced through custom PCB in *Europe* format to ensure at the same time reliability and modularity.

Every signal coming from the analog outputs of the *7831* card is split on three different lines in the *Europe* cards, and then amplified individually through buffer amplifiers to properly drive each sensor over the long cables. In case of fault on a power stage of one of the collimators, the two others will not be affected. The same *FPGA* card is also responsible for the synchronization of all the *DAQ* cards on the precise 10 *MHz* clock distributed to all the *PXI* chassis as well as for the synchronization of the motion survey process for each collimator on the trigger signal sent by the *CSS*. A 250 *kHz* clock for all the *DAQ* cards is generated by the *FPGA* from the *CLK*/10 on the *RTSI* bus used as reference clock. The start of the readout and survey loops for each collimator is triggered respectively by the signals $TRG0$, $TRG1$ and $TRG2$ on the *RTSI* bus generated by the *FPGA* at reception of a trigger from the *CSS*.

4.4 Software Architecture

In addition to the above features, the following ones are also implemented in the *PRS*:
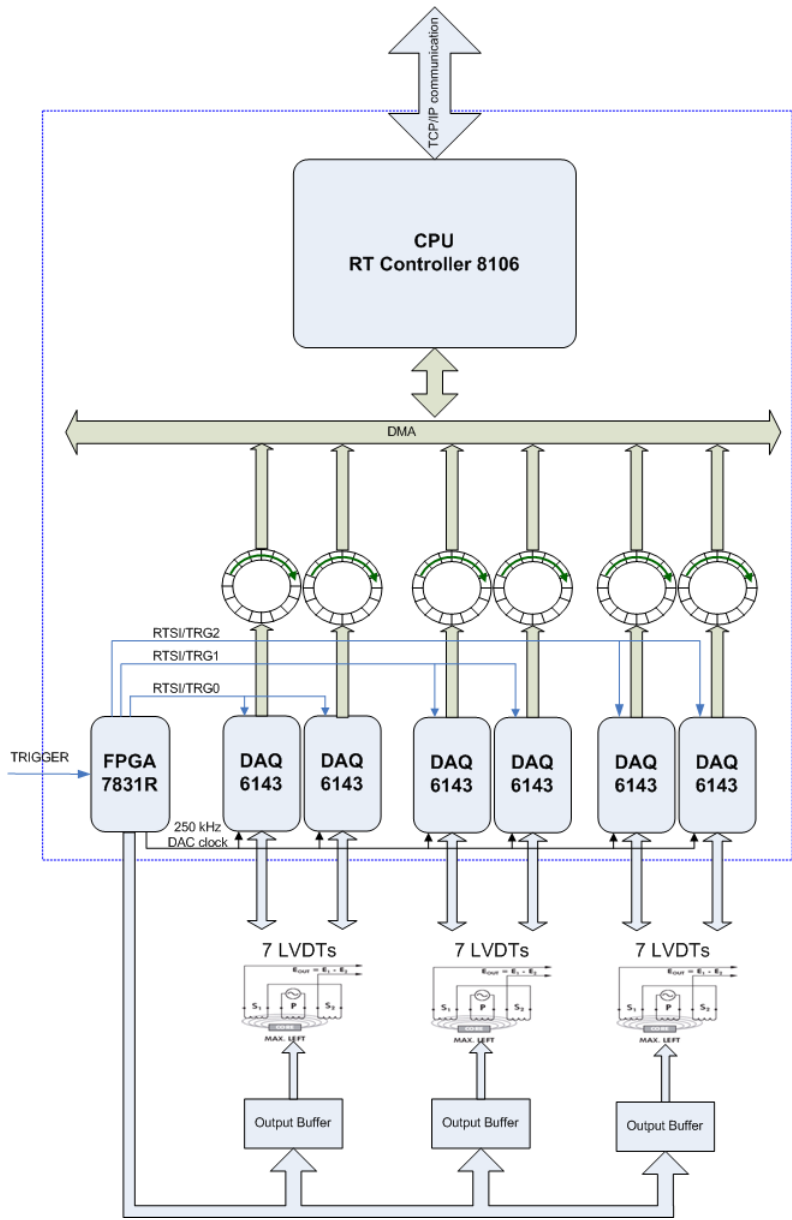
Figure 4.2: Hardware architecture of a PRS.

- pre-processing the commands received from the *CSS*: coherence check, protocol check;

- preparation of the upper and lower threshold profiles for the collimator axes and the two gaps;
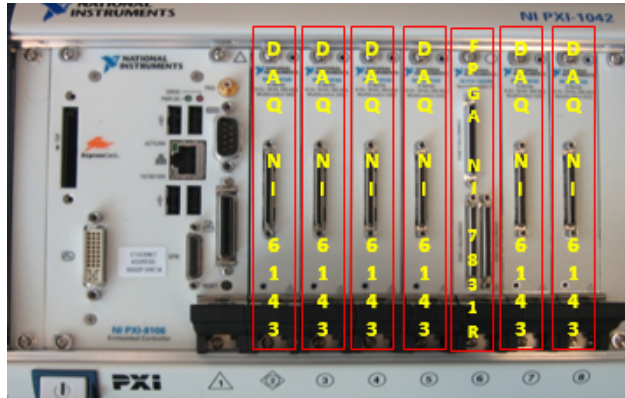
Figure 4.3: Picture of the PRS configured for 3 collimators.

- generation of the excitation sinusoidal signals supplying up to 21 LVDTs;

- synchronization of the motion profiles survey process on the trigger received by the *CSS*.

Most of the functions are executed by means of real-time tasks running on the *PXI* controller *NI-PXI 8106*, except for the generation of the excitation sinusoidal signals supplying the LVDTs and the synchronization task, which are entirely implemented in the *FPGA* of the *NI-PXI 7831* card. The architecture of the real-time tasks executed on the *PRS* for the readout and survey of three collimators is shown in Fig. 4.4, where yellow-colored tasks are executed on the CPU and grey-colored tasks on the *FPGA*. The CPU *command listener* waits for commands or settings sent by the *CSS* on the related *DIM* services. The event recognition loop has 1 *ms* cycle time and the highest priority to ensure negligible reaction time. At reception of the request of motion profile survey, it prepares upper and lower limit arrays for each axis according to the boundary function sent by the *CSS*. The limits represent thresholds for triggering a beam abort. A linear interpolation is applied to update the threshold value each 10 *ms*. An acknowledge is then

sent to the *CSS* to inform it that the *PRS* is ready for the profile survey and is waiting for the hardware trigger. The synchronization of the reading and survey process on the *CPU* is performed by the *FPGA* card (task *LVDTs excitation reading and synchronization*). As soon as the trigger is received from the *CSS* a 100 *Hz* clock is generated on the *RTSI* trigger line related to the collimator to survey. This accurate timing signal synchronizes the *CPU* task that performs the LVDTs reading and the comparison with the associated thresholds. This approach guarantees that the time jitter on the LVDTs reading will not exceed 100 μs, the error on position reading will therefore remain well within specifications. The *position readout and survey* task on the *CPU* performs the processing of the signals of the 7 LVDTs installed on the collimator using ratiometric conditioning.
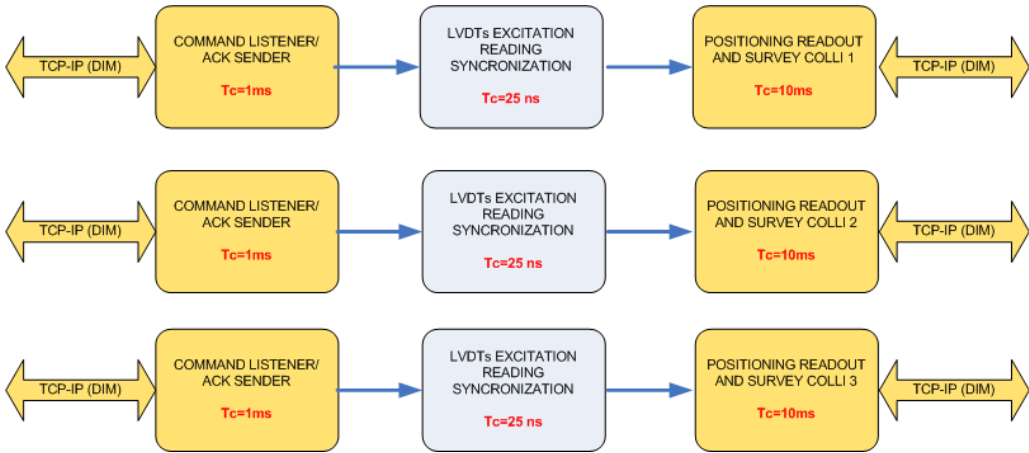
Figure 4.4: Software architecture.

Chapter 5

Estimation of the secondary voltage amplitudes

The *PRS* instrument takes full advantage of *ratiometric* 6-wire LVDTs. In Fig. 5.1 the working principle of the 6-wire LVDT is illustrated: as the high permeability moving core of the transformer moves toward one of the two secondary windings the magnetic coupling with it increases while it decreases with respect to the other one. The amplitudes of the secondary voltages change accordingly. Thus the two secondary voltages are amplitude modulated by the core position; with very good approximation the amplitudes change linearly with the position of the core. Non linearity is typically smaller than 0.1 %.

Thus secondary circuits are isolated and both secondary voltages are available, the *ratiometric reading* takes advantage of that by forming the *ratiometric* as in equation (5.1).

$$r\left(p\right) = \frac{A_1\left(p\right) - A_2\left(p\right)}{A_1\left(p\right) + A_2\left(p\right)} \tag{5.1}$$

Variation of the primary voltage amplitude has a tremendously reduced effect on the *ratiometric* since both secondary voltages' amplitudes are ap-

proximatively linearly proportional to the amplitude of the primary voltage which is canceled out by the division. Immunity to temperature variation is greatly enhanced as well [14]. Furthermore ratiometric LVDTs are expressly designed to keep the sum of the secondary voltages' amplitudes constant with respect to the core position p.
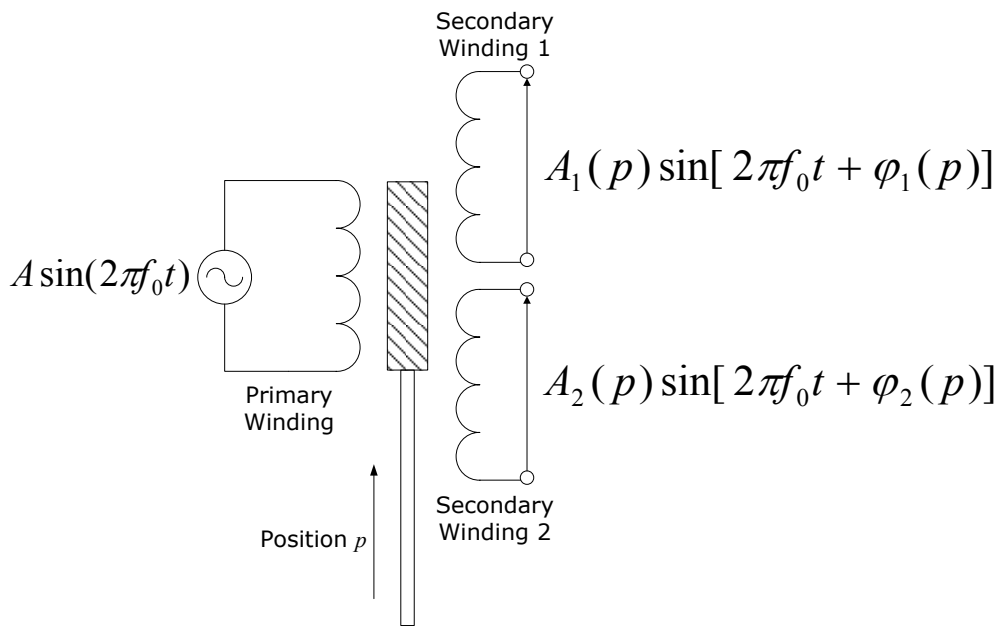
Figure 5.1: Working principle of the 6-wire LVDT.

The estimation of the amplitude of the secondary voltages is therefore the key element of the position measurement instrument.

5.1 The three-parameter sine fit

The three-parameter sine fit is a linear least-squares estimation algorithm suggested by *IEEE standard 1241-2000* [36] in ADC characterization to estimate sine wave parameters from recorded data when the frequency of the

sine wave signal is known. An interesting discussion on its main character-istics can be found in [37]. Its metrological performance in presence of additive noise of different statistical distributions has been extensively studied in the asymptotic case of large number of acquired samples [38]: Cramér-Rao bounds have been determined for the three parameters [39] and the bias of sine-wave's amplitude estimation has been proven for coherent sampling [40]. Conversely the properties of the algorithm have been investigated even for a number of samples as small as five [41] with application to LVDT signal conditioning. Anyway a systematic study of the metrological properties of the algorithm has never been presented for an arbitrary choice of the two design parameters: number of samples and sampling frequency. In this Chapter an analytical metrological characterization of the three-parameter sine fit algorithm in terms of its design parameters is carried out. In 5.3, neglecting the jitter, a thorough characterization of the algorithm is developed in terms of the eigenvalues and the eigenvectors of a suitable matrix in the very general case of zero mean additive noise. Subsequently optimal and sub-optimal sets of design parameters are found. Paragraph 5.4 is devoted to the detailed characterization of the amplitude estimation with respect to zero mean additive noise and its *frequency behaviour*. An approximated second order statistical characterization is given under the hypothesis of additive white noise (AWN) whereas an approximated, but complete, statistical characterization can be found under additive white Gaussian noise (AWGN) hypothesis. Eventually, as a by-product, the probability density function of the amplitude estimator is given for the optimal parameters' set as recently presented in [42]. Eventually the exact frequency response expression is found in the optimal case. The frequency response of the amplitude estimator turns out to have

important practical application for the design of the core algorithm of the instrument. As stated in [36] the best estimate, in the least squares sense, of the amplitude A, the phase ψ and the offset O of a sine wave signal of known frequency f_0 from N of its samples $y_0, y_1, \ldots, y_{N-1}$ acquired at the time instants $t_0, t_1, \ldots, t_{N-1}$ is obtained by minimizing the following error:

$$e = \sqrt{\sum_{i=0}^{N-1} \left[y_i - A_c \cos(2\pi f_0 t_i) - A_s \sin(2\pi f_0 t_i) - O_0 \right]^2} \qquad (5.2)$$

The parameters A, ψ and O are given by:

$$\begin{cases} A = \sqrt{A_c^2 + A_s^2} \\ \psi = \text{Atan2}(A_s, A_c) \\ O = O_0 \end{cases} \qquad (5.3)$$

where the function $\text{Atan2}(y, x)$ evaluates the arctangent of the ratio y/x but uses the sign of each argument to determine the quadrant of the resulting angle; this allows the correct determination of an angle in the range $[0, 2\pi[$. Introducing the following matrix and vectors:

$$\mathbf{D} = \begin{bmatrix} \cos(2\pi f_0 t_0) & \sin(2\pi f_0 t_0) & 1 \\ \cos(2\pi f_0 t_1) & \sin(2\pi f_0 t_1) & 1 \\ \vdots & \vdots & \vdots \\ \cos(2\pi f_0 t_{N-1}) & \sin(2\pi f_0 t_{N-1}) & 1 \end{bmatrix} \qquad (5.4)$$

$$\mathbf{y} = \begin{bmatrix} y_0 \\ y_1 \\ \vdots \\ y_{N-1} \end{bmatrix}, \quad \mathbf{x} = \begin{bmatrix} A_c \\ A_s \\ O_0 \end{bmatrix} \qquad (5.5)$$

the square of the error in (5.2) can be expressed in matrix notation as in the following equation.

$$e^2(\mathbf{x}) = (\mathbf{y} - \mathbf{D}\mathbf{x})^T (\mathbf{y} - \mathbf{D}\mathbf{x}) \qquad (5.6)$$

By minimizing (5.6) with respect to $\mathbf{x}$ the best estimation $\widehat{\mathbf{x}}$ of the sine wave parameters vector $\mathbf{x}$ is obtained.

The unique solution existing whenever the matrix $\mathbf{D}$ is full rank is:

$$\widehat{\mathbf{x}} = \mathbf{D}^{\dagger}\mathbf{y} \tag{5.7}$$

The matrix $\mathbf{D}^{\dagger}$ expressed by the following equation:

$$\mathbf{D}^{\dagger} = \left(\mathbf{D}^{T}\mathbf{D}\right)^{-1}\mathbf{D}^{T} \tag{5.8}$$

is the well known *Moore-Penrose* matrix pseudo-inverse [43] [44], which, in turn, is the left pseudo-inverse of matrix $\mathbf{D}$, when the matrix $\mathbf{D}$ is full rank. The details of the calculations are given in appendix A. Actually the pseudo-inverse always exists, even though the solution that minimizes (5.2) or equivalently (5.6) it is not unique in the case $\mathbf{D}$ is not full rank because of the rank-nullity theorem.

The conditions for $\mathbf{D}$ being full rank will be discussed in the following paragraphs by means of the analysis of the eigenvalues of the *core matrix* $\mathbf{D}^{T}\mathbf{D}$. Moreover, as it will be shown, the complete characterization of the three-parameter sine fit estimation error can be thoroughly developed by means of the properties of this matrix.

5.2 Closed form of the core matrix

The matrix $\mathbf{D}$, fixed the frequency f_0, is formed only by the knowledge of the time instants $t_0, t_1, \ldots, t_{N-1}$.

Neglecting the sampling jitter uncertainty the samples of the input signal are supposed to be uniformly spaced by $1/F_S$ seconds, F_S being the sampling

rate expressed in samples per second $[S/s]$. The generic sample time instant can be written as:

$$t_k = \frac{k}{F_S} \tag{5.9}$$

The frequency f_0 can be expressed as a function of the number of samples and the sampling rate considering that in the time span covered by the N samples there is an integer number M of periods of the input signal plus a fraction α:

$$f_0 = (M + \alpha) \frac{F_S}{N} \tag{5.10}$$

Introducing the following angle:

$$\theta = \pi (M + \alpha) \tag{5.11}$$

it is possible to express the instant phase as in the following equation.

$$2\pi f_0 t_k = 2\theta \frac{F_S}{N} t_k = 2\theta \frac{k}{N} \tag{5.12}$$

Matrix $\mathbf{D}$, as well as its transpose $\mathbf{D}^T$, can be rewritten in terms of its columns:

$$\mathbf{D} = [\mathbf{c}\ \mathbf{s}\ \mathbf{1}\ ], \quad \mathbf{D}^T = \begin{bmatrix} \mathbf{c}^T \\ \mathbf{s}^T \\ \mathbf{1}^T \end{bmatrix} \tag{5.13}$$

The columns are expressed as follows:

$$\mathbf{c} = \begin{bmatrix} \cos(2\theta \frac{0}{N}) \\ \cos(2\theta \frac{1}{N}) \\ \vdots \\ \cos(2\theta \frac{N-1}{N}) \end{bmatrix}, \quad \mathbf{s} = \begin{bmatrix} \sin(2\theta \frac{0}{N}) \\ \sin(2\theta \frac{1}{N}) \\ \vdots \\ \sin(2\theta \frac{N-1}{N}) \end{bmatrix}, \quad \mathbf{1} = \begin{bmatrix} 1 \\ 1 \\ \vdots \\ 1 \end{bmatrix} \tag{5.14}$$

By considering the dot product as the usual row column product the *core matrix* can be now expressed as follows:

$$\mathbf{D}^T\mathbf{D} = \begin{bmatrix} \mathbf{c}^T\mathbf{c} & \mathbf{c}^T\mathbf{s} & \mathbf{c}^T\mathbf{1} \\ \mathbf{s}^T\mathbf{c} & \mathbf{s}^T\mathbf{s} & \mathbf{s}^T\mathbf{1} \\ \mathbf{1}^T\mathbf{c} & \mathbf{1}^T\mathbf{s} & \mathbf{1}^T\mathbf{1} \end{bmatrix} \tag{5.15}$$

The elements of the $\mathbf{D}^T\mathbf{D}$ are the dot products of the columns by means of which the general sinusoidal signal can be expressed by N of its samples acquired at F_S samples per second.

More insight into the structure of the *core matrix* can be gained by writing symbolically its elements in terms of the design parameters of the fit algorithm namely the number of samples N and, via (5.11), the sampling frequency F_S.

The following variables are needed:

$$S = \frac{\sin\theta}{\sin(\theta/N)} \quad , \quad C = \frac{\cos\theta}{\cos(\theta/N)} \quad , \quad \gamma = \frac{N-1}{N}\theta \tag{5.16}$$

the details of the calculation are given in appendix B.

Once the symbolic expression of the *core matrix* is known it is possible to symbolically find its spectral decomposition; this will allow a complete knowledge of its properties and the ones of the overall pseudo-inverse matrix as it will be shown in the following. This matrix has been analyzed in several papers [40] and [39] among many others; its symbolic closed form has never been presented, thus conclusions have been drawn only in the asymptotic case of $N \to \infty$.

The spectral decomposition of the square matrix $\mathbf{D}^T\mathbf{D}$ is:

$$\mathbf{D}^T\mathbf{D} = \mathbf{V}\mathbf{\Lambda}\mathbf{V}^T \tag{5.17}$$

where the diagonal matrix $\mathbf{\Lambda}$ contains, on its diagonal, the eigenvalues λ_1, λ_2 and λ_3 and $\mathbf{V} = [\mathbf{v}_1\ \mathbf{v}_2\ \mathbf{v}_3]$ is the orthogonal matrix whose columns are the eigenvectors of $\mathbf{D}^T\mathbf{D}$ associated with the respective eigenvalues.

The eigenvalues are expressed by the following equations:

$$\begin{cases} \lambda_1 = \frac{N}{2} - \frac{SC}{2} \\ \lambda_2 = \frac{N}{2} + \frac{(N+SC)-\sqrt{(N-SC)^2+16S^2}}{4} = \frac{N}{2} + \lambda_- \\ \lambda_3 = \frac{N}{2} + \frac{(N+SC)+\sqrt{(N-SC)^2+16S^2}}{4} = \frac{N}{2} + \lambda_+ \end{cases} \qquad (5.18)$$

The eigenvectors are:

$$\mathbf{v}_1 = \frac{\begin{bmatrix} -\tan\gamma \\ 1 \\ 0 \end{bmatrix}}{\sqrt{1+tan^2\gamma}}, \quad \mathbf{v}_2 = \frac{\begin{bmatrix} \frac{\lambda_- -N/2}{S}\cos\gamma \\ \frac{\lambda_- -N/2}{S}\sin\gamma \\ 1 \end{bmatrix}}{\sqrt{1+\frac{(\lambda_- -N/2)^2}{S^2}}}, \quad \mathbf{v}_3 = \frac{\begin{bmatrix} \frac{\lambda_+ -N/2}{S}\cos\gamma \\ \frac{\lambda_+ -N/2}{S}\sin\gamma \\ 1 \end{bmatrix}}{\sqrt{1+\frac{(\lambda_+ -N/2)^2}{S^2}}}$$

$$(5.19)$$

where $\lambda_\pm$ is expressed by (5.20).

$$\lambda_\pm = \frac{(N+SC) \pm \sqrt{(N-SC)^2 + 16S^2}}{4} \qquad (5.20)$$

The details of the calculations are given in appendix B as well.

Sufficient conditions for the singularity of the core matrix are expressed by the following equation (see appendix C for the calculations):

$$f_0 = q\frac{F_S}{2} \quad \text{for} \quad q = 1, 2, \dots \qquad (5.21)$$

Equation (5.21) states that the core matrix is singular and hence the sine fit cannot work if the frequency of the signal to be fitted is an integer multiple factor of half of the sampling frequency.

5.3 Characterization of the algorithm with noisy input

Here only zero-mean additive noise has been considered; the generic input is therefore expressed by the following equation:

$$y(t) = u(t) + w(t) \tag{5.22}$$

where $w(t)$ is a zero mean random process. The vectors representing the acquired samples of the ideal input $u(t)$ and superimposed noise $w(t)$ are expressed as follows:

$$\mathbf{u} = \begin{bmatrix} u(t_0) \\ u(t_1) \\ \vdots \\ u(t_{N-1}) \end{bmatrix} \quad , \quad \mathbf{w} = \begin{bmatrix} w(t_0) \\ w(t_1) \\ \vdots \\ w(t_{N-1}) \end{bmatrix} \tag{5.23}$$

The ideal input samples can be rewritten in matrix notation as:

$$\mathbf{u} = \widetilde{A}_c \mathbf{c} + \widetilde{A}_s \mathbf{s} + \widetilde{O} \mathbf{1} = \mathbf{D} \begin{bmatrix} \widetilde{A}_c \\ \widetilde{A}_s \\ \widetilde{O} \end{bmatrix} = \mathbf{D} \widetilde{\mathbf{x}} \tag{5.24}$$

where $\widetilde{\mathbf{x}}$ is the vector containing the *true* parameters of the purely sinusoidal signal with an offset defined by (5.25).

$$\widetilde{\mathbf{x}} = \begin{bmatrix} \widetilde{A}_c \\ \widetilde{A}_s \\ \widetilde{O} \end{bmatrix} \tag{5.25}$$

By applying (5.7) to the noisy input (5.26) is obtained.

$$\mathbf{D}^\dagger \left(\mathbf{u} + \mathbf{w} \right) = \mathbf{D}^\dagger \mathbf{D} \widetilde{\mathbf{x}} + \mathbf{D}^\dagger \mathbf{w} = \widetilde{\mathbf{x}} + \mathbf{D}^\dagger \mathbf{w} \tag{5.26}$$

Equation (5.26) clearly shows that with zero mean superimposed noise the expected values of the algorithm output vector components are exactly the

true parameters of the ideal sinusoidal input, thus the estimation is unbiased for the parameters A_c, A_s and O. It shows as well that the estimation error for each of them can be fully characterized by means of the knowledge of the pseudo-inverse matrix $\mathbf{D}^\dagger$ and the statistical description of the superimposed noise.

By defining $\mathbf{e} = \mathbf{D}^\dagger \mathbf{w}$ the estimation error induced by the additive noise samples $\mathbf{w}$, the estimate of the parameters is expressed by:

$$\widehat{\mathbf{x}} = \widetilde{\mathbf{x}} + \mathbf{e} \tag{5.27}$$

$\widehat{\mathbf{x}}$ will denote the estimator hence after; its covariance matrix can be expressed as:

$$
\begin{aligned}
\mathbf{C} \;\overset{\text{def}}{=}\; & E\left[(\widehat{\mathbf{x}} - \widetilde{\mathbf{x}})(\widehat{\mathbf{x}} - \widetilde{\mathbf{x}})^T \right] = E\left[\mathbf{e}\mathbf{e}^T \right] \\
= \; & E\left[\mathbf{D}^\dagger \mathbf{w}\mathbf{w}^T \mathbf{D}^{\dagger^T} \right] = \mathbf{D}^\dagger E\left[\mathbf{w}\mathbf{w}^T \right] \mathbf{D}^{\dagger^T} = \mathbf{D}^\dagger \mathbf{C}_{\mathbf{w}\mathbf{w}} \mathbf{D}^{\dagger^T}
\end{aligned} \tag{5.28}
$$

since the error $\mathbf{e}$ has zero average having assumed the noise $\mathbf{w}$ to be zero average. The euclidean norm of the estimator covariance matrix will be used in order to quantify the estimation error. For the norm the following inequality holds:

$$\|\mathbf{C}\| \le \|\mathbf{D}^\dagger\| \|\mathbf{C}_{\mathbf{w}\mathbf{w}}\| \|\mathbf{D}^{\dagger^T}\| \tag{5.29}$$

The euclidean norm of a matrix is defined as its maximum singular value. The norm of its pseudo-inverse is given by the inverse of its minimum singular value, as shown in the following equation:

$$\left\| \mathbf{D}^\dagger \right\| = \sigma_{max}\left(\mathbf{D}^\dagger \right) = \sigma_{min}^{-1}\left(\mathbf{D} \right) \tag{5.30}$$

One of the definitions of the singular values states that:

$$\sigma_i\left(\mathbf{D}\right) \overset{\text{def}}{=} \sqrt{\lambda_i\left(\mathbf{D}^T\mathbf{D}\right)} \qquad (5.31)$$

According to (5.31) and (5.30) the knowledge of the eigenvalues only of the core matrix allows the evaluation of the norm of the pseudo-inverse matrix. An upper bound on the norm of the estimator covariance matrix can be put, for a given choice of the algorithm parameters, as in the following inequality:

$$
\begin{aligned}
\|\mathbf{C}\| \leq \|\mathbf{D}^\dagger\|\|\mathbf{C_{ww}}\|\|\mathbf{D}^{\dagger T}\| &= \sigma_{min}^{-1}\left(\mathbf{D}\right)\|\mathbf{C_{ww}}\|\sigma_{min}^{-1}\left(\mathbf{D}\right) \\
&= \frac{\|\mathbf{C_{ww}}\|}{\sigma_{min}^2} = \frac{\|\mathbf{C_{ww}}\|}{\lambda_{min}}
\end{aligned}
\qquad (5.32)
$$

Inequality (5.32) is important because it clearly shows that, no matter which kind of zero mean additive noise is present at the input of the algorithm, the norm of the covariance matrix of the error is minimized by maximizing the value of the smallest eigenvalue of matrix $\mathbf{D}^T\mathbf{D}$, thus the algorithm parameters, if possible, can be chosen accordingly.

Under the assumption of $w(t)$ being white, its samples, that form the random vector $\mathbf{w}$, are independent and have the same statistical distribution, thus its correlation matrix is $\mathbf{C_{ww}} = \sigma_{\text{w}}^2\mathbf{I}_N$. According to this property (5.28) can be particularized for white additive noise as follows:

$$
\begin{aligned}
\mathbf{C} = \sigma_{\text{w}}^2\mathbf{D}^\dagger\mathbf{I}_N\mathbf{D}^{\dagger T} &= \sigma_{\text{w}}^2\left(\mathbf{D}^T\mathbf{D}\right)^{-1}\mathbf{D}^T\mathbf{D}\left(\mathbf{D}^T\mathbf{D}\right)^{-1} \\
&= \sigma_{\text{w}}^2\left(\mathbf{D}^T\mathbf{D}\right)^{-1}
\end{aligned}
\qquad (5.33)
$$

By using now the symbolic expression of the eigenvectors too the whole covariance matrix of the estimator can be evaluated and yields :

$$\mathbf{C} = \mathbf{V} \begin{bmatrix} \frac{\sigma_{\mathrm{w}}^2}{\sigma_1^2} & 0 & 0 \\ 0 & \frac{\sigma_{\mathrm{w}}^2}{\sigma_2^2} & 0 \\ 0 & 0 & \frac{\sigma_{\mathrm{w}}^2}{\sigma_3^2} \end{bmatrix} \mathbf{V}^T \qquad (5.34)$$

In the most general case matrix $\mathbf{C}$ is not diagonal even considering white noise at the input of the algorithm thus the different components of the estimation error are not uncorrelated. Nevertheless adding the further hypothesis of gaussianity it can be concluded that the estimator $\widehat{\mathbf{x}}$ is a vector of Gaussian Random Variables (RVs hereafter) with expected value $\widetilde{\mathbf{x}}$ and covariance matrix $\mathbf{C}$ thus its statistical characterization of any order is completely known.

To summarize it's worth remarking that given the knowledge of the input noise variance, by means of eigenvalues and eigenvectors of the core matrix, the estimator covariance matrix can be designed *a priori* in case of AWN (this turns out to being sufficient for the complete statistical description of the estimator in the AWGN case) or, it can be, at least, minimized in norm when such hypotheses do not hold.

5.3.1 Optimal and sub-optimal choices of the design parameters

Whenever the number of periods acquired is an integer number the angle θ is an integer multiple factor of π thus the auxiliary variable S in (5.16) is zero.

In this case the inequality (5.32) states that the norm of the covariance matrix of the error is the minimum possible given the input additive noise and the number of samples acquired.

Obviously as N increases the difference between eigenvalues λ_1 and λ_2

becomes less and less important; the asymptotic value of σ_{min} goes as $\sqrt{N/2}$ thus the difference between coherent and incoherent sampling becomes less and less important.

A sub-optimum exists as well in the point in which the two eigenvalues λ_1 and λ_2 are equal. The non-integer fraction of acquired periods of the input signal α_{sub} can be found by solving the following equation:

$$\frac{\sin^2 2\theta_{sub}}{\sin^2 (2\theta_{sub}/N)} + N \frac{\sin 2\theta_{sub}}{\sin (2\theta_{sub}/N)} = 2 \frac{\sin^2 \theta_{sub}}{\sin^2 (\theta_{sub}/N)} \qquad (5.35)$$

where $\theta_{sub} = \pi (M + \alpha_{sub})$.

The corresponding sub-optimum eigenvalue is:

$$\lambda_{1,2}^{sub} = \frac{N}{2} - \frac{1}{2} \frac{\sin 2\theta_{sub}}{\sin (2\theta_{sub}/N)} \qquad (5.36)$$

The smallest eigenvalue of matrix $\mathbf{D}^T \mathbf{D}$ is therefore maximum and equal to $N/2$ whenever the fraction α is either 0 or 1, *coherent sampling*, or locally maximum whenever $\alpha = \alpha_{sub}$.

The smallest eigenvalue of matrix $\mathbf{D}^T \mathbf{D}$ is therefore maximum and equal to $N/2$ whenever the fraction α is either 0 or 1, *coherent sampling*, or locally maximum whenever $\alpha = \alpha_{sub}$, as shown by (5.18) and (5.36) and depicted in Fig. 5.2 for a particular choice of the parameters. In particular it can be seen in 5.2 a) that two of the eigenvalues oscillate around the value $N/2$ while the third is constantly greater than or equal to N as α goes from 0 to 1 or equivalently f_0 goes from 750 Hz to 1000 Hz; This is a general behavior that does not depend on the particular parameters used for the simulation. Furthermore in 5.2 b) it can be observed that the smallest between λ_1 and λ_2 assumes its maximum value equal to $N/2$ when α is either 0 or 1, those

are the conditions of coherent sampling. The sub-optimum exists when the two eigenvalues are equal.
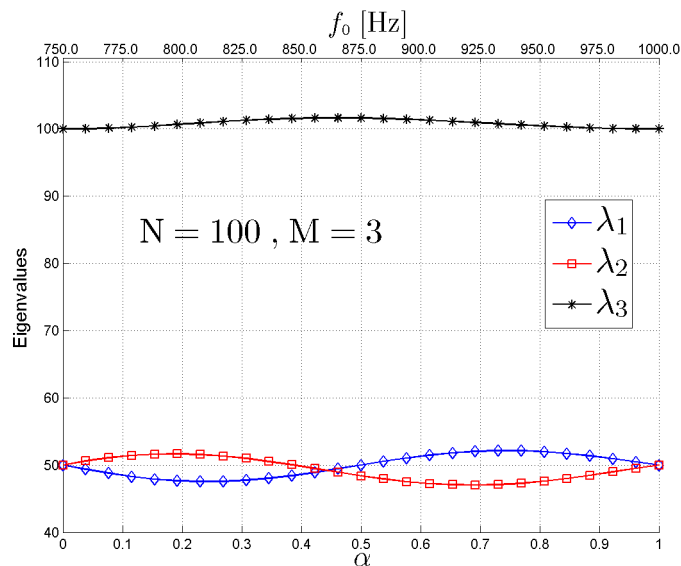
(a) Eigenvalues.
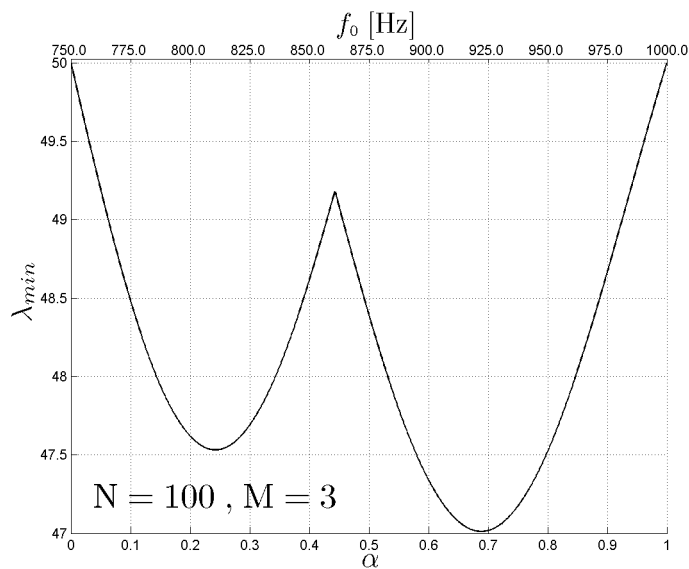
(b) Minimum Eigenvalue.

Figure 5.2: Eigenvalues of $\mathbf{D}^T\mathbf{D}$ vs α for $N = 100$ Samples, $M = 3$ Periods, $F_S = 25$ kS/s.

An integer number of periods means that all the dot products out of diagonal in (5.15) (from (A.15) to (A.17) in appendix A.2) are identically zero thus the matrix $\mathbf{D}^T\mathbf{D}$ is already diagonal. In particular the first two elements on the diagonal are equal to $\frac{N}{2}$ ((A.13) and (A.14) in appendix B) whereas the third is equal to N ((A.11) in A.2); therefore the *core matrix* has one eigenvalue of multiplicity 2 and one eigenvalue of multiplicity 1 and the pseudo-inverse gets a very simple form:

$$\mathbf{D}^\dagger = \left[\begin{array}{ccc} \frac{2}{N} & 0 & 0 \\ 0 & \frac{2}{N} & 0 \\ 0 & 0 & \frac{1}{N} \end{array}\right] \left[\begin{array}{c} \mathbf{c}^T \\ \mathbf{s}^T \\ \mathbf{1}^T \end{array}\right] \tag{5.37}$$

Since in the case of an integer number of periods acquired matrix $\mathbf{V}$ is the identity matrix, (5.34) can be rewritten as follows:

$$\mathbf{C} = \left[\begin{array}{ccc} \frac{2}{N}\sigma_{\mathrm{w}}^2 & 0 & 0 \\ 0 & \frac{2}{N}\sigma_{\mathrm{w}}^2 & 0 \\ 0 & 0 & \frac{1}{N}\sigma_{\mathrm{w}}^2 \end{array}\right] \tag{5.38}$$

thus it is straightforward to see that the components of $\widehat{\mathbf{x}}$ are uncorrelated when the additive noise is white. Furthermore if the input noise is also Gaussian the components of the estimator $\widehat{\mathbf{x}}$ are also statistically independent since they are jointly Gaussian and uncorrelated [45]. The AWGN case is important since white Gaussian noise is actually a good model for the additive noise corrupting sampled data.

It has been shown in [46] that the noise $w(t)$, formed by the sum of zero mean white Gaussian noise $n(t)$, present at the input of the ADC, and zero mean uniform white noise $q(t)$ that models the quantization noise when no saturation occurs, is approximately WGN if the standard deviation of the input $n(t)$ white noise σ_n is greater than $0.4 \, \Delta$, $\Delta = FSR \, 2^{-b}$ being the quantization step, b the number of bits, FSR the full scale range of the

quantizer. In the practical implementation, the saturation-free condition has to be carefully checked to confidently use the results found.

5.4 Amplitude Estimation

The sine wave amplitude is given by the nonlinear relationship expressed by the first of (5.3) which defines the amplitude estimator as follows:

$$\widehat{A} = \sqrt{\widehat{A}_c^2 + \widehat{A}_s^2} \tag{5.39}$$

Under the AWGN hypothesis, or whenever the covariance matrix of the input noise is known, it is possible to characterize approximately the first two moments of the amplitude distribution in terms of the design parameters, whereas in the special case of the optimal parameters, it will be possible to exactly evaluate all moments as will be shown in the following.

By considering only the first two components of the estimator $\widehat{x}_1 = \widehat{A}_c$ and $\widehat{x}_2 = \widehat{A}_s$, with the respective expected values $\widetilde{x}_1$, $\widetilde{x}_2$, and a generic function $g(\widehat{x}_1, \widehat{x}_2)$ the approximated expressions of the first two moments can be written as in [45]:

$$
\begin{aligned}
E\left[g\left(\widehat{x}_1, \widehat{x}_2\right)\right] \approx{}& g\left(\widetilde{x}_1, \widetilde{x}_2\right) + \\
&+ \frac{1}{2}\left(\frac{\partial^2 g}{\partial \widehat{x}_1^2}C_{11} + 2\frac{\partial^2 g}{\partial \widehat{x}_1 \partial \widehat{x}_2}C_{12} + \frac{\partial^2 g}{\partial \widehat{x}_2^2}C_{22}\right)
\end{aligned}
\tag{5.40}
$$

$$
\begin{aligned}
E\left[g^2\left(\widehat{x}_1, \widehat{x}_2\right)\right] - E^2\left[g\left(\widehat{x}_1, \widehat{x}_2\right)\right] \approx{}& \left(\frac{\partial g}{\partial \widehat{x}_1}\right)^2 C_{11} + \left(\frac{\partial g}{\partial \widehat{x}_2}\right)^2 C_{22} + \\
&+ 2\frac{\partial g}{\partial \widehat{x}_1}\frac{\partial g}{\partial \widehat{x}_2}C_{12}
\end{aligned}
\tag{5.41}
$$

where $C_{11} = \sigma_{\hat{x}_1}^2$, $C_{22} = \sigma_{\hat{x}_2}^2$ and $C_{12} = E\left[\left(\hat{x}_1 - \widetilde{x}_1\right)\left(\hat{x}_2 - \widetilde{x}_2\right)\right]$ and all the partial derivatives are evaluated in the expected value of the variables, i.e. $\widetilde{x}_1$ and $\widetilde{x}_2$ respectively.

By means of (5.40) the expected value of the amplitude estimator can be evaluated and yields:

$$E\left[\hat{A}\right] \approx \sqrt{\widetilde{A}_c^2 + \widetilde{A}_c^2} + \frac{1}{2}\frac{\left(C_{11} + C_{22} - \frac{\widetilde{A}_c^2 C_{11} + \widetilde{A}_s^2 C_{22} + 2\widetilde{A}_c\widetilde{A}_s C_{12}}{\widetilde{A}_c^2 + \widetilde{A}_s^2}\right)}{\sqrt{\widetilde{A}_c^2 + \widetilde{A}_c^2}} \tag{5.42}$$

Its variance can be evaluated by means of (5.41) and yields:

$$\sigma_{\hat{A}}^2 \approx \frac{\widetilde{A}_c^2 C_{11} + \widetilde{A}_s^2 C_{22} + 2\widetilde{A}_c\widetilde{A}_s C_{12}}{\widetilde{A}_c^2 + \widetilde{A}_s^2} \tag{5.43}$$

Denoting the kth element of the jth eigenvector $\mathbf{v}_j$ as v_j^k the generic element of the linear estimator $\widetilde{\mathbf{x}}$ covariance matrix is expressed by the following equation:

$$C_{ij} = \sigma_{\mathbf{w}}^2 \sum_{k=1}^{3} \frac{v_i^k v_j^k}{\sigma_k^2} = \sigma_{\mathbf{w}}^2 \sum_{k=1}^{3} \frac{v_i^k v_j^k}{\lambda_k} \tag{5.44}$$

Equation (5.44) together with (5.42) and (5.43) allow the evaluation of approximated expected value and variance of the amplitude estimator in presence of additive white noise, or any other statistics assuming the noise to be also Gaussian.

Furthermore, in that last case, for an integer number of periods acquired considering once more the first two components only of the estimator, it can be seen that they are independent, Gaussian and homoscedastic with expected values $\widetilde{A}_c$ and $\widetilde{A}_s$ respectively and common variance $\frac{2}{N}\sigma_{\mathbf{w}}^2$; the estimator $\hat{A}$ of the amplitude has therefore a Rice distribution, with parameters

$\nu = \sqrt{\widetilde{A}_c^2 + \widetilde{A}_s^2} = \widetilde{A}$ and $\sigma = \sqrt{\frac{2}{N}}\sigma_{\mathbf{w}}$:

$$f_{\widehat{A}}(a, \nu, \sigma) = \frac{a}{\sigma^2} e^{-\left(\frac{a^2 + \nu^2}{2\sigma^2}\right)} \mathrm{I}_0\left(\frac{a\nu}{\sigma^2}\right) u(a) \tag{5.45}$$

where $I_0(.)$ is the modified Bessel function of the first kind and order 0 and $u(.)$ is the Heaviside step function. For this distribution all the moments are known analytically, in particular mean and variance are expressed by the following equations:

$$\mu_{\widehat{A}} = \sigma\sqrt{\frac{\pi}{2}} L_{1/2}\left(-\frac{\widetilde{A}^2}{2\sigma^2}\right) \tag{5.46}$$

$$\sigma_{\widehat{A}}^2 = 2\sigma^2 + \nu^2 - \frac{\pi}{2}\sigma^2 L_{1/2}^2\left(-\frac{\widetilde{A}^2}{2\sigma^2}\right) = 2\sigma^2 + \widetilde{A}^2 - \mu_{\widehat{A}}^2 \tag{5.47}$$

where $L_{1/2}(.)$ is the generalized Laguerre polynomial of order $\frac{1}{2}$. The Laguerre polynomial is expressed by the following equation:

$$L_{1/2}(z) = e^{\frac{z}{2}}\left[(1-z)\mathrm{I}_0\left(-\frac{z}{2}\right) - z\mathrm{I}_1\left(-\frac{z}{2}\right)\right] \tag{5.48}$$

When the negative argument z is large enough the following asymptotic behaviour holds for the Bessel functions [47]:

$$\mathrm{I}_\beta(z) = \frac{e^z}{\sqrt{2\pi z}}\left[1 + \frac{(1-2\beta)(1+2\beta)}{8z} + \dots\right] \tag{5.49}$$

By defining the signal-to-noise ratio SNR as the mean-free average signal power divided by the average noise power, by means of (5.22), the SNR at the input of the algorithm can be evaluated as follows:

$$\mathrm{SNR}_{in} = \frac{\widetilde{A}^2}{2\sigma_{\mathbf{w}}^2} \tag{5.50}$$

It's interesting to note that the z variable in (5.48) and (5.49) is hence related to the signal-to-noise ratio at the input of the algorithm by the following relationship:

$$z = -\frac{N}{2}\text{SNR}_{in} \tag{5.51}$$

The condition of large z can be therefore always met by increasing the number of acquired samples N, no matters the value of SNR_{in}.

By neglecting the terms of higher order with respect to σ^2, the following asymptotic behaviour for the expected value and the variance of the amplitude estimator can be deducted:

$$\mu_{\widehat{A}} \approx \nu + \frac{1}{2}\frac{\sigma^2}{\nu} = \widetilde{A} + \frac{1}{N}\frac{\sigma_{\mathbf{w}}^2}{\widetilde{A}} \tag{5.52}$$

$$\sigma_{\widehat{A}}^2 \approx \sigma^2 = \frac{2}{N}\sigma_{\mathbf{w}}^2 \tag{5.53}$$

Equations (5.46) and (5.47) which generalize the results found in [40], or the approximated ones (5.52) and (5.53), suggest the possibility of a correction scheme for the amplitude estimation when a measurement, or an estimation, of its variance is available.

By considering indeed an estimation $s_{\widehat{A}}^2$ of the variance of the estimator $\widehat{A}$ and an estimation $\mu_{\widehat{A}}$ of its mean, an unbiased estimator $\widehat{A}_u$ of the sine wave amplitude can be built:

$$\widehat{A}_u = \frac{1}{2}\left(\mu_{\widehat{A}} + \sqrt{\mu_{\widehat{A}}^2 - 2s_{\widehat{A}}^2}\right) \approx \widetilde{A} \tag{5.54}$$

5.4.1 Frequency Analytical Characterization

Up to now the pseudo-inverse three-parameter sine fit has been characterized with respect to additive input noise; in this Section, the characterization of the algorithm is carried out with respect to the frequency of the input signal. In [28] an approximated closed-form expression of the *frequency response* of the algorithm $A_{f_0}(f) = |\mathrm{sinc}\,[(f - f_0)\,N/F_S]|$ has already been found by using a continuous time limit for an integer number of periods acquired.

Here, the frequency behavior is investigated in the proper framework of discrete time and a rigorous closed form expression is derived in the optimal case when an integer number of periods is acquired. The most general case can be studied by means of both the eigenvalues and the eigenvectors of the matrix $\mathbf{D}^T\mathbf{D}$ whereas in the optimal case only the eigenvalues are needed; in that case the pseudo-inverse operator is expressed by (5.37). Hence after a generic sine wave of unity amplitude $b(t) = \sin 2\pi f t$ is going to be considered as the input of the algorithm. The generic sine wave $b(t)$ can be rewritten in terms of its components at frequency f_0 as in the following:

$$
\begin{aligned}
b(t) &= \sin 2\pi f t = \sin\left[2\pi\left(f - f_0\right)t\right]\cos 2\pi f_0 t + \\
&+ \cos\left[2\pi\left(f - f_0\right)t\right]\sin 2\pi f_0 t
\end{aligned}
\tag{5.55}
$$

Since an integer number of periods to be acquired within the N samples is considered here the following relationship holds:

$$
\frac{M}{f_0} = \frac{N}{F_S}
\tag{5.56}
$$

The generic frequency f can be expressed as a function of the sampling frequency F_S as follows:

$$f = \frac{M + Q + \delta}{N} F_S \tag{5.57}$$

where $M + Q$ is the integer part and δ is the non-integer fraction. Q being positive or negative allows the expression of any frequency by means of (5.57).

Considering that $(f - f_0) = \frac{Q+\delta}{N} F_S$, the kth component $b_{k=0,1...,N-1}$ of the generic sine wave input vector $\mathbf{b}$ can be written as:

$$
\begin{aligned}
b_k &= \sin\left[2\pi \left(Q + \delta\right) \frac{k}{N}\right] \cos\left(2\pi M \frac{k}{N}\right) + \\
&+ \cos\left[2\pi \left(Q + \delta\right) \frac{k}{N}\right] \sin\left(2\pi M \frac{k}{N}\right)
\end{aligned}
\tag{5.58}
$$

By applying (5.37) the amplitude can be written as:

$$A = \sqrt{\left(\frac{2}{N}\mathbf{c}^T\mathbf{b}\right)^2 + \left(\frac{2}{N}\mathbf{s}^T\mathbf{b}\right)^2} = \frac{2}{N}\sqrt{(\mathbf{c}^T\mathbf{b})^2 + (\mathbf{s}^T\mathbf{b})^2} \tag{5.59}$$

thus in the optimal case to evaluate the amplitude as a function of the input frequency it suffices to evaluate only the dot product between the cosine and sine vectors at frequency f_0 and the input vector.

By introducing the angles:

$$
\begin{cases}
\phi = \pi \left(Q + \delta\right) \\
\theta = \pi M
\end{cases}
\tag{5.60}
$$

the dot products can be expressed by the following expressions.

$$
\begin{cases}
\mathbf{c}^T\mathbf{b} = \frac{1}{2}\frac{\sin\phi \sin\frac{N-1}{N}\phi}{\sin\frac{\phi}{N}} + \frac{1}{2}\frac{\sin(\phi+2\theta)\sin\frac{N-1}{N}(\phi+2\theta)}{\sin\frac{\phi+2\theta}{N}} \\
\mathbf{s}^T\mathbf{b} = \frac{1}{2}\frac{\sin\phi \cos\frac{N-1}{N}\phi}{\sin\frac{\phi}{N}} - \frac{1}{2}\frac{\sin(\phi+2\theta)\cos\frac{N-1}{N}(\phi+2\theta)}{\sin\frac{\phi+2\theta}{N}}
\end{cases}
\tag{5.61}
$$

With the aid of the following auxiliary variables:

$$\begin{cases} S_1 = \frac{\sin\phi}{\sin(\phi/N)} \\ S_2 = \frac{\sin(\phi+2\theta)}{\sin[(\phi+2\theta)/N]} \\ \gamma_1 = \frac{N-1}{N}\phi \\ \gamma_2 = \frac{N-1}{N}(\phi+2\theta) \end{cases} \tag{5.62}$$

the dot products in (5.61) can be rewritten as in (5.63).

$$\begin{cases} \mathbf{c}^T\mathbf{b} = \frac{1}{2}(S_1\sin\gamma_1 + S_2\sin\gamma_2) \\ \mathbf{s}^T\mathbf{b} = \frac{1}{2}(S_1\cos\gamma_1 - S_2\cos\gamma_2) \end{cases} \tag{5.63}$$

Eventually the amplitude is given by the following general expression:

$$A = \frac{1}{N}\sqrt{S_1^2 + S_2^2 - 2S_1 S_2 \cos(\gamma_1 + \gamma_2)} \tag{5.64}$$

Equation (5.64) is rigorous; nevertheless an easier to use approximation can be found whenever the following conditions are met:

$$\begin{cases} \frac{\phi}{N} << 1 \\ \frac{\phi+2\theta}{N} << 1 \end{cases} \tag{5.65}$$

In these conditions, the sine can be approximated by its argument thus $S_1 \approx N\frac{\sin\phi}{\phi}$ and $S_2 \approx N\frac{\sin(\phi+2\theta)}{(\phi+2\theta)}$; by applying now the formulas (5.60) the approximated expression of the amplitude as a function of the design parameters can be written:

$$A_{f_0}(f) = \Big[\ \mathrm{sinc}^2(Q+\delta) + \mathrm{sinc}^2(Q+2M+\delta) - $$
$$-2\,\mathrm{sinc}(Q+\delta)\,\mathrm{sinc}(Q+2M+\delta)\cos(\gamma_1+\gamma_2)\Big]^{\frac{1}{2}} \tag{5.66}$$

Equation (5.66) can be rewritten directly in terms of the design frequency f_0, its difference with respect to the actual one $\Delta f = f - f_0$ and the frequency bin $\Delta f_0 = \frac{F_S}{N}$ as:

$$A_{f_0}(f) = \left[\operatorname{sinc}^2\left(\frac{\Delta f}{\Delta f_0}\right) + \operatorname{sinc}^2\left(M + \frac{\Delta f}{\Delta f_0}\right) - \right.$$
$$\left. -2 \operatorname{sinc}\left(\frac{\Delta f}{\Delta f_0}\right) \operatorname{sinc}\left(2M + \frac{\Delta f}{\Delta f_0}\right) \cos\left(\gamma_1 + \gamma_2\right) \right]^{\frac{1}{2}} \quad (5.67)$$

Equation (5.67), as well as Fig. 5.3, clearly shows that the continuous time approximation $A_{f_0}(f) = |\operatorname{sinc}\left[(f - f_0)\,N/F_S\right]|$ holds very well, even though for very small values of N it can be inadequate; the goodness of the approximation can be evaluated by means of (5.64).

In Fig. 5.3, the different contributions introduced in (5.67) to the frequency response are illustrated. In particular, in 5.3 a) it can be seen that the error between the exact and the approximated frequency response is negligible for frequencies even far from f_0 up to ± 50 %; in 5.3 b) the different contributions of the approximated expression (5.66) are shown in order to that the approximation holds: in blue ($\times$) $\operatorname{sinc}^2\left(\frac{f-f_0}{F_S}N\right)$, in red ($*$) $\operatorname{sinc}^2\left(M + \frac{f-f_0}{F_S}N\right)$ and in black ($\cdot$) $\left|2 \operatorname{sinc}\left(N\frac{f-f_0}{F_S}\right) \operatorname{sinc}\left(2M + N\frac{f-f_0}{F_S}\right) \cos\left[2\pi\frac{N-1}{N}\left(M + \frac{f-f_0}{F_S}\right)\right]\right|$. It can be also seen that the blue curve is pretty smooth around f_0, thus small frequency drifts from the nominal frequency are not critical. It's worth noting that, no matter which expression is considered, a sinusoidal input signal whose frequency is separated from the design frequency f_0 by an integer number of frequency bins Δf_0 gives no contribution whatsoever to the amplitude estimate. This result holds under the only hypothesis of an integer number of periods acquired within the N samples.
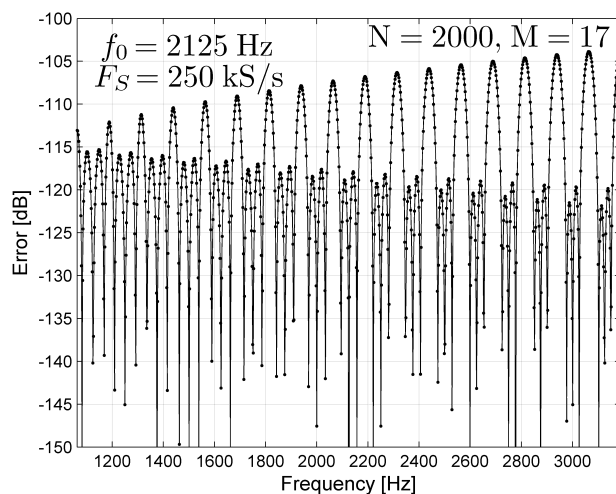
(a) Error between the actual, (5.64), and the approximated, (5.66), frequency responses.
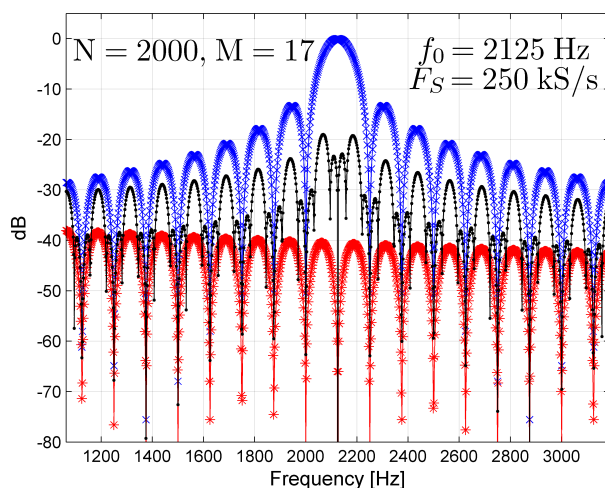
(b) Different contributions of the approximated frequency response.

Figure 5.3: Frequency behaviour of the algorithm for a particular choice of the design parameters.

5.5 Design of the Instrument Core Algorithm

The properties of the amplitude estimation by means of the three-parameter sin fit analyzed up to now are successfully applied in the the design of the

amplitude estimator of the secondary voltages of the LVDTs at the heart of the *PRS*. The first important feature for the design of the core algorithm of the instrument is that, for each LVDT, the frequency f_0 is known, therefore the matrix $\mathbf{D}$ in (5.13) can be calculated, and pseudo-inverted, just once per sensor off-line. Thus only matrix multiplications are needed. Another crucial feature of the computational optimization of the amplitude estimation is that matrix $\mathbf{D}$ can be simplified into an $(N \times 2)$ $\mathbf{D_0}$ matrix instead of an $(N \times 3)$ one since suitable frequency and number of samples are used leading to *coherent sampling*. Indeed, in 5.3.1, it has been proven that the covariance matrix defined in equation 5.28 is diagonal (5.34). Therefore, the estimation of the DC component is not carrying any information about the phase and the amplitude of the considered sinusoidal signal. For a single secondary channel this simplification yields:

$$\mathbf{D_0} = \begin{bmatrix} \cos(2\pi f_0 t_0) & \sin(2\pi f_0 t_0) \\ \cos(2\pi f_0 t_1) & \sin(2\pi f_0 t_1) \\ \vdots & \vdots \\ \cos(2\pi f_0 t_{N-1}) & \sin(2\pi f_0 t_{N-1}) \end{bmatrix} \quad , \quad \mathbf{x} = \begin{bmatrix} A_c \\ A_s \end{bmatrix} \tag{5.68}$$

Finally, since coherent sampling is used, choosing the frequencies of the different LVDTs, up to 7, that equip a collimator and that share the same multi-wire cable, to be orthogonal with respect to the three-parameter sine fit algorithm, potential cross talks are avoided by design. In general, for L LVDTs an $N \times 2L$ matrix has to be created and pseudo-inverted:

$$\mathbf{D}_L = [\mathbf{c}_{f_1} \mathbf{s}_{f_1} \ldots \mathbf{c}_{f_L} \mathbf{s}_{f_L}] \tag{5.69}$$

where:

$$\mathbf{c}_{f_j} = \begin{bmatrix} \cos(2\pi\frac{f_j}{f_s}) \\ \cos(2\pi\frac{2f_j}{f_s}) \\ \vdots \\ \cos(2\pi\frac{Nf_j}{f_s}) \end{bmatrix} \quad , \quad \mathbf{s}_{f_j} = \begin{bmatrix} \sin(2\pi\frac{f_j}{f_s}) \\ \sin(2\pi\frac{2f_j}{f_s}) \\ \vdots \\ \sin(2\pi\frac{Nf_j}{f_s}) \end{bmatrix} \tag{5.70}$$

The data coming from the acquisition boards, sampled at a frequency f_s, are stored in an $(N \times 2L)$ matrix and then multiplied with the matrix $\mathbf{D}_L^\dagger$, the pseudo-inverse of matrix (5.68), thus, at each survey cycle, a simple matrix product is performed to produce a $(2L \times 2L)$ coefficients' matrix estimate. $2L$ sinusoidal signals can be in fact expressed by the following equation:

$$\mathbf{Y}_L = \mathbf{D}_L \mathbf{X}_L \tag{5.71}$$

where the amplitudes of *cosine* and *sine* components are written as in the following equations (5.72), (5.73).

$$\mathbf{X}_L = diag\left\{\mathbf{A}_{f_1}^{(s_1,s_2)}, \ldots, \mathbf{A}_{f_1}^{(s_1,s_2)}\right\} \tag{5.72}$$

$$\mathbf{A}_{f_j}^{(s_1,s_2)} = \begin{bmatrix} \mathbf{A}_{c_{f_j}}^{s_1} & \mathbf{A}_{c_{f_j}}^{s_2} \\ \mathbf{A}_{s_{f_j}}^{s_1} & \mathbf{A}_{s_{f_j}}^{s_2} \end{bmatrix} \tag{5.73}$$

Equation (5.71) relates ideal sinusoidal signals to their amplitudes, decomposed in *cosine* and *sine* components, while (5.72) describes the diagonal structure of the amplitudes' matrix in which each block, described by (5.73), gives contributions only for its own frequency. The superscript s_1 and s_2 refer to the first and the second secondary respectively. Eventually the *best* amplitudes' matrix estimate is given by:

$$\tilde{\mathbf{X}}_L = \mathbf{D}_L^\dagger \mathbf{Y}_L \tag{5.74}$$

Two acquisition boards are needed to sample all the LVDTs of a same collimator, respectively 8 channels on board A and 6 channels on board B. The demodulation scheme specified in (5.69)-(5.73) has therefore been split: two *SineFit* matrices are generated at startup pseudo-inverting one matrix for the 4 LVDTs connected to the board A, and one for the 3 LVDTs connected to the board B. At each reading cycle, two matrices come from the *DMA* to be multiplied with the fit matrices. In Fig. 5.4 the reading and survey task for a single collimator is described.
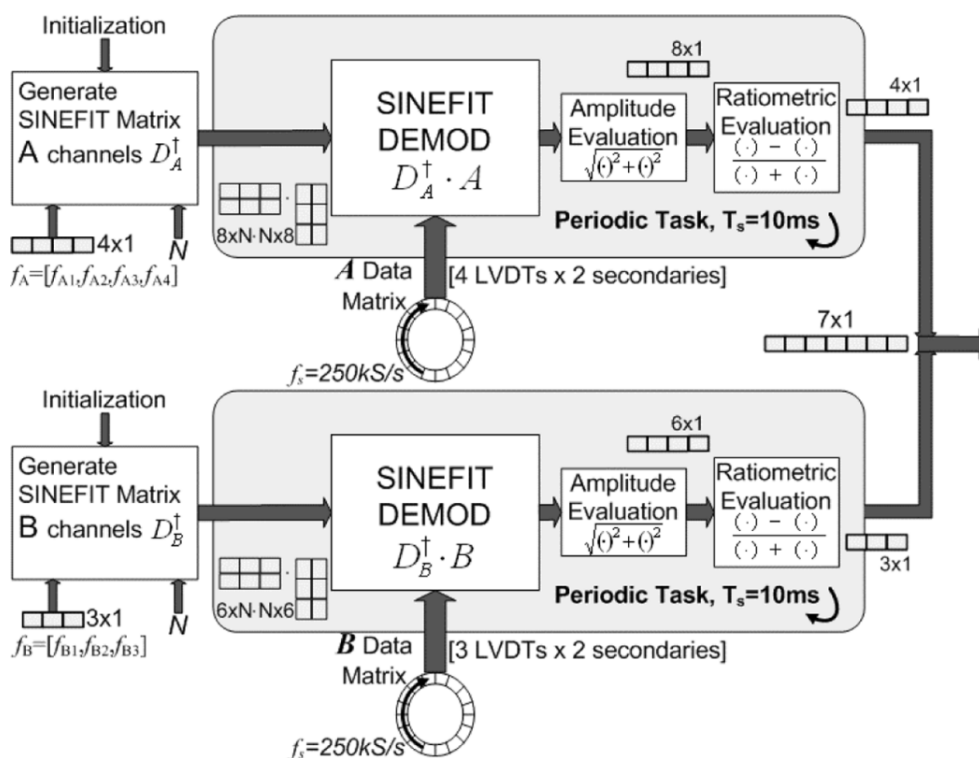
Figure 5.4: The Positioning Readout and Survey Task.

Chapter 6

Analysis of LVDT External Magnetic Field Interference

6.1 Interference Problem

For some collimators, installed in the *LHC* transfer lines from *SPS*, huge deviations of the positions measured by the *PRS* have been observed synchronously with the currents pulses of the resistive dipoles of the transfer lines. A typical installation of collimators in the transfer lines is shown in Fig. 6.1 where different cable trays are visible. Some of them accommodate water-cooled cables conducting currents whose typical profile is shown in Fig. 6.2.

A preliminary measurement of such deviation from the nominal position measurement, that is to say with no current pulses applied to the nearby magnets, is shown in Fig. 6.3 together with a measurement of the magnetic induction field components in the close proximity of the LVDT. Even with such preliminary measurement results of the magnetic flux density field impinging on the LVDT it is clear that the effect is proportional to the field intensity and not on its time derivative. Being such *external* fields pulsed and not purely DC, their effect cannot be corrected by a calibration oper-
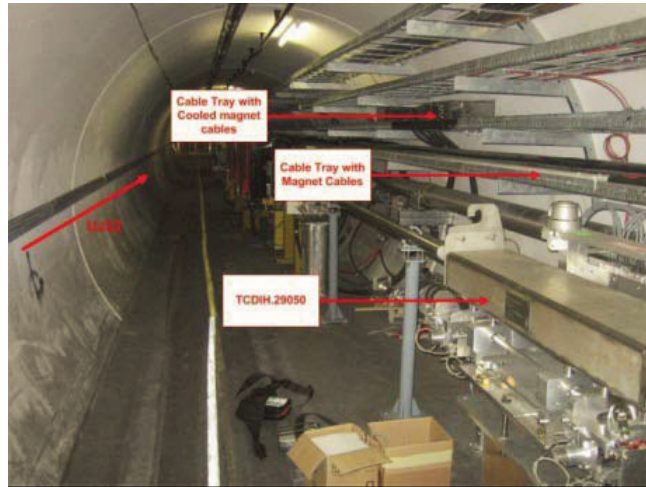
Figure 6.1: Typical installation of collimators in the *LHC* transfer lines.
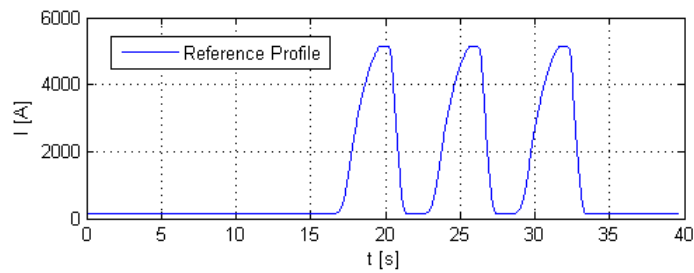
Figure 6.2: Reference current profile for the water-cooled cables in close proximity to collimators in transfer lines.

ated at a given value of the currents which makes the problem not easy to overcome. The amplitudes of the secondary voltages of the LVDT, measured by the *PRS*, are affected by the pulses (Fig. 6.4).

Measurement deviations of hundreds of μm are clearly unacceptable for *LHC* operation, especially at top nominal energy when the beam transverse dimension is circa 200 μm and the requirement for collimators positioning uncertainty is one tenth of that dimension.
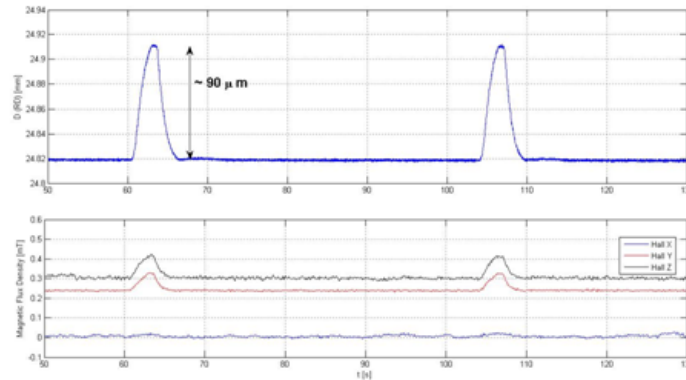
Figure 6.3: Typical profile of the magnetic interference on a collimator's jaw position measurement in TI2 transfer line.
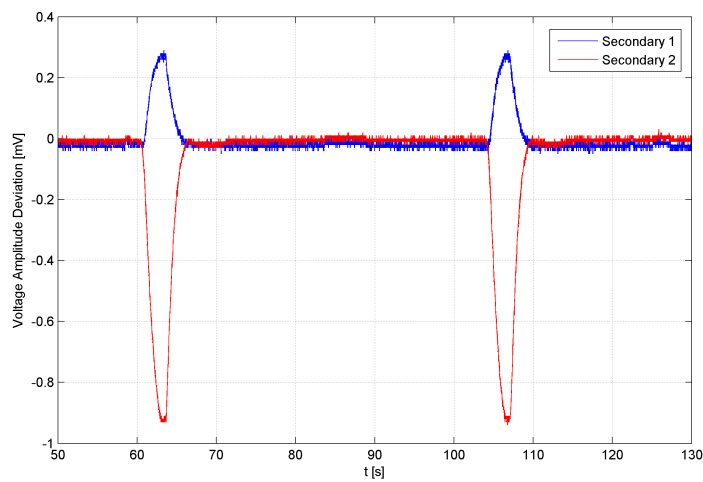
Figure 6.4: Deviation of the amplitudes of LVDT secondary voltages due to external pulsed magnetic field.

6.2 Strategy

The problem at stake has to be considered new in the literature about LVDT sensors. No more than a couple of datasheets mention magnetic fields as *influence quantities*, and even in those cases, no details are given whether magnetic fields are AC or DC. AC or fast pulsing magnetic fields are evi-

dently likely to affect the performance of the sensor as, more generally, any sudden variation of magnetic flux that can easily be captured by the LVDT; not so intuitive is how DC field or slowly varying ones come into play. It goes without saying that no quantitative characterization is available in the datasheets, thus the problem cannot be addressed by the measurement system designer during the design phase.

Given the novelty of the problem or, more specifically, the lack of useful technical knowledge about it, a general path comprising measurements, modeling and design phases, as illustrated in 6.5, has been followed along this thesis. Although each of the phases is deeply interconnected with the others in an iterative process, a methodological organization has been operated.
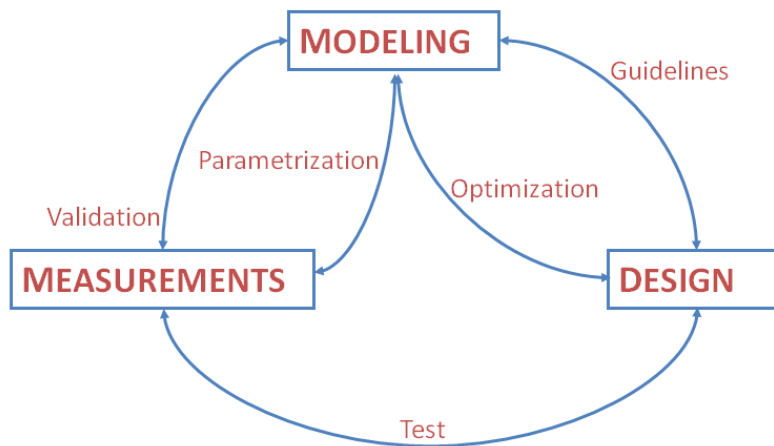
Figure 6.5: Conceptual Scheme of the Relationships between Measurements, Modeling and Design.

The first step consists in developing models of the interference starting from reasonable assumptions. Two different models have been proposed to characterize this phenomenon: an analytical, simplified, one aiming at capturing the main physics of the interaction and a more *quantitative* and accurate F.E.M. one. The next Sections (6.3) and (6.4) describe them in detail.

Following the path on the left in Fig. 6.5, Chapters 9 and 10 deal with their characterization and validation by means of simulation results. Eventually the experimental validation is developed along Chapters 14 and 15. Such validation required the conception of a suitable measurement method and the design and realization of an *ad hoc* measurement system: the method is presented in Section (6.5) whereas the detailed description of the actual measurement system together with its metrological characterization is described in Chapter 13.

Once validated, the models of the interference can be confidently used in the design of suitable solutions: moving now on the right of Fig. 6.5 design guidelines are proposed in Chapter 7 and then validated by means of simulation results in Chapter 11.

6.3   Simplified Analytical Model

The main interaction of an external DC magnetic field (i.e. slowly varying with respect to the excitation frequency) on the LVDT reading can be described by focusing on the nonlinear behaviour of the ferromagnetic materials that compose the different parts of the LVDT's magnetic circuit.

Actually the magnetic circuit is quite complex and can vary significantly from design to design. Here a very general approach is used for the modeling;

it can then be tailored according to the geometrical configuration of the actual sensor. The focus will therefore be on the nonlinearity of the core's material, since it has, by far, the highest permeability.

The rigorous description of the influence of an external magnetic field on the secondary voltages would require knowledge of the instantaneous magnetic flux linked to the secondary coils according to the equation (6.1) where S_{γ_i} is the surface of the secondary winding.

$$v_{s_i}(t) = \dot{\Phi}_{s_{\gamma_i}}(t) \tag{6.1}$$

The nature of the winding shape means that the surfaces S_{γ_i} can be considered as the union of the individual surfaces of each secondary turn. The total flux linked to the secondary coils is given by the sum of all the individual fluxes seen by each turn, which can vary since the magnetic flux density field is generally not uniform along the entire length of the coils. The flux is related to the flux density field by (6.2):

$$\Phi_{s_{\gamma_i}}(t) = \iint_{S_{\gamma_i}} \mathbf{B}(t) \cdot \mathbf{n}\, \mathrm{d}S = <B_n(t)>_{\gamma_i} S_{\gamma_i} \tag{6.2}$$

where $S_{\gamma_i} = N_{sec} S_{sec}$, where N_{sec} is the, common, number of turns of the secondary coils and S_{sec} is the cross sectional area of a single turn. $<B_n(t)>_{\gamma_i}$ has to be considered as the average normal component of the field over the cross section of all the individual turns that made up the coil. In this way the longitudinal nonuniformity of the field is taken into account and the instantaneous value of this averaged field is sufficient to describe the effect on the secondary voltages. From now on the magnetic flux density $\mathbf{B}$ will be assumed to being equal to the coil average field $<B_n(t)>_{\gamma_i}$.

6.3.1 Model of the magnetic field H

The main hypothesis, henceforth, is that the magnetic field $\mathbf{H}_{int}$ generated by the excitation circuit is purely sinusoidal. When an external magnetic field is present the overall magnetic field can be expressed as in the following equation (6.3):

$$\mathbf{H}(t) = \mathbf{H}_{ext}(t) + \mathbf{H}_{int}(t) = \mathbf{H}_{dc} + \mathbf{H}_{ac}\sin(2\pi f_0 t) \qquad (6.3)$$

Actually by means of $\mathbf{H}_{ext}$ and $\mathbf{H}_{int}$ it has been considered the effective field in a specified region which depend on the geometry of the LVDT and on the permeabilities of the different materials. It is explicitly assumed that:

- all the materials are isotropic thus the fields $\mathbf{H}$ and $\mathbf{B}$ are always parallel;

- the only ferromagnetic component inside the volume wrapped by the surfaces S_{γ_i} is the core, thus the only constitutive relationship to be considered is the one of the material the core is built of;

- $\mathbf{H}_{ext}$ is directed along the axis of the LVDT

The latter assumption is justified by the fact that the longitudinal component of the external field is, by far, the most significant one in terms of the effects on the secondary voltages [48].

Since the core has a cylindrical shape there will be a demagnetization effect which depends on the permeability and geometry of the core [49]. The magnetization $\mathbf{M}$ of the core will be assumed to being uniform thus the demagnetization factor will depend only on the geometry; by so doing the

purely sinusoidal shape of the magnetic field $\mathbf{H}_{int}$ in the region occupied by the core is preserved.

The time derivative of the flux density field $< B_n(t) >_{\gamma_i}$ is therefore expressed by:

$$\dot{B}_i(t) = \left.\frac{\partial B_i}{\partial H}\right|_{H=H(t)} \dot{H}(t) = \mu_d^{(i)}[H(t)]\dot{H}(t) \qquad (6.4)$$

In (6.4) the vector notation has been dropped and only scalar quantities have been considered. Furthermore (6.4) clearly states that whenever the quantity $\mu_d^{(i)}$, the "coil equivalent" differential permeability, depends on the magnetic field $H = H_{int} + H_{ext}$ then the time derivative of the magnetic flux density, and thus the voltages across the secondary coils, will change according to a variation in the magnetic field due to an external source.

6.3.2   Coil Equivalent Differential Permeability

The coil equivalent differential permeability that has been introduced can be modeled by averaging the fields over the different volumetric regions of the LVDT. In order to validate this approach the averaged differential magnetic permeabilities are modeled for both secondary coils considering ideal *linear* magnetic materials (for which $\mu = \mu_d$) and the results are compared with simulations performed by FLUX$^{\copyright}$ on an accurate F.E.M. model [50] in 9.1. Even though the assumption of ideal linear magnetic materials is not really realistic the aim, here, is to approximate the *intended behaviour* of the LVDT, that is to say the, approximatively linear, relationships between the amplitudes of the secondary voltages and the core position and not to develop a highly accurate model suited for LVDT's design. The nonlinearity of the magnetic materials will be therefore addressed afterwards when the focus

is moved to the dependence on the external magnetic field. This dependence is a *side effect* and is similar to the working principle of the fluxgate which is known to be a very sensitive magnetometer [51]. The first step is carried out, for a realistic LVDT geometry like the one sketched in Fig. 6.6 and Fig. 6.7, by considering the mutual inductances between the primary and the secondary coils as functions of the core position; the second step, in which the dependence on the core position is conversely completely discarded and only the core's material nonlinearity is taken into account, is described starting from subsection 6.3.3. The main parameters of the model are reported in Tab. 6.1 for the cross section and in Tab. 6.2 for the longitudinal section.
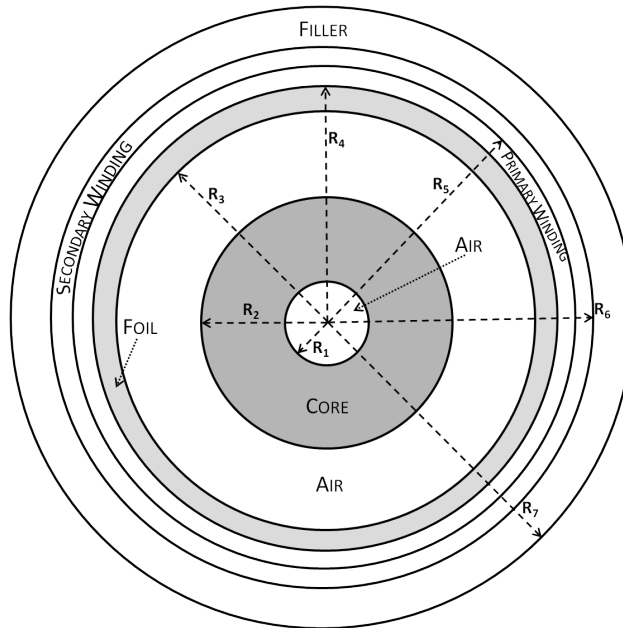
Figure 6.6: Cross section of the LVDT model used for the validation of the coil equivalent differential permeability (not in scale). Very thin air or not magnetic materials regions are not shown.

By assuming all the fields to be uniformly distributed and by averaging over the different 2-D regions, in Fig. 6.6 the following equations can be

written for the (differential) permeabilities of the secondary region where the core is present and when the core is absent respectively:

$$\mu_{sec}^{(core)} = \frac{\mu_0}{S_{sec}} \left[\frac{S_{core}\mu_r^{core}}{1 + \mathcal{N}\left(\mu_r^{core} - 1\right)} + \mu_r^{foil} S_{foil} + S_{air}^{int} + S_{air}^{ext} \right] \qquad (6.5)$$

$$\mu_{sec}^{(no\ core)} = \frac{\mu_0}{S_{sec}} \left(S_{nc} + \mu_r^{foil} S_{foil} \right) \qquad (6.6)$$

S_{air}^{int}	πR_1^2	Area of the internal air region
S_{core}	$\pi\left(R_2^2 - R_1^2\right)$	Area of the core region
S_{air}^{ext}	$\pi\left(R_3^2 - R_2^2\right)$	Area of the external air region
S_{foil}	$\pi\left(R_4^2 - R_3^2\right)$	Area of the foil region
S_{pri}	πR_{pri}^2	Area seen by the primary coil
S_{sec}	πR_{sec}^2	Area seen by the secondary coils
S_{nc}	πR_3^2	Area of the air in the region without core
R_{pri}	$\left(R_5 + R_4\right)/2$	Average radius of the primary coil
R_{sec}	$\left(R_6 + R_5\right)/2$	Average radius of the secondary coil

Table 6.1: Parameters of the Coil Equivalent Differential Permeability - Cross Section (Fig. 6.6)

In (6.5), it has been explicitly considered the demagnetization of the core whereas for the rest of the ferromagnetic parts these effects can be neglected since the regions foil-crowns-shield (Fig. 6.7) can be considered a (high permeability) continuum for the magnetic flux lines though small discontinuities in the magnetic permeability are present at the interfaces.

l_{pri}	Length of the primary coil
l_{sec}	Length of the secondary coil
l_{core}	Length of the core
s	Length of air gap between the secondary coils

Table 6.2: Parameters of the Coil Equivalent Differential Permeability - Longitudinal Section (Fig. 6.7)
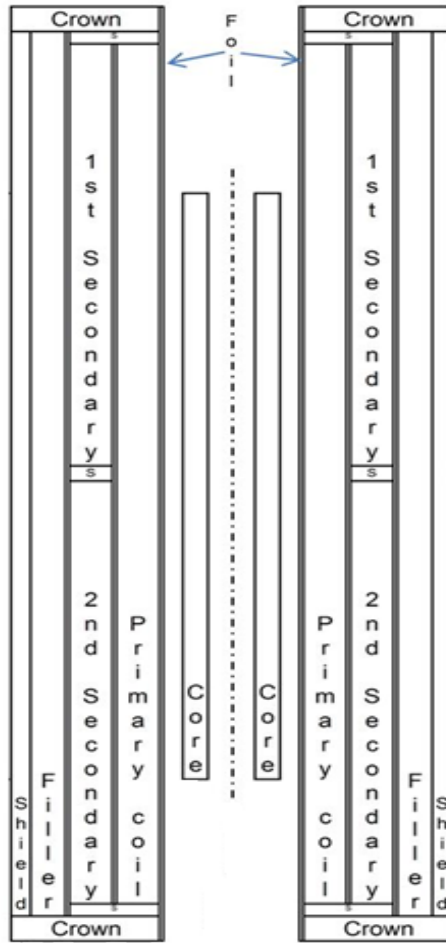
Figure 6.7: Longitudinal section of the LVDT model used for the validation of the coil equivalent differential permeability (not in scale).

The demagnetization in the core can be described, under the assumptions discussed in 6.3.1, by means of a simple demagnetization factor $\mathcal{N}$ [49]. Even though for an hollow cylinder there is no analytic exact formula, a good approximation is described by the following one [52]:

$$\mathcal{N} \approx \left(\frac{R_2}{l_{core}/2}\right)^2 \left[1 - \left(\frac{R_1}{R_2}\right)^2\right] \left(\ln \frac{2l_{core}}{R_2} - 1\right) \tag{6.7}$$

By defining x as the displacement between the geometric center of the core

and the geometric center of the LVDT, considered positive toward secondary 1, the following quantities measure the relative length of core *seen* by the two secondary coils:

$$\lambda_1 = \frac{1}{l_{sec}} \left[\frac{1}{2} \left(l_{core} - s \right) + x \right]$$
$$\lambda_2 = \frac{1}{l_{sec}} \left[\frac{1}{2} \left(l_{core} - s \right) - x \right] \tag{6.8}$$

By means of (6.8), together with (6.5) and (6.6) that act as an average in the cross section, it is possible to write the (volumetric) averaged coil equivalent permeabilities as:

$$\mu_{sec_1} = \lambda_1 \mu_{sec}^{(core)} + \left(1 - \lambda_1 \right) \mu_{sec}^{(no\ core)}$$
$$\mu_{sec_2} = \lambda_2 \mu_{sec}^{(core)} + \left(1 - \lambda_2 \right) \mu_{sec}^{(no\ core)} \tag{6.9}$$

Since for this analysis only constant magnetic permeabilities have been considered $\mu_{sec_i}(x) = \mu_d^{(i)}(x)$. The mutual inductances have been chosen because of the availability of direct coil inductance calculation in FLUX$^\copyright$ and mostly because, with sinusoidal current excitation, the amplitudes of the secondary voltages (which are purely sinusoidal signals at the excitation frequency) can be easily evaluated as:

$$A_{v_1}^{f_0}(x) = 2\pi f_0 M_{sec_1}(x) I_{pri}^{ac}$$
$$A_{v_2}^{f_0}(x) = 2\pi f_0 M_{sec_2}(x) I_{pri}^{ac} \tag{6.10}$$

Equations (6.10) directly relate the amplitudes of the secondary voltages with the core position by means of (9.1) for a given amplitude of the primary excitation current.

The coil equivalent differential permeability that has just been introduced will depend, in the most general case, on:

- the core geometry (the demagnetization factor depends strongly on the geometry);

- the permeability of the core material (whenever the magnetization cannot be considered uniform);

- the core position (to justify that a secondary coil senses its linked flux growing when the core moves toward it);

- the permeability of other ferromagnetic material enclosed by the secondary coil (in the most general case).

$$\mu_d^{(i)} = \mu_d^{(i)}(x, H) \tag{6.11}$$

In (6.11), by design, the dependence on x is intended and approximately linear whereas the dependence on H_{dc} is the side effect that can be significant. This side effect is indeed similar to the working principle of the fluxgate which is known to be a very sensitive magnetometer [51].

In order to get an equation that links the flux to the applied and external magnetic fields, additional hypotheses are now needed. When the past history of both B and H fields is known it is possible to write an equation like (6.4) each time the magnetic field is changing monotonically. At the very moment the derivative of the magnetic field changes sign a different differential permeability function has to be used: $\mu_d^{\uparrow} \neq \mu_d^{\downarrow}$.

Since the focus of this work is on the external slowly varying magnetic field whereas the internal AC one is somehow imposed by the current generator the effect of the AC hysteresis has not been taken into account.

Conversely for the external interfering magnetic field it will be explicitly considered that $\mu_d^\uparrow(H_{dc}) \neq \mu_d^\downarrow(H_{dc})$.

It is possible, now, to expand the differential permeability, determined by the underlying dynamics of the interfering field, in a Taylor's series around the external field H_{dc} considering $H = H_0 + \Delta H = H_{dc} + H_{ac}\sin(2\pi f_0 t)$ leading to the following equation:

$$\mu_d(H) = \mu_d(H_{dc}) + \sum_{n=1}^{\infty} \frac{1}{n!} \frac{\partial^n \mu_d}{\partial H^n}\bigg|_{H=H_{dc}} H_{ac}^n \, \sin^n(2\pi f_0 t) \qquad (6.12)$$

6.3.3 Harmonic expansion of the flux density time derivative

Using the Taylor's expansion (6.12), the derivative of the flux density can be written as:

$$\dot{B}_i = \mu_d^{(i)}(H)\dot{H} = 2\pi f_0 H_{ac}\cos(2\pi f_0 t) \, \cdot$$
$$\cdot \left[\mu_d^{(i)}(H_{dc}) + \sum_{n=1}^{\infty} \frac{1}{n!} \frac{\partial^n \mu_d^{(i)}}{\partial H^n}\bigg|_{H=H_{dc}} H_{ac}^n \, \sin^n(2\pi f_0 t) \right] \qquad (6.13)$$

Omitting the intermediate calculations and introducing the following auxiliary variables in order to simplify the notation:

$$\begin{cases} \delta_{cos}^{f_0}(n,k) & = \cos\left[(n-2k-1)2\pi f_0 t\right] + \\ & + \cos\left[(n-2k+1)2\pi f_0 t\right] \\ \delta_{sin}^{f_0}(n,k) & = \sin\left[(n-2k-1)2\pi f_0 t\right] + \\ & + \sin\left[(n-2k+1)2\pi f_0 t\right] \end{cases} \qquad (6.14)$$

$$\partial^n \mu_{dc}^{(i)} = \frac{\partial^n \mu_d^{(i)}}{\partial H^n}\bigg|_{H=H_{dc}} \tag{6.15}$$

the product $\sin^n(2\pi f_0 t)\cos(2\pi f_0 t)$ of (6.13) can be expanded.

$$\sin^n(2\pi f_0 t)\cos(2\pi f_0 t) = \frac{1}{2^n} \cdot \begin{cases} \sum_{k=0}^{\frac{n-1}{2}}(-1)^{(\frac{n-1}{2}-k)} \cdot \\ \cdot \binom{n}{k}\delta_{sin}^{f_0}(n,k) & n \text{ odd} \\ \binom{n}{\frac{n}{2}}\cos(2\pi f_0 t)+ \\ +\sum_{k=0}^{\frac{n}{2}-1}(-1)^{(\frac{n}{2}-k)} \cdot \\ \cdot \binom{n}{k}\delta_{cos}^{f_0}(n,k) & n \text{ even} \end{cases} \tag{6.16}$$

The harmonic expansion of the magnetic flux density is finally given by:

$$\dot{B}_i = 2\pi f_0 H_{ac}\bigg\{ \mu_d^{(i)}(H_{dc})\cos 2\pi f_0 t + \sum_{n \text{ even}} \frac{H_{ac}^n}{2^n}\frac{\partial^n \mu_{dc}^{(i)}}{n!} \cdot$$

$$\cdot \left[\binom{n}{\frac{n}{2}}\cos 2\pi f_0 t + \sum_{k=0}^{\frac{n}{2}-1}(-1)^{(\frac{n}{2}-k)}\binom{n}{k}\delta_{cos}^{f_0}(n,k) \right] +$$

$$+ \sum_{n \text{ odd}} \frac{H_{ac}^n}{2^n}\frac{\partial^n \mu_{dc}^{(i)}}{n!}\sum_{k=0}^{\frac{n-1}{2}}(-1)^{(\frac{n-1}{2}-k)}\binom{n}{k}\delta_{sin}^{f_0}(n,k) \bigg\} \tag{6.17}$$

6.3.4 The amplitude of the first harmonic of the secondary voltages

The secondary voltage v_i, given by $\dot{B}_i S_{\gamma_i} = \dot{B}_i N_{sec} S_{sec}$, hence has several harmonics whereas the only one used in the ratiometric evaluation, as well as in many different conditioning techniques, is the one at the excitation frequency f_0. Selecting the suitable summation index in (6.17) the amplitude of this component of the secondary voltages v_i can be easily evaluated as:

$$A_{v_i}^{f_0} = 2\pi f_0 H_{ac} S_{\gamma_i}\left| \mu_d^{(i)}(H_{dc}) + \sum_{n \text{ even}} \frac{H_{ac}^n}{2^n}\frac{\partial^n \mu_{dc}^{(i)}}{\left(\frac{n}{2}\right)!\left(\frac{n}{2}+1\right)!} \right| \tag{6.18}$$

It worths noting that the coefficient $2^n \left(\frac{n}{2}\right)! \left(\frac{n}{2} + 1\right)!$ appearing in the denominator in (6.18) grows very fast as the order of the expansion n increases, thus by truncating (6.18) at the first order it yelds:

$$A_{v_i}^{f_0} \approx 2\pi f_0 H_{ac} S_{\gamma_i} \left| \mu_d^{(i)}(H_{dc}) \right| \tag{6.19}$$

Equation (6.19) shows that the amplitude of the first harmonic of the voltage of secondary i is approximately proportional to the equivalent differential permeability $\mu_d^{(i)}$ of that coil evaluated in the external slowly varying field H_{dc}.

6.4 Finite Elements Method Model

An F.E.M. model of the interference has been developed using the simulation software FLUX$^{\copyright}$. This simulator is particularly suited for the finite element analysis of electromagnetic problems involving 2D and 3D geometries [53]. The F.E.M. simulator FLUX$^{\copyright}$ from *CEDRAT Technologies* has been used, as it is particularly suited for solving electromagnetic problems involving movable parts, such as sensors, motors, and actuators [53]. In addition, it allows a deep investigation of flux distributions, end effects, nonlinearity, and non uniformity of field strength along the different magnetic elements [54], [55]. For ferromagnetic materials, FLUX works with nonlinear $B - H$ curves, but it does not consider hysteresis effects [53]. The purpose of such an F.E.M. analysis is to conceive a model of Linear Variable Differential Transformer and a simulation environment which can be used as tools for analysis and design of LVDT exposed to external magnetic fields. The availability of such a model would allow an immediate feedback in the analytical study of the physical phenomenon of the external magnetic fields influence on LVDT

reading, as well as in the design process of a LVDT-like structure with high immunity to external magnetic fields.

Since the external fields, such the one shown in Fig. 6.3, are slowly varying with respect to the frequency of the internal LVDT magnetic field, in the range of few kHz, at each reading of the instrument the interfering field can be confidently assumed constant. Therefore only DC fields will be considered.

6.4.1 2D Modeling

The LVDT geometry presents cylindrical symmetry. On the other hand, an interfering magnetic field impinging the LVDT structure can be in principle arbitrarily oriented. However, an arbitrarily oriented magnetic field can be seen as the superposition of longitudinal (parallel to the LVDT axis) and transversal (perpendicular to the axis) components. Given that such sensor is more sensitive to longitudinal magnetic fields [13], [12], this case is here considered. Thus, the simulation geometry has to include the sensor itself and an external longitudinal magnetic field source. Actually, the impinging magnetic field (the magnetic field generated by the external source when the LVDT is not present) can be uniform or nonuniform along the LVDT axis. For a first-step model, the interfering magnetic field has been chosen to be uniformly distributed along the axis and on the cross section. For this reason, the interfering magnetic field will exhibit a rotational symmetry too. Thus, the magnetic field source can be a solenoid. In this way, the whole structure has complete cylindrical symmetry and the simulation geometry can be built in two dimensions. In the actual model the primary coil is indeed wound on the entire length of the winding support, whereas the secondary coils are

wound over the primary, one of each side of the structure (Fig. 6.8). In this way the leakage inductances of the transformer are significantly reduced. The model presents insulator washers and layers, treated as nonmagnetic regions. The structure is enclosed in a ferromagnetic cylindrical case with two end
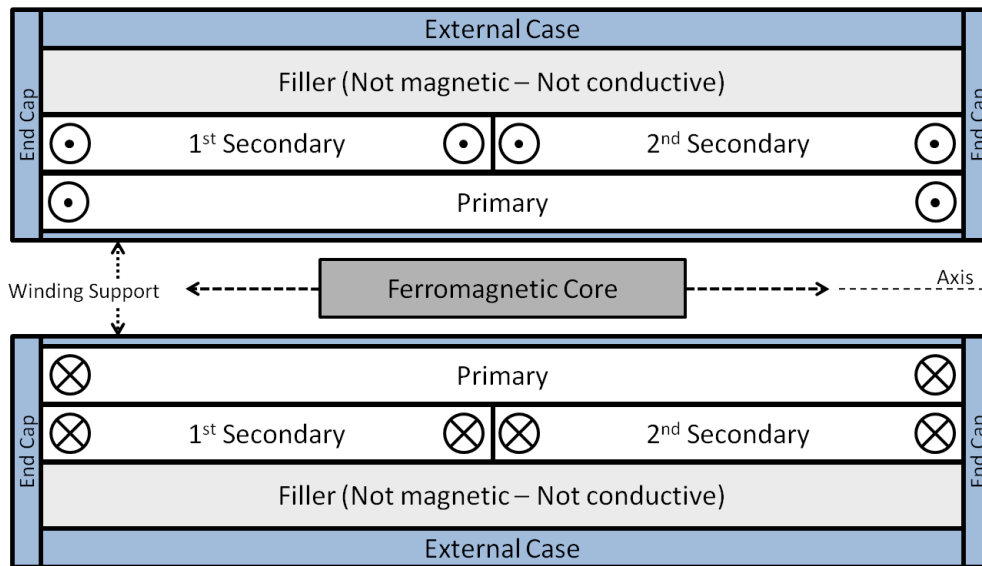
Figure 6.8: 2D Longitudinal scheme of the LVDT sensor F.E.M. model (not in scale).

caps. The ferromagnetic case, together with the end caps, has two main functions: it closes the LVDT magnetic circuit and acts like a first shielding against external magnetic fields. The core is a cylinder whose length is equal to the secondary coils length. Given the cylindrical symmetry, the simulation geometry takes into account only half of the longitudinal section of the sensor (Fig. 6.9). Actually, the complete 3D geometry is obtained by rotating the simulation geometry around the symmetry axis by 360 degrees (Fig. 6.9, in the infinite box a geometrical transformation is performed in order to simulate the infinite space [54]). However, even though the finite element analysis can be performed totally in the 2D environment, the results are

provided anyway for the whole volume of the device, resulting in a significant reduction of computational time.
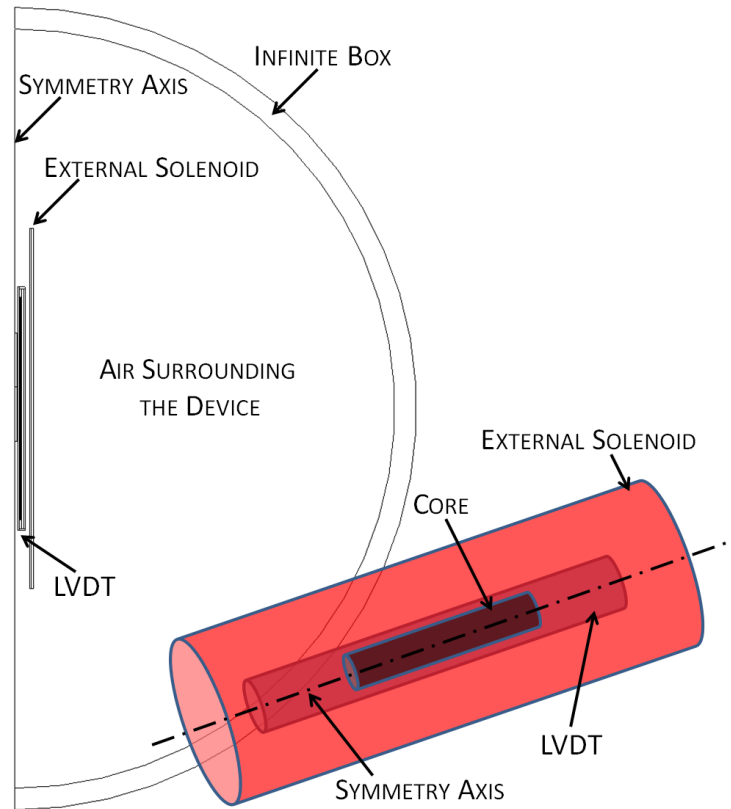
Figure 6.9: 2D Simulation geometry and 3D reconstruction.

The structure has a high aspect ratio, thus a fine mesh has been chosen in order to discretize the thicknesses, whereas the mesh along the length of the sensor can be coarser. By doing so, the mesh has been optimized using triangular elements on all the geometry. The meshing and the solving parameters for the geometry are reported in Tab. 6.3. The presence of a small amount of poor elements (i.e. nearly flat triangular elements), disposed axially, is not a concern; indeed in such a structure the variation of the fields in a single region is supposed to be more rapid in the transversal direction,

Info	Parameters
Mesh Type	2D Triangular Mesh
Mesh Order and Density	2nd Order, Non-uniform
General Meshing Rule	$3-4$ elements per thickness
Number of Poor Elements	2.8 %
Number of Nodes	≈ 43000
Solving Scenario	Time Transient
Target relative ϵ of the Newton-Raphson solver	1×10^{-4}
Maximum Number of Iterations	100
Solving time (no parameters except time)	24 minutes

Table 6.3: Mesh and Solving Information

rather than in the longitudinal one [56]. This assumption applies also to the regions of the structure between the coils and the external case, in which the poor elements are present. In addition, in the regions corresponding to the magnetic media, the mesh density has been adapted to the penetration depth. Being in principle the magnetic permeability a function of the magnetic field, the penetration depth has been calculated in the worst case (i.e. maximum permeability) and the meshing density arranged in order to have at least two meshing elements inside the skin depth area [53].

6.4.2 Magnetic Materials

The F.E.M. modeling of magnetic materials properties for the study of the LVDT magnetic interference is not trivial. As a matter of fact, given the presence of an external magnetic field superposed to the one due to the LVDT working principle, the materials magnetic properties have to be correctly described in all regions of the B - H plane for the simulations to closely match their actual behavior. Unfortunately, F.E.M. simulators model the

nonlinearity of magnetic materials by considering their normal magnetization curve, without taking into account major and minor hysteresis effects [53]. For these reasons, the materials which have been chosen for the magnetic parts of the LVDT sensor model had been through an annealing procedure. The preference of having annealed samples instead of not treated materials lies in the fact that in annealed state such samples exhibit high permeability and narrow hysteresis cycle [57], as well as an uniformly distributed magnetic permeability [22]. These properties make them more suitable to be modeled with a finite element approach. *PERMENORM 5000 H2* (50 % Ni-Fe alloy) has been chosen as core material, whereas ferromagnetic steel has been used for the cylindrical case, since these materials. Both of them had been through an annealing process. Regarding the coils specifications, a number of turns of 1500 has been chosen for the primary winding, in order to have a sufficiently high field inside the sensor, whereas a number of turns of 1600 has been chosen for both secondary coils, setting the transformation ratio.

6.4.3 Solving Strategy

The time transient solver has been chosen. The Newton-Raphson method is used for non-linear solving and a maximum number of 100 iterations is set for each time instant. The relaxation factors for this algorithm are calculated through the Fujiwara method [53]. Geometrical distances, including crucial parameters (for example, the core displacement) have been parameterized in order to allow rapid parametric simulations embedded in the same simulation scenario. The numerical transients have been avoided by using an initialization by static computation [53]. On the other hand, for each simulation, an adequate time window has been chosen for the time transient computation,

in order to avoid physical transient phenomena. The parameterization of the core displacement allows performing a set of simulations at different core positions. For each of them, the geometry is re-meshed and the time transient computation performed [53]. The core position range which has been set goes from $-20\ mm$ to $20\ mm$ in 11 steps with constant spacing. By doing so, the simulation in standard working conditions results in the sensor's calibration. For the interfering field simulation, taking critical installations as an example [35], [48], the case of a $1\ mT$ external magnetic flux density has been considered, which in air corresponds to an interfering magnetic field of about $800\ A/m$. The magnetic field is axially oriented and spatially uniform.

6.5 Measurement Method

A well-defined procedure has been developed for measuring the output characteristic of the sensor. According to its design and its available wires, a differential or a ratiometric reading [27], [58], [59] , [60] is used, and the nonlinearity and uncertainty of the sensor are given. Then, the procedure is detailed to analyze the sensor under test in the presence of an external magnetic field on the LVDT. The method aims at evaluating the accuracy reduction of an LVDT due to magnetic interference. The procedure is proposed as a reference to test the LVDT sensors in the presence of an external magnetic field. An automatic test bench implements this procedure and has been improved with respect to that in [61] in order to be exploited as a tool to find an optimal supplying excitation and a reading technique under which immunity of a given sensor to interference is maximized. Measurement conditions and procedures have been defined in order to fix a suitable method for different types of LVDT sensors. As far as the reading of the sensor is

concerned, the primary coil is fed by a voltage or a current sine waveform at a frequency ranging from 1 to 5 kHz. Although a few LVDTs are designed for operation at 60 Hz, excitation frequencies of 250 Hz to 10 kHz are more typical, with 1 kHz being the most common. Generally, a higher frequency is desired in order to have a faster response of the LVDT to variation in the position. A limiting factor, however, is that an excessively high frequency ($> 10~kHz$) leads to eddy current loss in the core and results in lower output signal level, more power dissipation, and greater temperature influence [22]. The amplitude value is chosen in order to have some units of Volts on the secondary coils. A high-resolution high-sampling rate data acquisition board, similar to the one employed in the PRS as presented in 4.3, is used to acquire the primary and both secondary waveforms, whose amplitudes are evaluated by applying the sine-fit algorithm on 2000 samples acquired at 250 kS/s. Then, the ratiometric reading function is applied, i.e.,the difference of the secondary voltage amplitudes over its sum ($(A_1 - A_2)/(A_1 + A_2)$). In case of a four-wire model, only the series bucking of the secondary coils is available; therefore, the reading technique suggested by the manufacturer is exploited (Fig. 6.10). The sensor is first calibrated without any interference magnetic field (Fig. 6.10). It is assumed that the sensor works in the position range $(-P, +P)$. Moving the core from position $-P$ to $+P$, a conversion table T is created between the array of position readings p_i and their corresponding ratiometric values r_i. The reference positions p_i are measured by another independent displacement sensor. At each position p_i, ($i = 1 \ldots N$, $N = 50$) repeated measurements are done to evaluate uncertainty u_i (Fig. 6.10). Then, the average of u_i is evaluated. It represents the uncertainty $u_{LVDT+read}$ of the LVDT sensor and the associated reading system. As a

matter of fact, the uncertainty of the sensor itself cannot be evaluated without the reading system; in fact, the reading system can be regarded as the transducer of the sensor. At this stage, nonlinearity NL is evaluated as well (see Fig. 6.10).
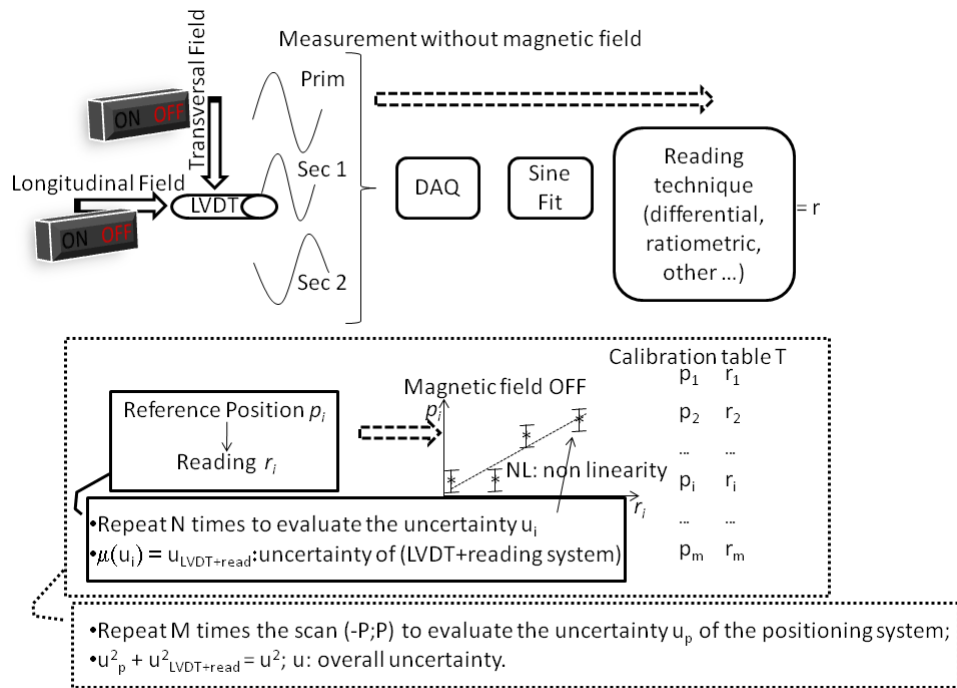
Figure 6.10: Chart of the measurement procedure without external magnetic field.

This procedure is then repeated ($M = 30$) times to evaluate the uncertainty of the overall system. In fact, moving the core M times between positions $-P$ and $+P$ allows evaluating uncertainty up of the positioning system by means of the external reference sensor. Evaluation of this figure is significant to compare more sensors and assess the effect of the external magnetic field. This point will be detailed in 13.2. Finally, composition of u_p and $u_{LVDT+read}$ gives the overall uncertainty u of the test bench and of

the LVDT under test (Fig. 6.10).
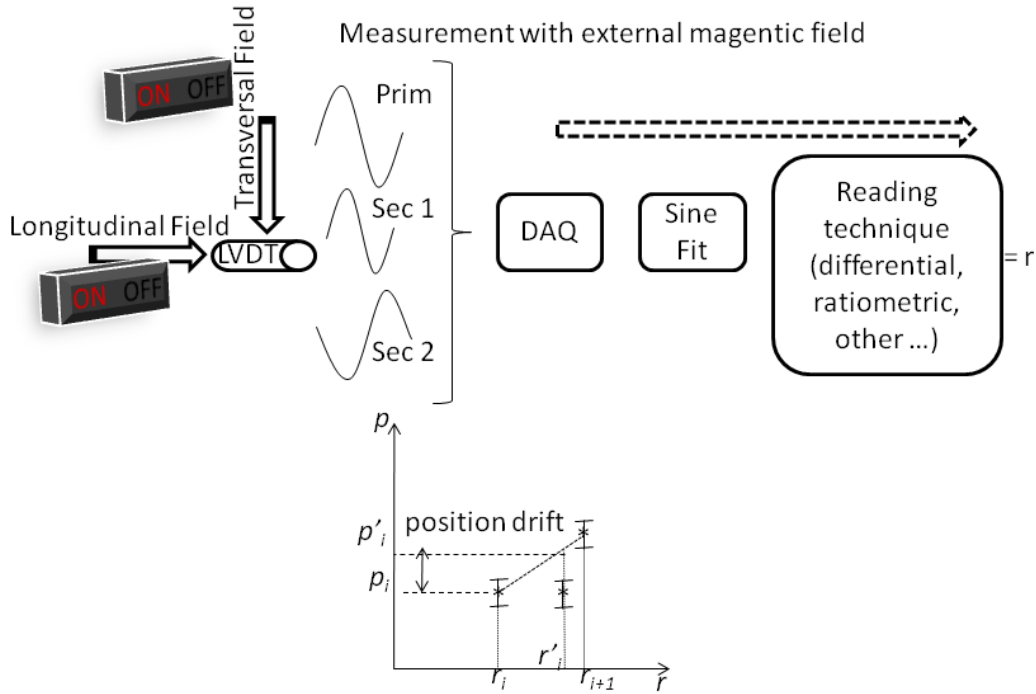
Figure 6.11: Position deviation is evaluated for the measurement with a magnetic field impinging on the LVDT structure.

The described procedure is then applied in the case of an external magnetic source. A new set of ratiometric values $r_i^{'}$ is measured and then converted in the position reading $p_i^{'}$ using the calibration table T (Fig. 6.11). The difference $p_i - p_i^{'}$, where p_i is the reference position read by another sensor, is the position measurement variation due to magnetic interference and chosen as figure of merit to evaluate the performance of the LVDT sensors in the presence of the external magnetic field. A transversal or a longitudinal magnetic field impacting uniformly on the LVDT sensor structure is considered as the external source (Fig. 6.11). They are separately applied, assuming that the effect of a field, impinging at any angle, can be always considered as the contribution of its transversal and axial components [48].

In particular, the transversal field is generated by means of a resistive magnet and the longitudinal one by means of a solenoid.

The evaluation of the position measurement variation is carried out as follows:

1. For a given position p_i and a maximum external field $|H|$, a first cycle from 0 to $|H|$ and then to $-|H|$ and back to $|H|$ is applied with no measurements.

2. An interfering magnetic field scan is performed by following the previous cycle, changing the field with step ΔH. For each magnetic field value, the ratiometric value r_i' is measured (over $N = 50$ repeated measurements).

3. A demagnetization procedure is performed.

4. The core is moved to position p_{i+1}.

The demagnetization procedure is a critical point of the measurement procedure. It is necessary to bring the core and the foil back to their initial magnetic state, before starting a measurement at a new position. If those magnetic parts of the LVDT are not correctly demagnetized, repeatability of the measurement conditions is not assured. Therefore, a demagnetization procedure is applied for each measurement with an external field of intensity $|H|$ at a given position p_i. Starting from the field value $|H|$, repeated magnetic cycles, with decreasing amplitude, are applied to demagnetize the sensor materials. The shape of the decreasing amplitude is depicted in Fig. 6.12. A linear shape was preferred to the exponential one chosen at the first stage [61] since the former assures a smoother decrease in the magnetic

field than exponential decay, above all at high values of H. This allowed improving the effectiveness of LVDT material demagnetization.
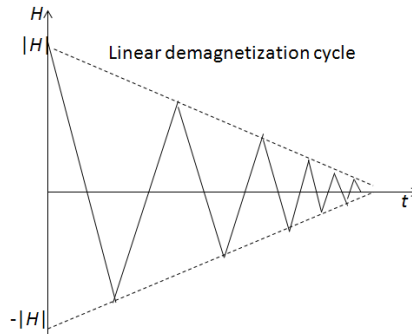
Figure 6.12: Amplitude shape of the applied magnetic field for the demagnetization cycle.

The value of the position reading before applying the external magnetic field $|H|$ and that after the measurement procedure and the demagnetization cycle are compared. If the difference between the aforementioned values is within the sensor's uncertainty, then the demagnetization procedure is considered successful otherwise, it is repeated.

Chapter 7

Design Guidelines for DC Polarization and Magnetic Shielding

In this Chapter, general design guidelines to drastically lessen the influence of external magnetic fields on LVDTs are outlined. They consist of an innovative multi-layer magnetic shielding and a tuned DC polarization of the primary circuit of an abstracted LVDT.

Thus for the purpose of this Chapter, the LVDT design is not referred to a specific commercial sensor, thus only the typical LVDT parameters such as sensitivity and primary voltage excitation are taken into account. The geometrical dimensions are purely indicative. A maximum interfering magnetic field of 800 A/m (approximately 1 mT of magnetic flux density in air) has been considered (maximum intensity experienced by the collimators in LHC Transfer Lines). Anyway, the design guidelines discussed here can be easily applied to stronger interference cases. The target is to reduce the effect of the external field such that the position sensor uncertainty must be contained within ± 20 μm. The rejection of the longitudinal interfering magnetic field is to be obtained by means of a proper designed shield and further enhanced

by applying a DC polarization of the magnetic media.

7.1 Simulation Model Description

A general model of the LVDT and its environment, as well as a simulation strategy were conceived by means of the F.E.M. tools discussed in Chapter 6. They aim at evaluating not only the shield efficiency of the proposed design but also at reproducing the interference problem for its successive validation.

The primary coil is wound along the entire length of the sensor under study (about 110 mm), whereas the secondary windings are wound over the primary, one on each side of the bobbin. The ferromagnetic core is a hollow cylinder whose length matches the one of the secondary windings (about 50 mm). The core is made up of *Alloy 48*, a very high relative permeability material, commonly used for these purposes [53], [62]. The foil is made up of *S235* steel, which exhibits ferromagnetic behavior and relatively high permeability. The soft magnetic materials have been chosen to assure a working voltage swing greater than 1 V. In addition, the choice takes into account the fact that the LVDT materials themselves may worsen the interference effect. The model presents insulator layers and washers between and over the primary and secondary coils that are treated as nonmagnetic regions in the simulations. The structure is enclosed in a cylindrical case with two end-caps, made up of *S235* steel (Fig. 7.2). The F.E.M. simulator FLUX© from *CEDRAT Technologies* has been used, as it is particularly suited for solving electromagnetic problems involving movable parts, such as sensors, motors, and actuators [53]. In addition, it allows a deep investigation of flux distributions, end effects, nonlinearity, and non uniformity of field strength along the different magnetic elements [54], [55]. For ferromagnetic

Indicator	Description
Mesh Type	$2D$ Triangular Nonuniform
Mesh Order	2nd
Number of Mesh Elements	10628
Number of Poor Quality Elements	3.5 %
Min - Max Mesh Element Size	0.05 mm (Foil) - 20 mm (Air ∞)
Average Mesh Density	3 elements/thickness

Table 7.1: F.E.M. mesh properties for the shield design.

materials, FLUX works with nonlinear $B-H$ curves, but it does not consider hysteresis effects [53]. The model has been prepared in $2D$ environment, because the LVDT sensor has cylindrical symmetry, thus only half of the longitudinal section of the sensor has been modeled (Fig. 7.1). The model mesh features are summarized in Tab. 7.1. The choice of a nonuniform 2nd order mesh assures a faster elaboration and a precise solution. The primary coil is fed by a voltage generator providing a 3.5 V sine waveform at 2000 Hz. The amplitude of the first harmonics of the induced voltages on the two secondary coils has been evaluated using a fast Fourier transform (FFT) algorithm in order to calculate the ratiometric value as a function of the position, ranging from -15 mm to $+15$ mm, corresponding to 60 % of the overall core position range of the sensor.

7.2 DC Polarization

The amplitude of the secondary voltages as a function of the the external field and the core position can be easily derived by (6.19) as:

$$A_{v_{1,2}}^{f_0}\left(H_{dc}, x\right) \approx 2\pi f_0 H_{ac} S_{sec_{1,2}} \left| \mu_{d_{1,2}}^{eq}\left(H_{dc}, x\right) \right| \tag{7.1}$$

The sensitivity of the amplitude of the secondary voltages to the external

field depends clearly on the local slope of μ_d^{eq} around the generic point H_{dc}^0 as shown by evaluating the difference quotient of (7.1):

$$\frac{\Delta A_{v_{1,2}}^{f_0}}{\Delta H_{dc}^0} \approx S_{sec_{1,2}} 2\pi f_0 H_{ac} \frac{\Delta |\mu_{d_{1,2}}^{eq}|}{\Delta H_{dc}} \left(H_{dc}^0, x\right) \tag{7.2}$$

The field H_{dc}^0 is zero in the nominal operation of the LVDT, thus the influence of external field depends on the slope of the differential permeability of the different materials around the zero. Actually, the H_{dc} field can be equivalently produced applying a DC component in the primary circuit. In this case, analyzing the typical shape of the $B - H$ curve of the used soft magnetic materials [53], it is possible to choose a biasing field characterized by a reduced influence of the ΔH_{dc} produced by the external field. Because of the demagnetization effect on the core of the LVDT, a relationship between the applied field produced by the primary current and the resulting fields H_{ac} and H_{dc} can be established only by means of simulations. Eventually, such biasing will affect the linearity of the sensor [63].

7.3 Shield Design

Normally, commercial LVDTs present a cylindrical shield integrated in the sensor magnetic circuit. An innovative aspect of the proposed solution consists in separating the magnetic circuit of the coaxial cylindrical shield from the sensor. In this way, the design of the shield can be optimized for the rejection without concerns about any magnetic sensor constraint. Dimensions, materials, and distances between the different shielding layers can be adjusted to achieve a given shielding efficiency, depending on the maximum acceptable variation of position measurement. Preliminary simulations have shown that a $1-mT$ transversal flux density produces a nonuniform distribu-

tion along the core, ranging from 3 μT to 19 μT, whereas a longitudinal flux density of 1 mT produces a nonuniform distribution along the core, ranging from 8 mT to 130 mT. Thus, the effect of a transversal field is negligible with respect to the longitudinal one. A set of simulations has been carried out to evaluate the effect of an interfering longitudinal magnetic field, ranging from 0 A/m to 800 A/m, on the measured position. It showed that the maximum variation of the measured position is about 1 mm, as well as that the magnetic field has to be reduced to about 35 A/m in order to have a variation not greater than 20 μm. Therefore, the shield has to show an attenuation factor of about 23. In a scenario with a longitudinal interfering field of 800 A/m, the cylindrical shield is interested by a field with both longitudinal and transversal components not uniformly distributed along its length (Fig. 7.1).
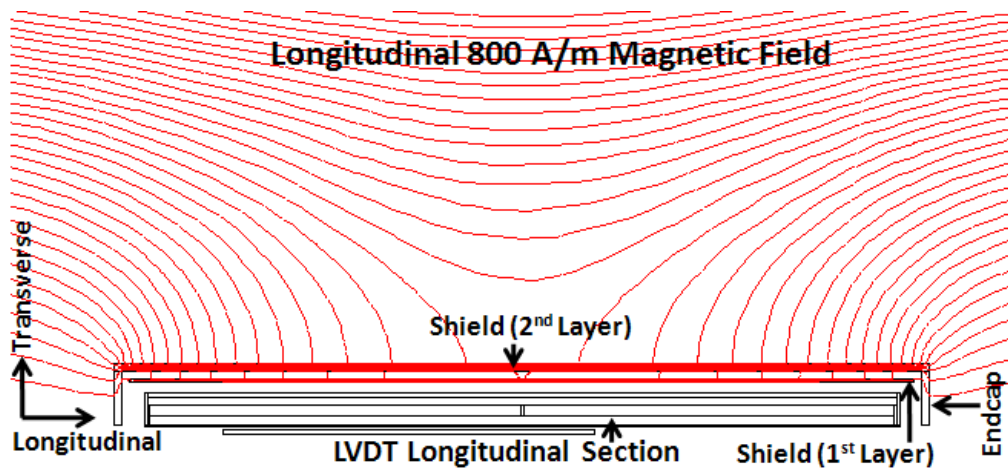
Figure 7.1: Flux density distribution of an external longitudinal magnetic field impinging on the LVDT shield. Half of the LVDT longitudinal section is displayed.

Since such a case cannot be handled by means of an analytical approach [64], a simulation plan with *F.E.M.* software turned out to be necessary in order to design the shield, having as a basis the following guidelines:

1. use of high magnetic permeability materials to reduce the interfering fields;

2. consideration of a multilayer shield to prevent the saturation of the inner layer;

3. optimization of the air gap between the layers and their thicknesses not to oversize the shield with respect to the sensor dimensions.

Accordingly, a single-layer shield with a high-permeability material, such as *Mumetal* [65], has been discarded since a decrease of about 50 % of the permeability (from 120000 to 60000) has been observed, meaning a significant saturation. For this reason, the shield has been endowed with an external layer as shown in Fig. 7.2. Half of the longitudinal section displayed in Fig. 7.2 has been used for *2D* simulations. The distance between the two layers is 1 *mm*, and it assures that the *Mumetal* layer does not saturate and provides an appropriate shunting for the flux. The external layer is a *low-carbon iron* cylindrical foil [65] endowed with two end-caps that, in particular, assure a very effective binding of the longitudinal flux lines, avoiding a direct impact on the sensor's magnetic circuit, as shown in Fig. 7.1. For this reason, additional *Mumetal* end-caps turned out to be useless. A simulation scan showed that 1 *mm* of *low-carbon iron* and 0.4 *mm* of *Mumetal* assure both the saturation prevention and the required shield efficiency. In fact, with an external magnetic field of about 30 A/m, the variation of the measured position of the LVDT is contained within 20 μm, which has been considered as the design goal.
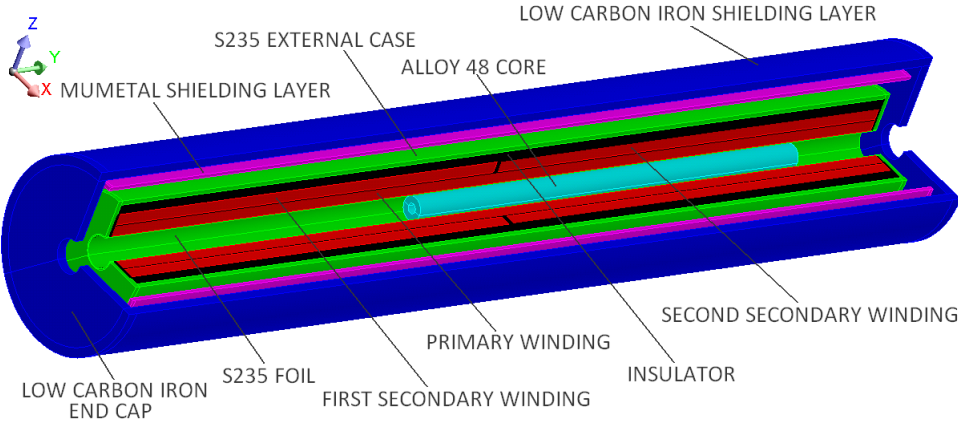
Figure 7.2: LVDT model prototype and shield case.

Part III: Simulation Results

Chapter 8

Estimation of the secondary voltage amplitude

Numerical simulations have been performed in MATLAB$^{\text{©}}$ in order to validate and graphically highlight the properties of the statistical distribution of the amplitude estimator in the optimal case of coherent sampling under AWGN hypotheses.

8.1 White Noise Generation

White Gaussian noise realizations were produced in two steps:

- generation of a pseudo Gaussian noise vector $\mathbf{n}$ by means of the MATLAB$^{\text{©}}$ normal random number generator $randn(.)$

- whitening of vector $\mathbf{n}$ in order to produce zero-mean white Gaussian noise vector $\mathbf{w}$

The following equations clarify the process of producing a WGN realization $\mathbf{w}$ from the Gaussian noise realization $\mathbf{n}$. The covariance matrix $\mathbf{C_{nn}}$ of vector $\mathbf{n}$, being nonnegative-definite and symmetric can, indeed, be diagonalized as shown in (8.2).

$$E\left[\mathbf{n}\right] = \mu_n \tag{8.1}$$

$$\mathbf{C_{nn}} = E\left[\left(\mathbf{n} - \mu_n\right)\left(\mathbf{n} - \mu_n\right)^T\right] = \mathbf{\Phi\Lambda\Phi}^T \tag{8.2}$$

Matrix $\mathbf{\Phi}$ is orthogonal (i.e. $\mathbf{\Phi}^{-1} = \mathbf{\Phi}^T$) and matrix $\mathbf{\Lambda}$ is diagonal. Once the matrices $\mathbf{\Phi}$ and $\mathbf{\Lambda}$ have been calculated the noise realization $\mathbf{n}$ can be "whitened" in order to produce a WGN realization of given power $\sigma_{\mathbf{w}}^2$ by means of (8.3).

$$\mathbf{w} = \sigma_{\mathbf{w}}\mathbf{\Lambda}^{-\frac{1}{2}}\mathbf{\Phi}^T\left(\mathbf{n} - \mu_n\right) \tag{8.3}$$

Indeed the covariance matrix of $\mathbf{w}$ has the typical expression $\sigma_{\mathbf{w}}^2\mathbf{I}$ of a discrete white stochastic process of power $\sigma_{\mathbf{w}}^2$ and its PDF is, approximately, Gaussian since the $\mathbf{w}$ has been generated from the, approximately, Gaussian process $\mathbf{n}$ by means of the linear transformation (8.3).

Considering that $\mathbf{\Lambda} = \mathbf{\Phi}^T\mathbf{C_{nn}}\mathbf{\Phi}$ and that $\mu_{\mathbf{w}} = E\left[\mathbf{w}\right] = 0$ equation (8.4) formalizes what has been just discussed.

$$
\begin{aligned}
\mathbf{C_{ww}} &= E\left[\mathbf{w}\mathbf{w}^T\right] = E\left[\sigma_{\mathbf{w}}\mathbf{\Lambda}^{-\frac{1}{2}}\mathbf{\Phi}^T\left(\mathbf{n} - \mu_n\right)\left(\mathbf{n} - \mu_n\right)^T\right]\mathbf{\Phi}\mathbf{\Lambda}^{-\frac{1}{2}}\sigma_{\mathbf{w}}\right] \\
&= \sigma_{\mathbf{w}}\mathbf{\Lambda}^{-\frac{1}{2}}\mathbf{\Phi}^T\mathbf{C_{nn}}\mathbf{\Phi}\mathbf{\Lambda}^{-\frac{1}{2}}\sigma_{\mathbf{w}} = \sigma_{\mathbf{w}}\mathbf{\Lambda}^{-\frac{1}{2}}\mathbf{\Phi}^T\mathbf{\Phi}\mathbf{\Lambda}\mathbf{\Phi}^T\mathbf{\Phi}\mathbf{\Lambda}^{-\frac{1}{2}}\sigma_{\mathbf{w}} \\
&= \sigma_{\mathbf{w}}^2\mathbf{I}
\end{aligned}
\tag{8.4}
$$

8.2 Data Analysis

In Fig, 8.1 the Rice and the Gaussian distributions are compared for an intermediate value of signal-to-noise ratio obtained with $N = 5000$ realizations

of white Gaussian noise generated by means of (8.3). It can be observed that the SNR is large enough, thus a Gaussian distribution fits pretty well even though the Rice fits better as shown by the log-likelihood indicator.

In the implementation of the the whitening process, a covariance matrix strictly (within numerical precision of MATLAB$^{©}$) equal to $\sigma_{\mathbf{w}}^2\mathbf{I}$ has been obtained, though not strictly zero-mean realizations have been generated, which is not really critical since the coherent sampling only is discussed here. In Fig. 8.1 it is depicted a graphical comparison between the Rice distribution and the Gaussian distribution for an intermediate value of signal-to-noise ratio obtained with $N = 5000$ realizations of white Gaussian noise generated by means of (8.3) from which it can be easily seen that the Rice distribution is the best fit as highlighted by the log-likelihood indicator. In particular, it can be seen by (8.5) and (8.6) that, even for the considered value of the SNR of circa -23.17 dB, the relative errors with respect to the asymptotic values of the standard deviation and of the mean, introduced in (5.52) and (5.53), are pretty small.

$$\frac{\sigma_{\widehat{A}} - \sqrt{\frac{2}{N}}\sigma_{\mathbf{w}}}{\sqrt{\frac{2}{N}}\sigma_{\mathbf{w}}} = -6.13 \times 10^{-3} \tag{8.5}$$

$$\frac{\mu_{\widehat{A}} - \left(\widetilde{A} + \frac{1}{N}\frac{\sigma_{\mathbf{w}}^2}{\widetilde{A}}\right)}{\left(\widetilde{A} + \frac{1}{N}\frac{\sigma_{\mathbf{w}}^2}{\widetilde{A}}\right)} = 3.75 \times 10^{-3} \tag{8.6}$$

Fixed N for smaller and smaller values of the input SNR the distribution would approach a Rayleigh whereas for larger and larger ones it would approach better and better a Gaussian even though it must be noted that for a Gaussian distribution the probability of a negative value is strictly non zero, whereas, by definition, an amplitude cannot be negative.
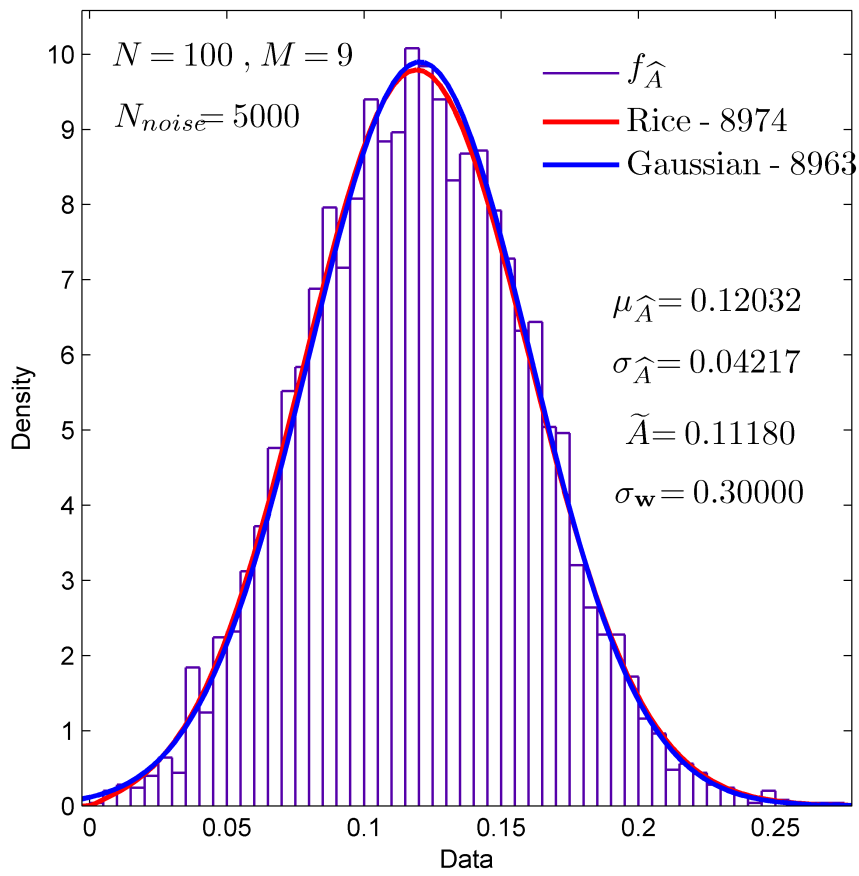
Figure 8.1: Distribution of the amplitude estimator $\widehat{A}$ generated by 5000 realizations of white noise $\mathbf{w}$ in a case, $\sigma_{\mathbf{w}} = 0.3$ far from the asymptotic behavior.

Chapter 9

Interference Simplified Analytical Model Validation

The analytical simplified model, comprising only current supply of the primary (6.3), was validated through a series of simulations mainly aimed at supporting the introduction of the secondary equivalent permeability defined in 6.3.2.

9.1   Coil Equivalent Permeability Validation

Magnetostatic simulations were run with FLUX$^©$ in order to validate the analytical expression of the *averaged coil equivalent permeabilities* of (6.9). The mutual inductances between the primary and the two secondary coils were evaluated, with N_{pri} primary turns and N_{sec} secondary turns, by means of FLUX^{TM} and by means of the following equations:

$$M_{sec_1}(x) = \mu_{sec_1}(x)\frac{N_{sec}N_{pri}S_{sec}}{l_{pri}}$$
$$M_{sec_2}(x) = \mu_{sec_2}(x)\frac{N_{sec}N_{pri}S_{sec}}{l_{pri}} \tag{9.1}$$

Transient analysis, with sinusoidal primary current, was conducted as

well in order to double check the results of the magnetostatic simulations without significantly different results.

The comparisons between the simulations results, and the analytical model calculations are reported in Fig. 9.1 with the relative error that is below 4 %. As expected the analytic curves are exactly linear whereas the F.E.M. curves show a non negligible nonlinearity mainly due to the non uniform distribution of the fields in the core (owing to complex demagnetization effects). One of the geometrical elements playing a major role in that nonlinearity is the airgap s in Fig. 6.7. The description of such effects fairly outgoes the scope of this work [48]. Equations similar to (9.1) and (6.10) were written for the primary autoinductance and voltage amplitude respectively. They give a relative error not greater than 2.4 % with respect to the F.E.M. simulation results. The primary autoinductance is not a function of the core position according to the analytical model ($L_{pri} \approx 19.857\ [mH]$ uniformly). A weak dependence in the simulations results ($L_{pri} \approx 19.545\ [mH]$ when the core is in position 0 and $L_{pri} \approx 19.401\ [mH]$ at the extremes) due to the airgap was found as well. The overall agreement between the simulation results and the analytical calculations is considered well-suited for the scope of this work.
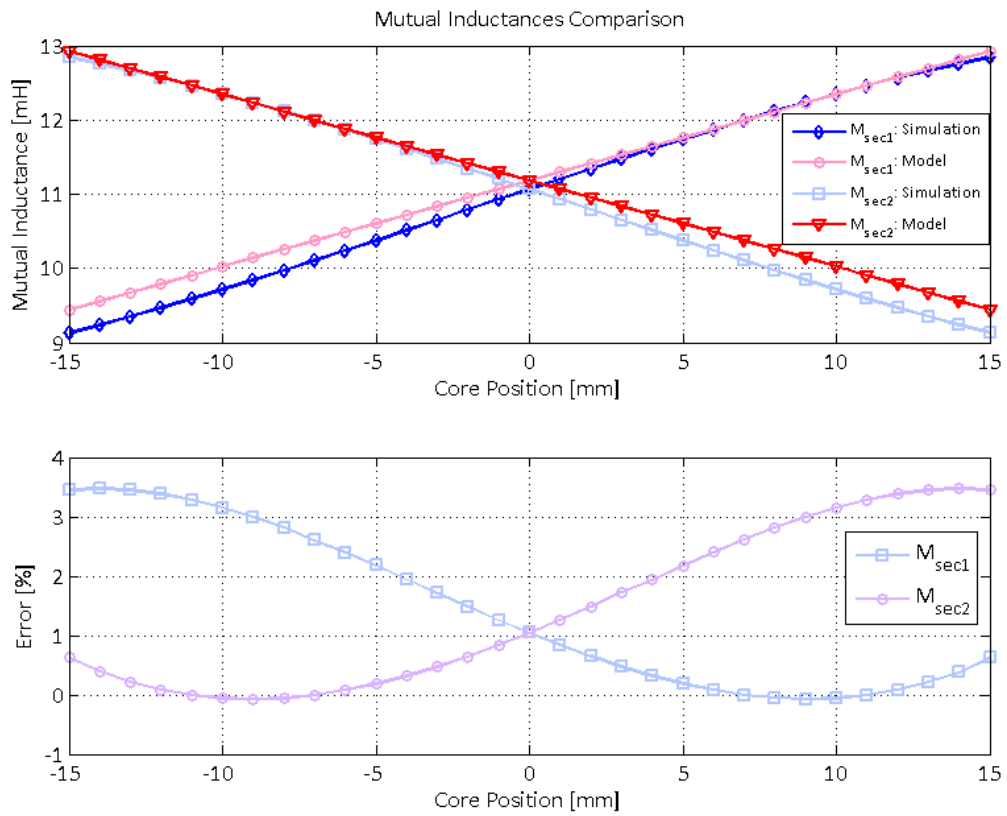
Figure 9.1: Comparison between the mutual inductances evaluated by means of analytic formulas and F.E.M. simulations.

Chapter 10

F.E.M. Model Characterization

In this Chapter, the simulation results for voltage and current supply, in presence and in absence of the interfering magnetic field, are shown. Although the two modes of voltage and current supplies are both used in commercial LVDTs, the need for studying the phenomenon with both of them arises from the fact that when the supply signal is a purely sinusoidal current, the overall magnetic field is sinusoidal. Conversely, with voltage supply, the overall magnetic field is distorted owing to the nonlinearity of the magnetic media. Hence, the influence of the external magnetic field can, in principle, play different roles in the two cases. For each of them, the LVDT characteristic curve, showing the first harmonics of the secondary voltages with respect to the reference position, is highlighted. In addition, the ratiometric is computed as follows:

$$r = \frac{A_1 - A_2}{A_1 + A_2} \tag{10.1}$$

where A_1 and A_2 are the amplitudes of the first harmonics of the first and second secondary, respectively. A non-linearity error has been computed as:

$$NL = 100 \, \frac{\max(p^{'} - p^*)}{CPR} \tag{10.2}$$

where p^* is the core reference position, $p^{'}$ is the interpolated one, CPR is the core position range. Even if normally the core position ranges goes from -20 to 20 mm, some interesting results hold for smaller ranges too. In case of interference, the external magnetic field yields a variation on the measured position. Hence, a variation has been computed, at each core position, as difference between the positions *read* in presence and in absence of the interference. In both the cases, the position is achieved through the ratiometric reading technique, by means of a calibration curve in standard working conditions. Actually, the position measurement variation allows the effect of the external magnetic field to be analyzed on a certain position.

10.1   Voltage Supply Simulation

The sensor was supplied by a 3.5 V-peak sinusoidal voltage at 2000 Hz. The characteristic curve in this case is displayed in Fig. 10.1 for core positions ranging from -20 to $+20$ mm.

The curve is symmetric with respect to the null position, owing to the complete symmetry of the device. The simulations show that the secondary transformation ratio of the sensor goes from 0.54 (minimum core coupling) to 1.66 (maximum core coupling). The ratiometric is assessed as a function of the position in Fig. 10.2. The ratiometric is a monotonic function ranging from about -0.5 to about 0.5 over the full core position range. Once again, the perfect odd symmetry of the curve reflects the perfect geometrical symmetry and reciprocity of the simulated device.

In simulation, the nonlinearity of the device resulted 0.7 % in the range $[-20, 20]$ mm. The linearity becomes more acceptable when the core position range is reduced: nonlinearity is 0.11 % in the range $[-10, +10]$ mm. The
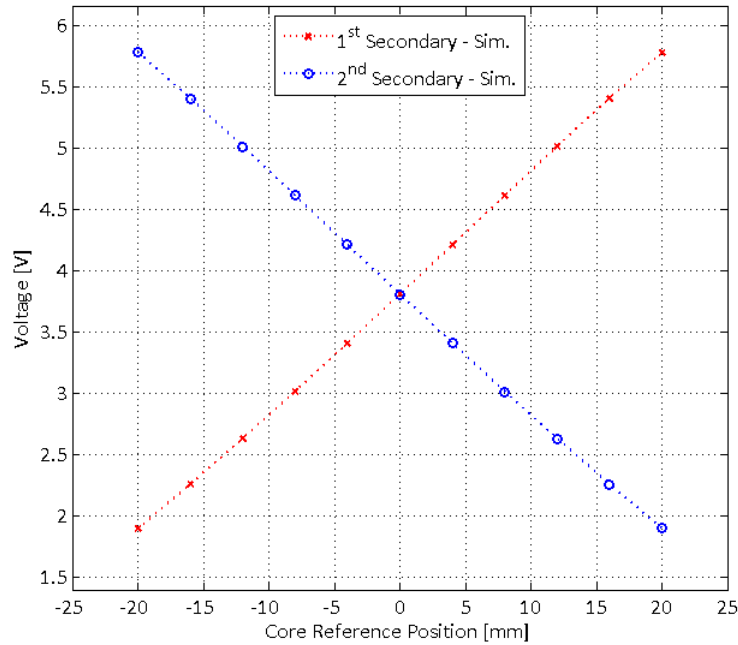
Figure 10.1: Simulation results regarding the LVDT secondary characteristic curve (voltage supply).

results for the longitudinal interference are displayed in Fig. 10.3. The position measurement variation is a monotonic function of the core position exhibiting an odd symmetry (reflecting again the geometrical symmetry of the device). In addition, it is zero in the null position. The farther from the center the core is, the greater the position measurement variation is. In the worst case, at the core position of 20 mm, the variation can reach a value of about 70 μm.
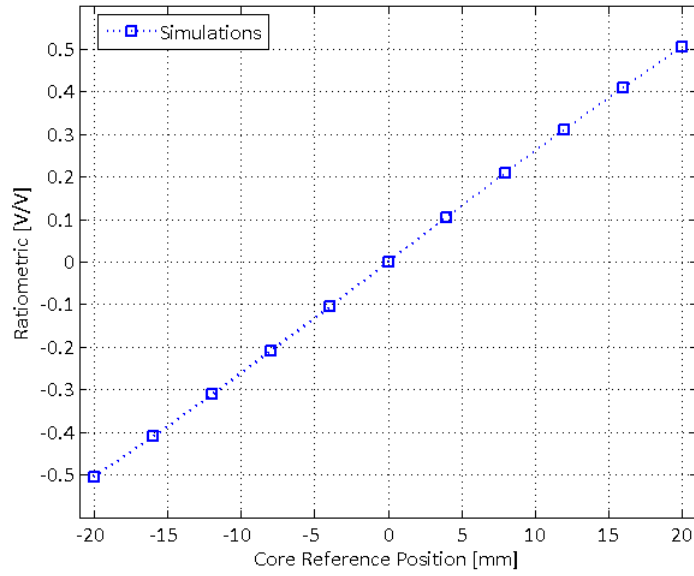
Figure 10.2: Simulation results regarding the ratiometric (voltage supply).
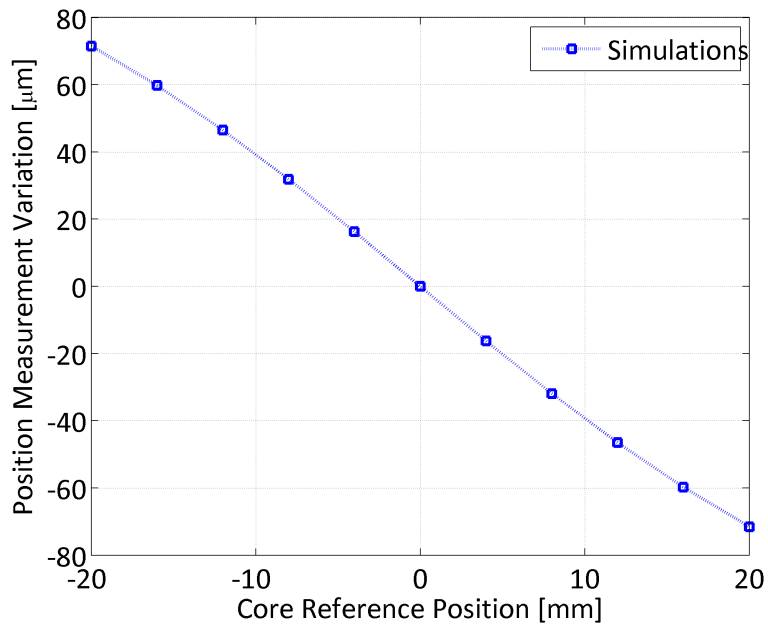
Figure 10.3: Simulation results regarding the position measurement variation (voltage supply).

10.2 Current Supply Simulation

The sensor was fed with a current sine wave at 2 kHz whose amplitude. The amplitude of 24.0 mA was chosen in order to have the amplitude of the first harmonic of the primary voltage of about 3.5 V when the core is in null position. In this way, the simulation results can directly be compared with the ones obtained with voltage supply.
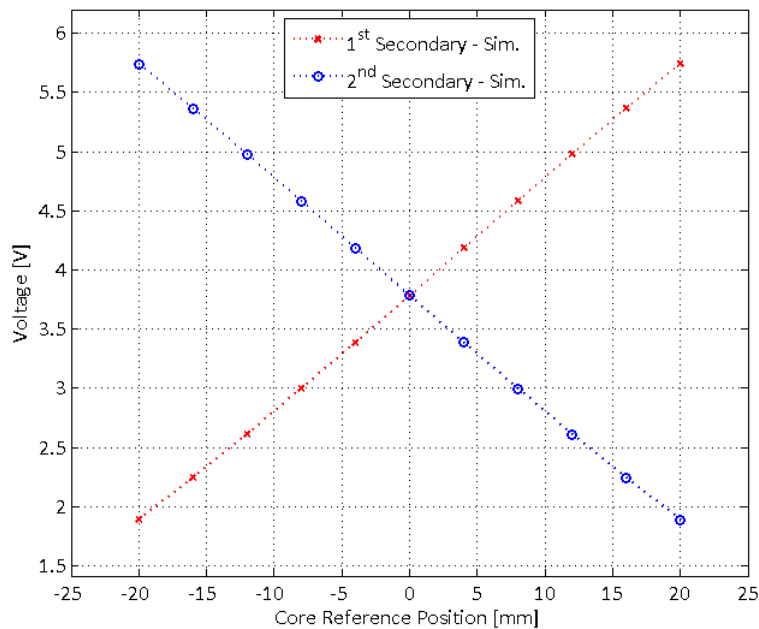
Figure 10.4: Simulation results regarding the LVDT secondary characteristic curve (current supply).

The characteristic curve in the current supply case is displayed in Fig. 10.4 for core positions from -20 to $+20$ mm. Again, a dual behavior of the two curves in terms of trend and the symmetry around the null position can be noticed. In this case, the secondary transformation ratio of the sensor ranges from 0.54 (minimum core coupling) to 1.66 (maximum core coupling).

In Fig. 10.5, the ratiometric curve with respect to the core position in current supply is shown. It is very similar to the corresponding curve in voltage supply: the trend is monotonic (due to the LVDT working principle) and the ratiometric ranges from about -0.5 to $+0.5$, with a zero value in null position. Thus, the curve is once again symmetric with respect to the null position. In addition, the nonlinearity error (0.7 % on the full range, 0.12 % in the range going from -10 to $+10$ mm) is roughly the same observed with voltage supply.
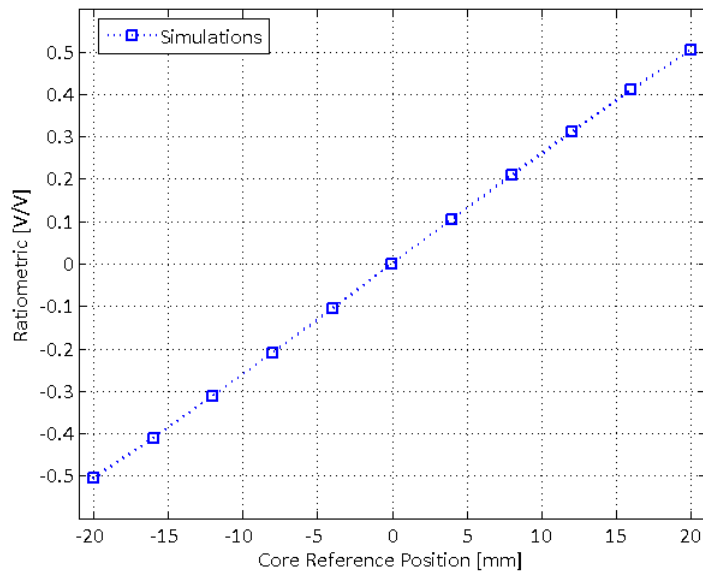
Figure 10.5: Simulation results regarding the ratiometric (current supply).

In Fig. 10.6, the results regarding the position measurement variation are depicted. The shape and the magnitude recall the corresponding behavior in voltage supply. Here, the position measurement variation ranges from $+72$ to -72 μm, with a zero value in null position and higher values for positions farther from the center.
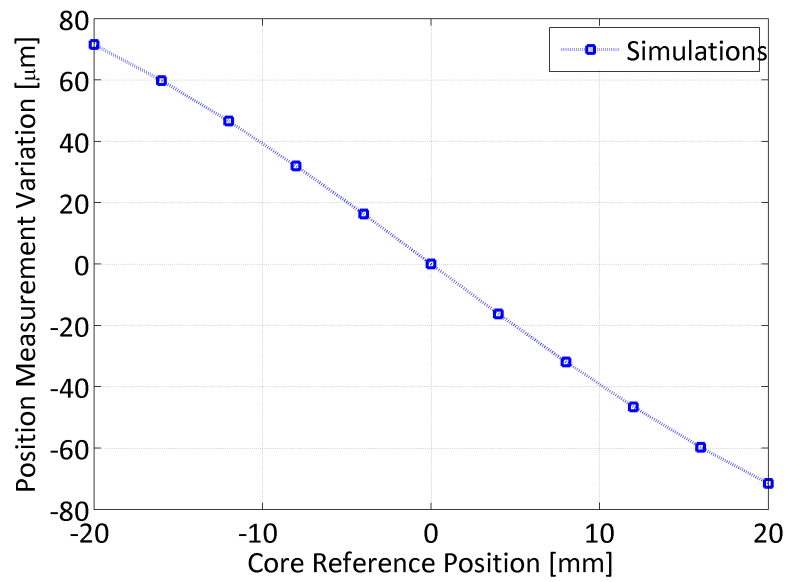
Figure 10.6: Simulations results regarding the position measurement variation (current supply).

Chapter 11

Validation of Design Guidelines for DC Polarization and Magnetic Shielding

The following simulation results take into account only the dominating interference of the longitudinal magnetic field. In Fig. 11.1, the characteristic of the sensor, representing the calibration curve, and the effects of an 800 A/m external magnetic field, are shown.

The position value, in presence of external field, was evaluated on the basis of the corresponding ratiometric value by means of a linear interpolation of the calibration curve. The position measurement variation increases according to the nominal position, achieving a maximum value of about 1 mm (Fig. 11.2). DC magnetic bias can be used to reduce the effect when a shield is not sufficient or cannot be fit for mechanical reasons. At this aim, a DC voltage of 10 V (corresponding to a DC current of 160 mA) was added to the primary input. Once the calibration curve of the sensor is evaluated in presence of the DC effect, the maximum position measurement variation due to an external interference of 800 A/m results to be reduced by a factor 2 (Fig. 11.2). The inversion of the variation sign is due to the DC polarization
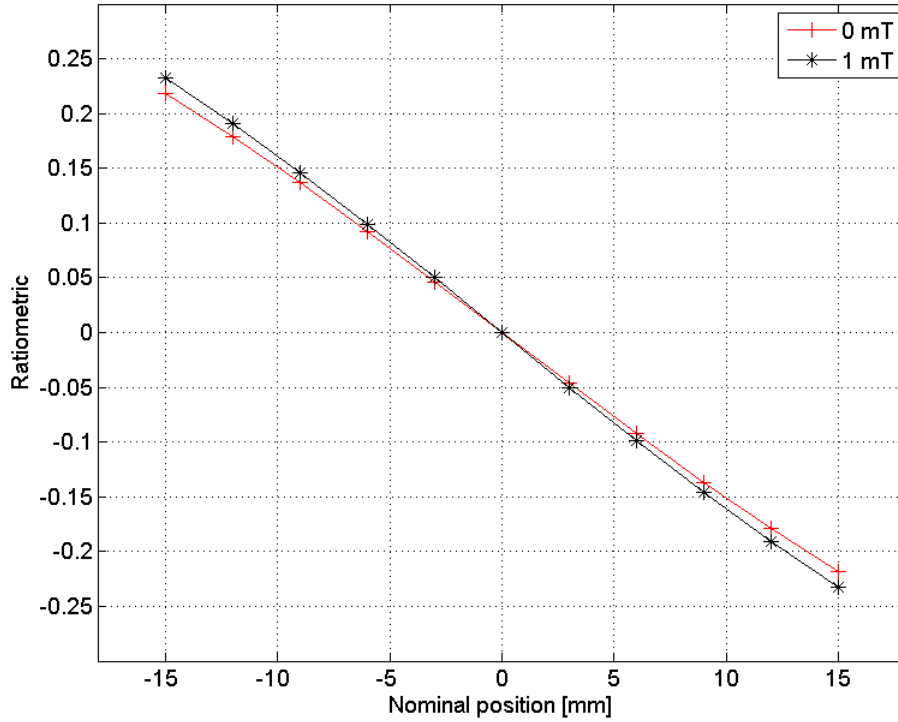
Figure 11.1: Sensor characteristic with and without a longitudinal magnetic field of 800 A/m.

affecting the characteristic curve of the sensor. However, as a main solution strategy, the external magnetic interference can be reduced by means of the shield case described in Chapter 7. The shield reduces the position measurement variation to about 12 μm without deeply affecting the sensor linearity (Fig. 11.3).

Finally, both the shield and the 10-V DC polarization were applied to the LVDT (Fig. 11.3). The benefits of both the solutions are kept since the position measurement variation is still reduced by a factor 2 (Fig. 11.3).
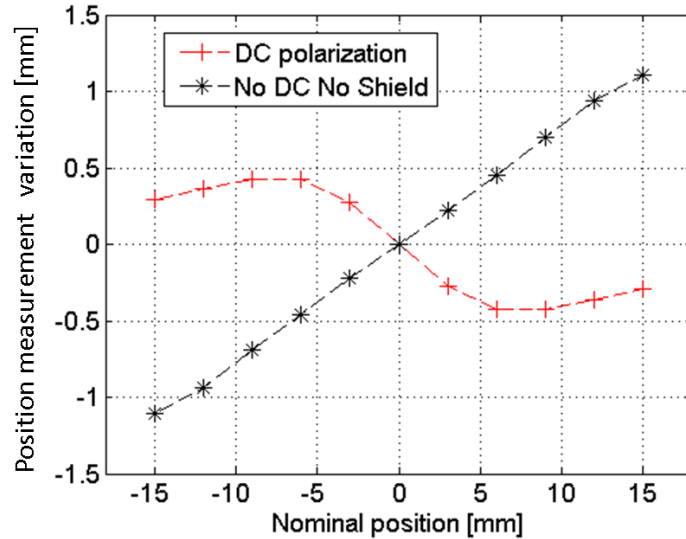
Figure 11.2: Comparison between the position measurement variation of the LVDT model with ($*$) and without ($+$) DC polarization.
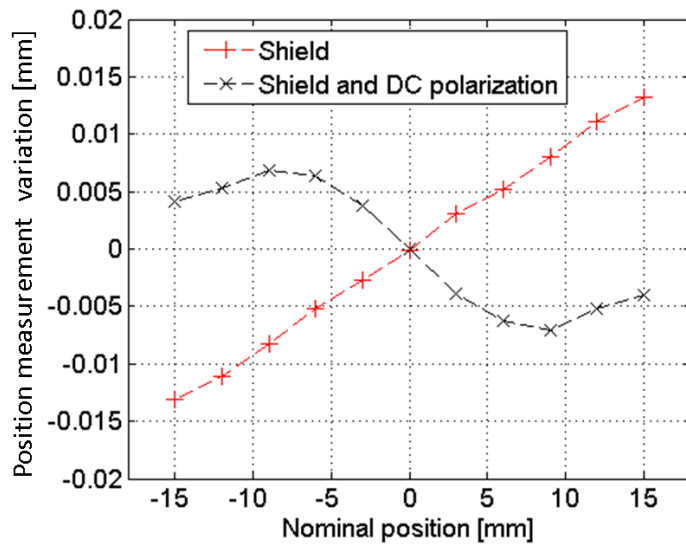
Figure 11.3: Position measurement variation with the shield ($+$) and its combined effect with DC polarization ($\times$).

Part IV: Experimental Results

Chapter 12

Experimental Characterization of the secondary voltage amplitude estimation

12.1 Software Performance

In Fig. 12.1, the statistics for the parallel readout of 3 collimators' LVDTs running on the same CPU are shown. Each task runs in parallel and is completed in approximately 1 ms. No significant differences exist between them and the time jitter is negligible. The statistics are evaluated on 5000 readings, each one coming from 2000 samples per channel.

12.2 Single LVDT Characterization

An experimental campaign was carried out to characterize the single LVDT reading performance. The nominal configuration is with $N = 2000$ samples and no motor driver running during the test. The nominal gain of 100 $mm/ratiometric$ is assumed for all the LVDTs. In Fig. 12.2, the typical amplitude estimate, in the lab setup, for the two secondaries of a single LVDT connected to the PRS by a short cable, is depicted (on the left, histogram
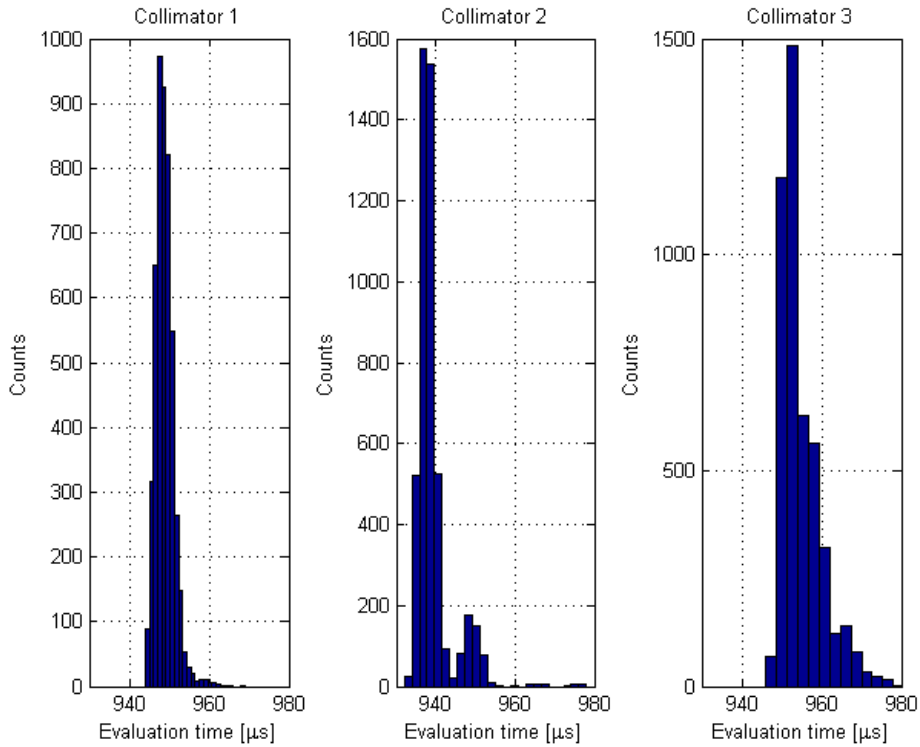
Figure 12.1: Positioning Readout and Survey task execution time.

of the first secondary of *LVDT A*; on the right, the second secondary). The *SNR* measured on the signals is close to 30 *dB*. The standard deviation evaluated on 5000 readings is about 10 *ppm* of the amplitude. This is in reasonable agreement with the approximated formulas (5.53).

Noise generated by the stepping motor drivers power electronics was taken into account by adding a square wave noise has been added on one secondary of the LVDT through the experimental setup of Fig. 12.3. The noise was added at 9 *kHz* and 18 *kHz*, since the *LHC* motor drivers work at a chopping frequency of 18 *kHz* and sub-harmonics may be present due to the *PWM* control. The main sub-harmonic involved is the half order [66]. The square waves were generated with a *SRS DS-360* frequency generator. A Single
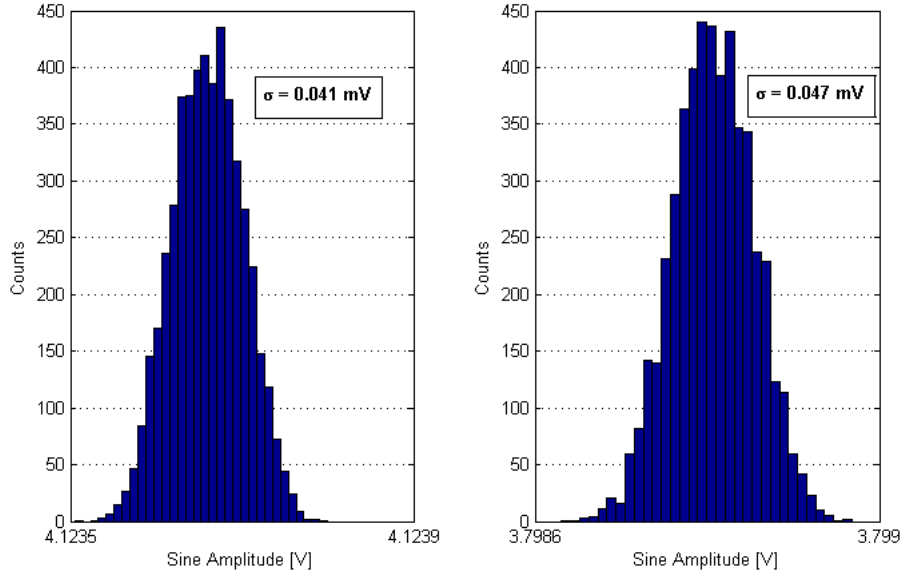
Figure 12.2: Typical performance of the channel amplitude estimate. $f_0 = 2125\ Hz$.

Ended-Differential mixer was built to add the *noise* to the useful channel, because the output of the *DS-360* is single-ended, while the LVDT signals are differential.

The ratio between the standard deviation of the position reading at various SNR level and the standard deviation without noise was evaluated. The reference standard deviation σ_0^{mm} is measured with the mixer connected and the generator switched off. The experimental results are summarized in Fig. 12.4. The standard deviations σ^{mm} of the position were normalized to the nominal value σ_0^{mm} with no square wave disturbance applied in order to highlight the effect of the disturbance. Each plotted value is the average of two different measurements, with σ^{mm} evaluated on $N = 5000$ readings. The immunity is very good for all the reasonably expected values of the SNR.
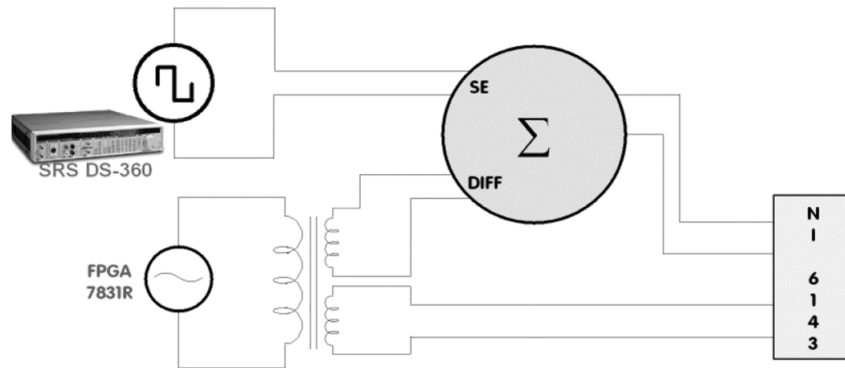
Figure 12.3: Measurement setup for motor driver noise immunity test.
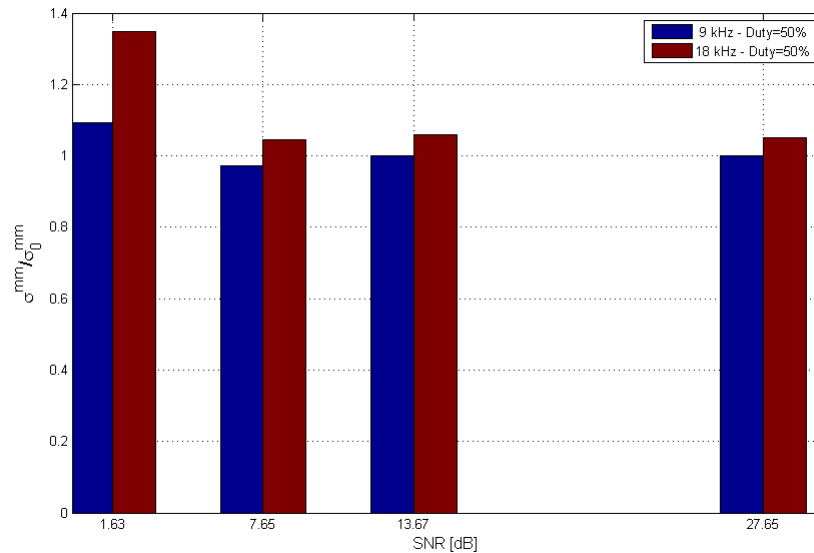
Figure 12.4: Effects of square wave disturbances.

12.3 Multiple LVDTs Characterization

Finally, the performance of the overall system was measured in the nominal conditions. A multi-wire 500-m long cable was used to connect the 21 LVDTs of 3 collimators to the *PRS*. In Fig. 12.5, the amplitude spectrum of a LVDT secondary channel, measured with an *Agilent E7405 EMC* analyzer, is shown. Such as expected, all the other LVDTs' frequencies were detected.

The amplitude of the tones is 60 dB below the main, however the effect of
these spurious tones is negligible because the frequencies were suitably chosen
to be orthogonal.

In Fig. 12.6, statistics for some LVDTs connected both with short and
500-m long cables are reported. It can be proved that the standard deviation
of the reading is a function of the position; anyway the difference among the
values of the standard deviations shown in Fig. 12.6 can be also explained
by the different excitation frequencies and by the different behavior of the
front-end channels. Nevertheless, with the laboratory setup the standard
deviations of the readings are all below 1 μm .
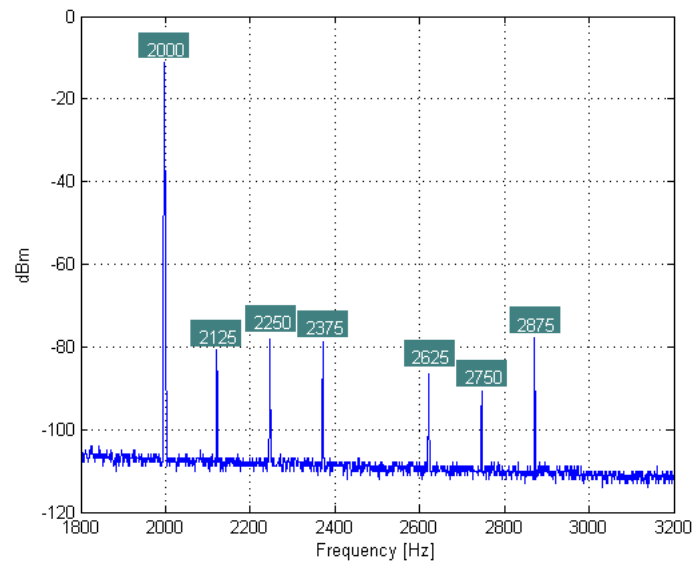
Figure 12.5: Typical spectrum of an LVDT secondary channel.
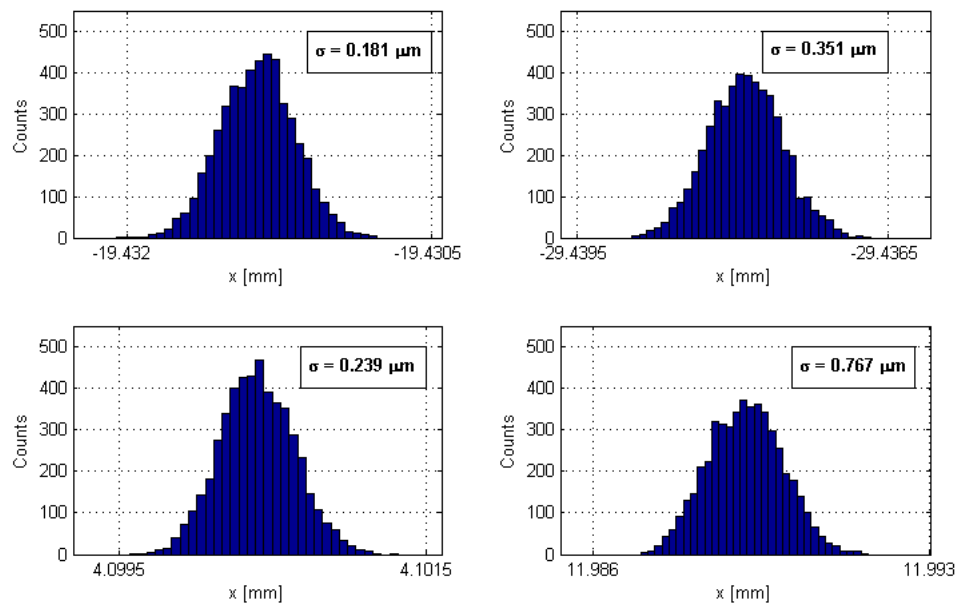
Figure 12.6: Position repeatability with the laboratory setup: standard deviations of two LVDTs on 5000 readings with 500-m long (top) and short cable (bottom).

Chapter 13

Experimental Characterization of the LVDT External Magnetic Field Interference

In Fig. 13.1, the test bench for the experimental characterization of LVDT external magnetic field interference is depicted. The resistive magnet *SIGMAPHI F12407* and the solenoid, used as transversal and longitudinal magnetic interference sources, respectively, are driven by the *KEPKO BOP 50-8M* amplifier. The control voltage is generated by means of an analog output of the data acquisition board *NI-PCI 6289*. The primary coil is connected to the voltage generator *Stanford DS 360* or to the current generator *Keithley 6221*, according to whether the sensor is driven in the voltage or the current mode. The primary and both secondary coils are acquired by means of the data acquisition board *NI-PCI 6123*. A step motor is used to move the LVDT core, and the absolute reference position is measured by means of the photoelectric linear encoder *Heidenhain LIP 401R*, with an uncertainty of $\pm 0.5 \ \mu m$. The test bench is remotely controlled by *LabView*™program.

The external field, which was generated by the solenoid or by the resistive magnet, has been measured by means of a Hall plate *Senis GmbH 3MH3 C—*
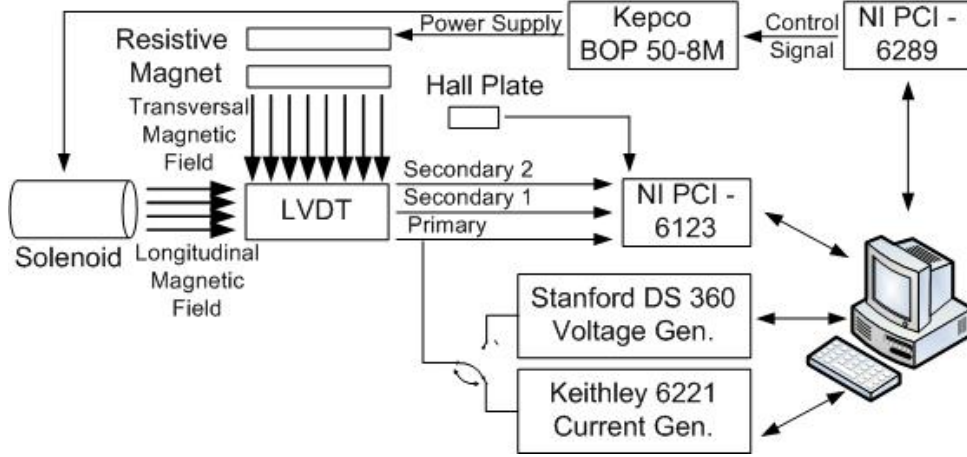
Figure 13.1: LVDT test bench schematics.

H3A to find out the transfer function $I - H$ to be used during the LVDT tests. The solenoid is a 33 *cm*-long plexiglas tube with a diameter of 3 *cm*, with wound 160 turns of a 1 *mm*-diameter wire. The magnetic field H was measured in air as a function of the input current I, in the range -4 to 4 *A*, at different positions along the tube length. The $I - H$ curve with the uncertainty bar and the linear fit of the data are displayed in Fig. 13.2 (top) and 13.2 (bottom), for the solenoid and the resistive magnet, respectively. Both sources show good uniformity of the field along their length, being the measurements at different positions within the uncertainty bar of $\pm 3\sigma$. The uncertainty, obtained by means of 50 repeated tests, resulted to be about ± 80 A/m, i.e is 0.1 % and 0.01 % of the maximum H_z and H_x values, respectively.

Two commercial LVDTs were analyzed to prove the capability of the test bench to characterize the behavior of the sensor with and without an external magnetic field.
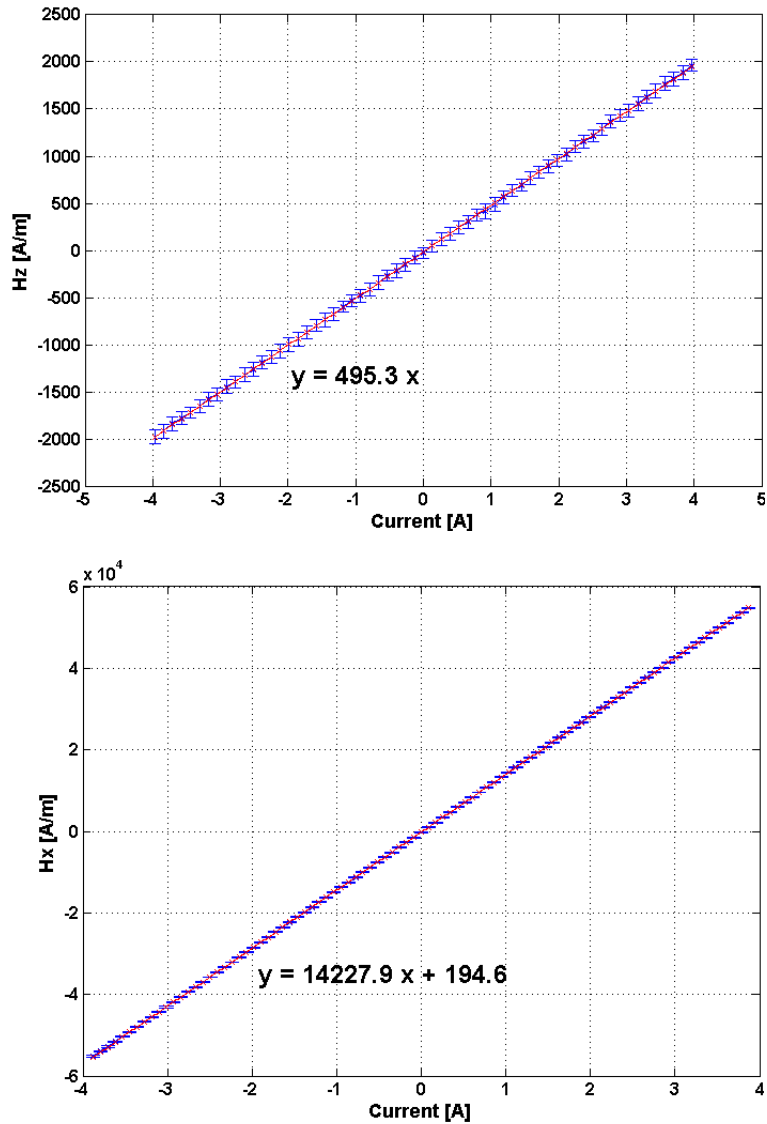
Figure 13.2: Solenoid (top) and resistive magnet (bottom) $I - H$ characteristics.

13.1 LVDT characterization without external field

The *LVDT A* and *LVDT B* were analyzed without external field by measuring their conversion tables T, between the array of position p measured by

LVDT A			
Reading Technique	$\frac{A_1-A_2}{A_1+A_2}$	$\frac{A_1-A_2}{A_{pri}}$	$A_1 - A_2$
Nonlinearity (LVDT and reading system)	0.07 %	0.09 %	0.12 %
$u_{LVDT+read}$ (3σ)	1.0 μm	5.0 μm	4.8 μm
u (3σ)	2.2 μm	5.4 μm	5.2 μm
LVDT B			
Reading Technique	$\frac{A_1-A_2}{A_1+A_2}$	$\frac{A_1-A_2}{A_{pri}}$	$A_1 - A_2$
Nonlinearity (LVDT and reading system)	15.2 %	0.1 %	0.2 %
$u_{LVDT+read}$ (3σ)	6.7 μm	3.0 μm	3.3 μm
u (3σ)	7.0 μm	3.6 μm	3.9 μm

Table 13.1: Summary data of the calibration for *LVDT A* and *LVDT B*

the photoelectric encoder and assumed as reference, and the corresponding ratiometric values r. Both the sensors have a measurement range $[-P,+P]$ of $[-40,40]$ mm. The ratiometric and normalized differential readings were used for *LVDT A* and *LVDT B*, respectively, as suggested by the manufacturers. In Fig. 13.3 (Top) and 13.3 (Bottom), the reading position is depicted as a function of the ratiometric (*LVDT A*) and of the normalized differential value (*LVDT B*). Uncertainty $u_{LVDT+read}$ (type A) was evaluated by means of 50 repeated measurements.

The range was scanned 30 times assessing an uncertainty (type A) u_p of the positioning system equal to be ± 2 μm. This uncertainty is due to the moving system (step motor) and the feedback position sensor. The composition of the uncertainties u_p and $u_{LVDT+read}$ turns out to be the overall uncertainty u of the test bench and of the LVDT under test without magnetic interference. The non linearity and the uncertainty values are reported for the three main reading techniques of the LVDTs (Tab. 13.1).
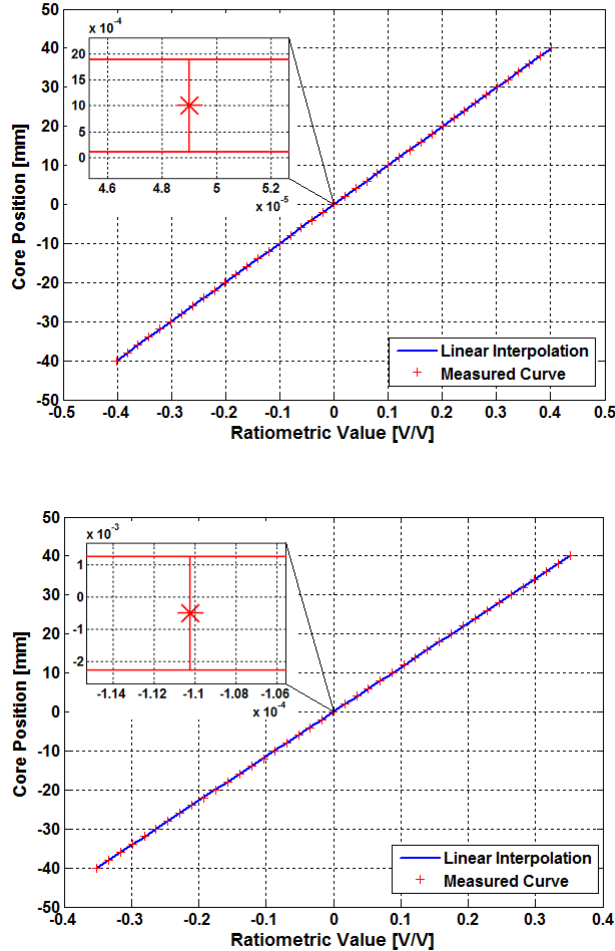
Figure 13.3: Position measurement as a function of the ratiometric value for *LVDT A* (top) and the normalized differential value for *LVDT B* (bottom).

13.1.1 Analysis of the results without the external field

The best performance in terms of both linearity and uncertainty is achieved by using the reading techniques suggested by the manufacturers, i.e., the ratiometric reading for *LVDT A* and the normalized differential reading for *LVDT B*. Generally, the techniques based on the ratiometric readings reduce the effects of the systematic errors of the acquisition system. As a matter of fact, the ratio operation allows reducing the gain errors of the acquisi-

tion system and mitigating temperature effects. The ratiometric technique
also permits reducing the uncertainty of the reading value. By applying the
uncertainty propagation the uncertainty of the ratiometric value u_r results:

$$u_r^2 \leq 2\frac{A_1^2 + A_2^2}{(A_1 + A_2)^4}\left(u_{A_1}^2 + u_{A_2}^2\right) \tag{13.1}$$

where u_{A_1} and u_{A_2} are the uncertainty values (assumed equal) of A_1 and
A_2, respectively, and u_d is the uncertainty of the differential reading. The
factor k determines if uncertainty u_r is minor than u_d. If the voltage signals
are a few Volts, as it is for *LVDT A* and *LVDT B*, k is lower than 2, and u_r
will be lower than u_d.

Similar considerations can be done for the ratiometric reading $\frac{A_1 - A_2}{A_{pri}}$.
However, any conclusion on the best reading technique, basically related to
the LVDT design, its structure, and the coiling of the primary and secondary
circuits can be drawn. As an example, the linearity of *LVDT B* drastically
decreases if the ratiometric reading is used (Tab. 13.1). This is related to
the design itself of the LVDT.

Nonlinearity NL (Tab. 13.1) represents the systematic error of the sensor
and the acquisition system. The systematic errors of the acquisition system
are corrected at each measurement by means of an auto-calibration proce-
dure. The systematic errors on the reading of the voltage amplitudes are
taken into account by the calibration of the LVDT with respect to a refer-
ence position sensor. This is valid provided that the gain and offset of the
board have good stability, although affected by a systematic error. The ef-
fectiveness of the auto-calibration procedure is proven by the fact that the
nonlinearity obtained by the differential reading is only slightly higher than
that obtained by the reading technique suggested by the manufacturers (i.e.,

the ratiometric for $LVDT\ A$ and the normalized differential for $LVDT\ B$),
mitigating the effect of systematic errors by definition since they are based
on ratiometric operation. The nonlinearity of the sensor plays a major role
and is due to the coiling of the primary and secondary circuits and the mis-
alignment of the core.

The uncertainty of type-A $u_{LVDT+read}$, representing the uncertainty of
the sensor itself and the reading system, resulted to be a few micrometers
(Tab. 13.1). This performance is reached due to the high-sampling-rate
and high-resolution analog-to-digital converter (ADC) and by exploiting the
sine-fit algorithm to evaluate the amplitudes of A_{pri}, A_1, and A_2. The sine
fit algorithm allows improving uncertainty on the measurement of the signal
voltage amplitude by reducing the effect of random noise affecting the ADC
samples: if N is the number of samples acquired, the uncertainty due to
the random component is reduced roughly by factor $\sqrt{N/2}$ according to
5.53 for the variance of the amplitude assuming a Rice distribution. Finally,
the results do not depend on the source type of the primary coil because
the same figures were obtained using either a voltage or a current generator.
The overall uncertainty u is dominated by uncertainty $u_{LVDT+read}$ in all cases,
except for $LVDT\ A$ when the ratiometric technique is exploited. In the latter
case, the overall uncertainty is dominated by uncertainty u_p of the positioning
system.

13.2 LVDT characterization with the external magnetic field

The preceding results gave a figure of the overall uncertainty u of the LVDT
and the test bench (Tab. 13.1). This feature is crucial in order to correctly

measure afterward the position variation $p_i - p_i^{\backprime}$ due to an external magnetic field, which depends on the position itself. In fact, the uncertainty of the sensor, the reading system, and the positioning system have to be negligible compared to the measured position variation in order to prove that the latter is effectively due to the external interfering field.

The behavior of the sensor under a magnetic field will be assessed, and all of the three main reading techniques will be exploited including those less effective without any external magnetic interference. In fact, variations of the primary and secondary voltages in the presence of a magnetic field are not known a priori. Therefore, an experimental measurement is required to point out the best reading technique. The position measurement variation $p_i - p_i^{\backprime}$ was measured by applying the external interference $|H|$ up to a maximum intensity of about 800 A/m, i.e., a magnetic field level easily reached in an environment with motors and power cables [12], [67]. The test results are referred to the external longitudinal interference because it causes a measurement variation of about one order of magnitude larger than the horizontal one.

The measurements were carried out for both LVDTs using voltage and current excitations. The three reading techniques, i.e., ratiometric $\frac{A_1 - A_2}{A_1 + A_2}$, differential $A_1 - A_2$, and differential normalized readings to the primary voltage $\frac{A_1 - A_2}{A_{pri}}$, were used in order to evaluate the position on the basis of the coil voltage in order to study how the position measurement variation changes. In particular, the variations at three nominal positions, i.e., ± 15 and 0 mm, due to increasing $H \uparrow$ and decreasing $H \downarrow$ longitudinal magnetic fields, are reported for current and voltage excitations in Figs. 13.4 ($LVDT\ A$) and 13.5 ($LVDT\ B$). In this case, the ratiometric and normalized differential

readings have been used for LVDTs A and B, respectively. The magnetic cycle has been repeated 30 times for each position, and the average value of the position measurement variation with a $\pm 3\sigma$ uncertainty bar is reported (vertical bars of Figs. 13.4 and 13.5).
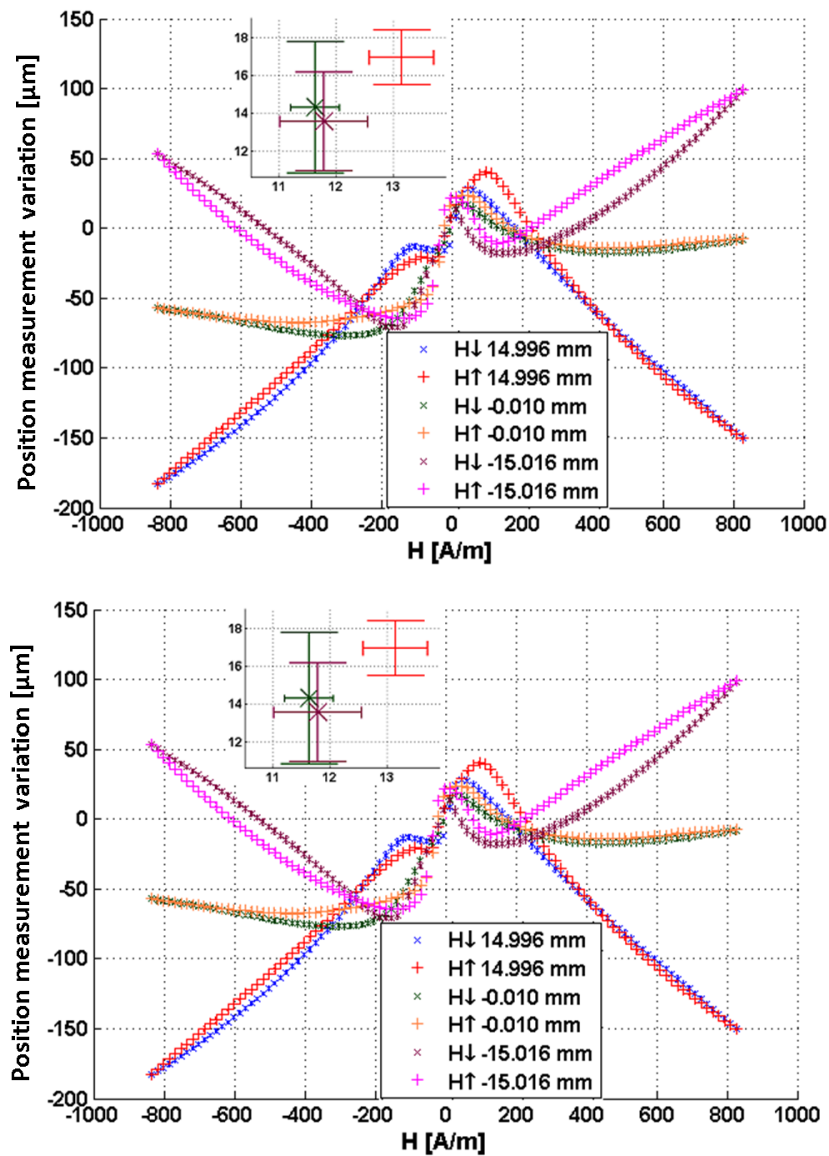
Figure 13.4: Position measurement variation due to a longitudinal interference of 800 A/m for $LVDT$ A in the case of (top) current and (bottom) voltage excitations.

This is mainly due to the difference of the materials of LVDTs. Then, the position measurement variation for *LVDT B* presents a kind of polarization increasing according to the displacement (Fig. 13.5), whereas the variation of *LVDT A* is centered at about the null value. Those different behaviors could be interpreted as a consequence of the difference in the hysteresis cycles exhibited by the LVDTs.
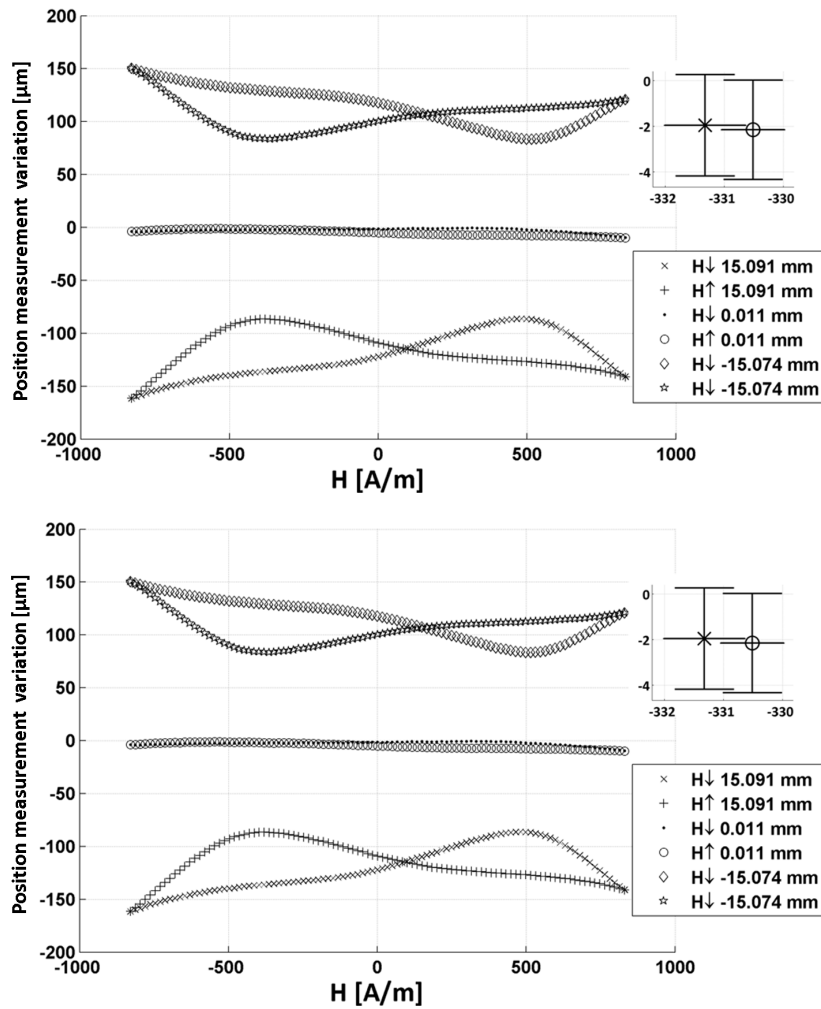
Figure 13.5: Position measurement variation due to a longitudinal interference of 800 *A/m* for *LVDT B* in the case of (top) current and (bottom) voltage excitations.

Despite of this difference, the performance of LVDTs A and B can be comparable if the most suitable supply excitation and reading technique are selected to increase the robustness of the sensor with respect to an external magnetic field. In fact, the maximum measurement variation (at 15 mm and 800 A/m) can be reduced at circa $160 - 180$ μm if the sensors are supplied by a voltage source and read by exploiting the ratiometric and normalized differential techniques for LVDTs A and B, respectively.

The current excitation also gives good results for $LVDT$ B (Tab. 13.2). In more details, as far as $LVDT$ A is concerned, the position measurement variation does not depend on the source excitation (Fig. 13.4) when the ratiometric reading technique is used. The same consideration applies for the normalized differential reading (Fig. 13.6 and Tab. 13.2). The differential reading gives the worst results and is not recommended in the case of a current excitation for which the position measurement variation increases at the order of millimeters. As far as $LVDT$ B is concerned, the position measurement variation does not depend on the source excitation when the normalized differential reading technique or the ratiometric one is applied (Fig. 13.5). However, the technique suggested by the manufacturer gives better results than the latter, contrarily to the case of $LVDT$ A (Fig. 13.7 and Tab. 13.2). The differential technique gives good results in the case of a voltage excitation but gets much worse in the case of a current supply (Tab. 13.2). As a matter of fact, an external field affects the impedance of the primary and, therefore, the primary voltage in the case of a current excitation. That variation is not taken into account in the differential reading, which turns out to be the worst case for a current supply. The variation of the primary voltage is less important in the case of a voltage excitation. Further

$\frac{A_1 - A_2}{A_1 + A_2}$	$\frac{A_1 - A_2}{A_{pri}}$	$A_1 - A_2$
LVDT A : Voltage Excitation		
180 μm	270 μm	310 μm
LVDT A : Current Excitation		
200 μm	290 μm	3500 μm
LVDT B : Voltage Excitation		
410 μm	160 μm	170 μm
LVDT B : Current Excitation		
420 μm	171 μm	555 μm

Table 13.2: Summary data for the maximum position measurement variation at 15 mm in the case of voltage and current excitations for LVDTs A and B

details on the phenomenon model are given in [68].
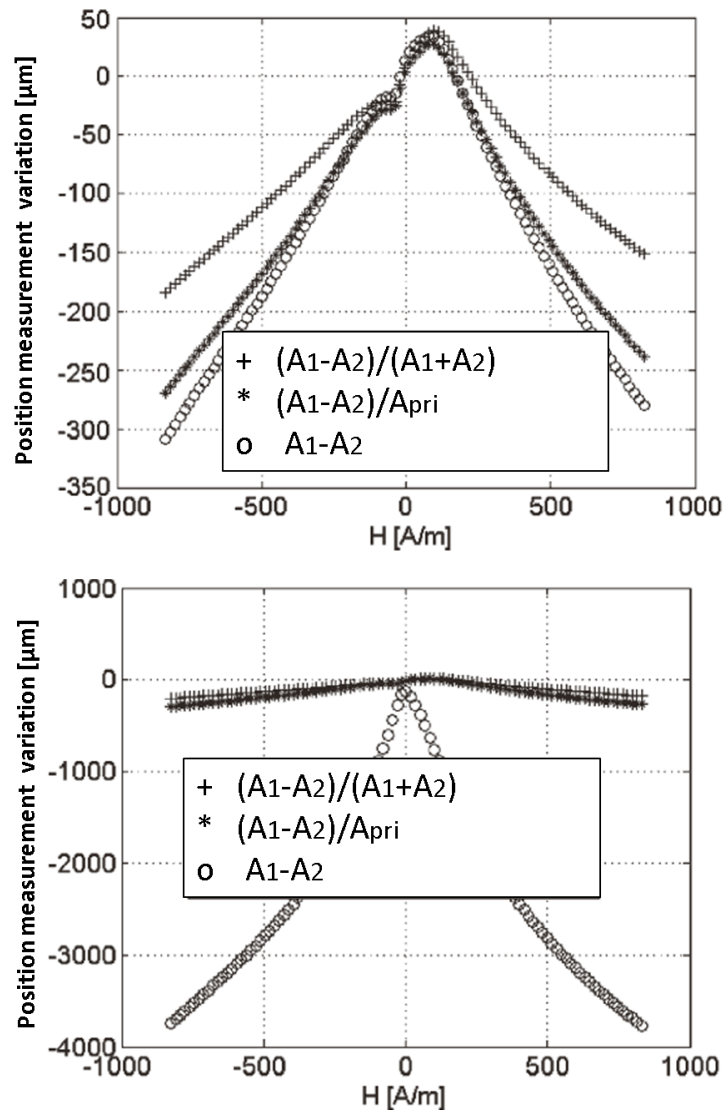
Figure 13.6: Position measurement variation at 15 mm due to a longitudinal interference of 800 A/m for different reading techniques and voltage (top) and current (bottom) excitations of $LVDT\ A$.
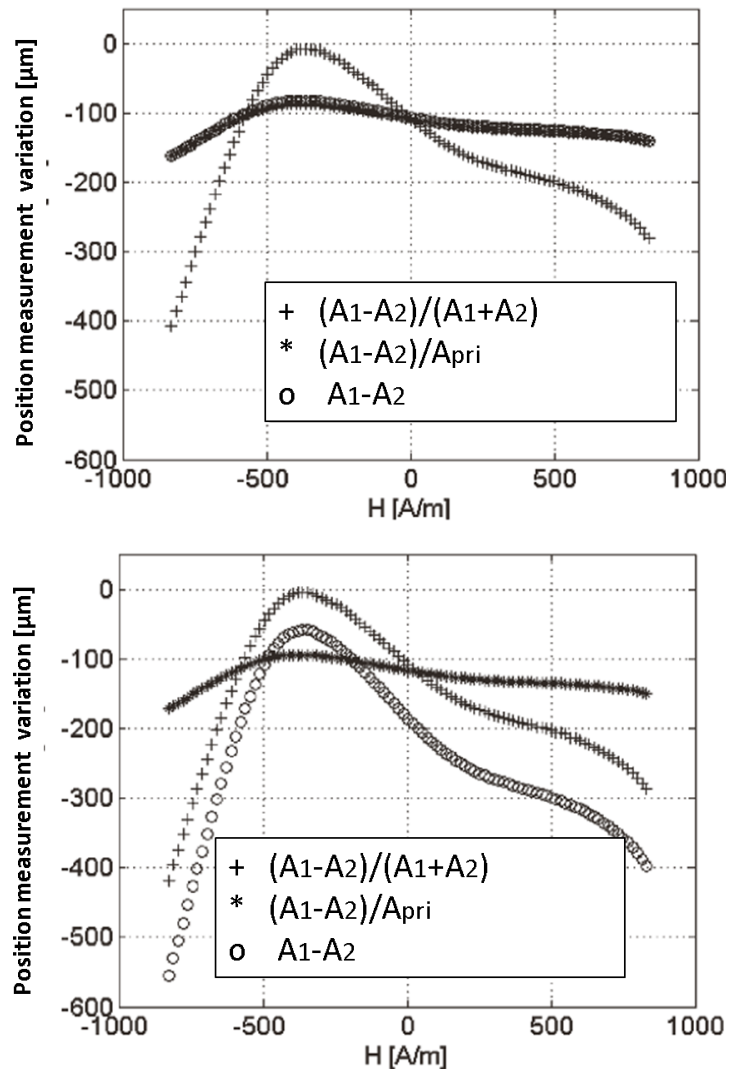
Figure 13.7: Position measurement variation at 15 mm due to a longitudinal interference of 800 A/m for different reading techniques and voltage (top) and current (bottom) excitations of $LVDT$ B.

Chapter 14

F.E.M. Model Experimental Validation

The simulation work constituted the starting point for an LVDT prototype. The dimensions, materials, geometry and coils specifications reflect the simulation criteria. All the magnetic materials were submitted to annealing. The primary coil was wound on 2 layers with a wire diameter of 0.28 mm (in order to allow possible measurements even with high currents), whereas the secondaries are single layer coils with a wire diameter of 0.06 mm, since they are supposed to be connected to high impedances, typical of DAQs. The manufactured prototype, with highlighted information, is depicted in Fig. 14.1.

14.1 Experimental Validation Procedure

A full-automatic test bench [67] was used for the LVDT prototype metrological characterization, in both standard and magnetic interference conditions. In addition, the measurements were performed in current and voltage supply. As for the F.E.M. analysis, the core position range goes from -20 to 20 mm. In particular, the measurements at different positions are preceded by an
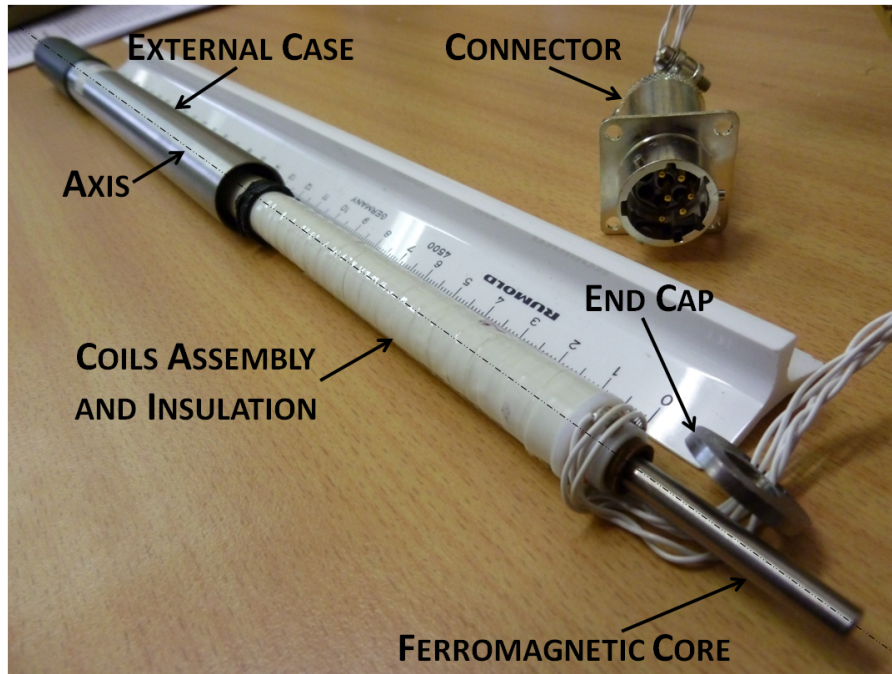
Figure 14.1: Expanded view of the custom prototype used to validate the F.E.M. model. Dimensions scale is in *cm*.

iterative search for the null point of the sensor (electric zero research) [67]. The external longitudinal magnetic field is generated by means of a calibrated solenoid, fed by a DC current in order to have the desired amplitude and a uniform field distribution along the solenoid length. In addition, a procedure has been foreseen in the measurement process [67], in order to demagnetize the magnetic circuit of the sensor and keep as fixed as possible the static working point of the equivalent $B - H$ curve during the measurement.

The measurements in absence of external magnetic field are aimed at calibrating the prototype. In presence of external field, the position is measured in reference to the previous calibration by computing variation as a difference.

As for the simulations, the position variation analysis is a relative study

aimed at pointing out the effect of the external magnetic interference.

In all the experimental results, the related expanded measurement uncertainty was calculated on 30 repeated measurements, by assuming a Gaussian distribution. A chi-square test on the repeated *electric zero* search results confirmed that the null point of the LVDT prototype follows a Gaussian distribution with a standard deviation of 6 μm. The uncertainty of the measurements at different positions is therefore dominated by this component, because the other sources of uncertainty from the test bench are negligible [67]. The expanded measurement uncertainty was computed using a coverage factor 2. The uncertainty on the position measurement variation is:

$$u_{variation} = \sqrt{u_p^2 + u_{p_0}^2} \qquad (14.1)$$

where u_{p_0} and u_p are the uncertainties on the measured position in absence and in presence of the external field, respectively. The difference between the values of such uncertainties in the different cases will be analyzed in the following subsections.

14.2   Voltage Supply

In Fig. 14.2, the prototype characteristic curve is depicted (continuous line). The measurements showed that the secondary transformation ratio of the sensor goes from 0.48 (against a value of 0.54 for the simulations) to 1.69 (against a value of 1.66 for the simulations). For the voltage amplitudes, the agreement between simulation and measurements results is good, always greater than 85 %, whereas it increases to more than 95 % when reducing to $[-10,+10]$ mm the core position range.

In Fig. 14.3, the results for the ratiometric are depicted (continuous

line). In this case, the ratiometric is a monotonic function of the position rising from about -0.58 (-0.5 for the simulations) to about 0.57 (0.5 for the simulations). Measurements results show a more pronounced nonlinearity, especially for high core position ranges (1.11 % in $[-20,20]$ mm). In Fig. 14.3 the influence of the ratiometric reading on the match between simulations and measurements can be highlighted. As a matter of fact, while the match on the secondary voltages is more than 85 %, on the ratiometric is 83 %. Furthermore, such effect does not act uniformly on all the positions.
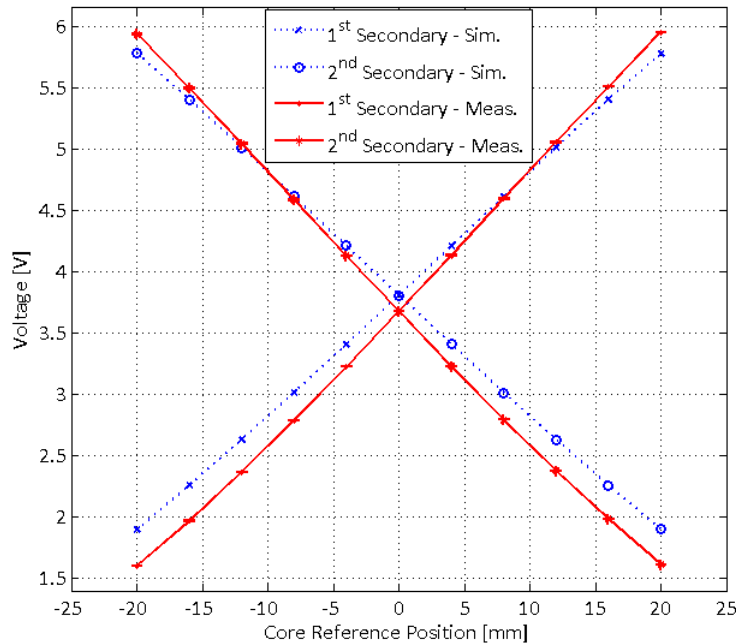
Figure 14.2: LVDT secondary characteristic curve simulations and measurements results (voltage supply).

Regarding the interference conditions, the related position measurement variation is presented in Fig. 14.4 (continuous line). The position measurement variation at 0 mm is zero in the simulations and in the measurements (mean value): this is due to the fact that when the core is in the center,

the interference effect on the two secondary windings is the same, resulting in a non-perturbed ratiometric reading (i.e. the measured position is not affected). In addition, the good agreement between simulations and measurements (almost always within the uncertainty in Fig. 14.4) gets even better when considering only negative positions. As a matter of fact, the agreement in this area is more than 90 %. For positive positions the agreement decreases. In other words, the intrinsic symmetry of the position measurement variation of simulations (Fig. 14.4, dotted line) is not fully reflected by the measurements (Fig. 14.4, continuous line). In fact, for both simulations and measurements the variation is positive for negative positions, negative for positive positions and null at 0 mm, but in the measurements the variation goes from 71 μm (72 μm for the simulations) to -44 μm (-72 μm for the simulations). Such discrepancies are due to slight (micrometric order) asymmetric wire assembly of the prototype. Anyway, the overall agreement between F.E.M. model and experiments is good.

In Fig. 14.4 (continuous line), the measurement uncertainty is meanly around 20 μm. This uncertainty depends, of course, on the position uncertainty (14.1). These values are nevertheless higher than the corresponding values found in [67]. This is explained by taking into account that this prototype exhibits a high voltage swing (Fig. 14.2 and Tab. 14.1), and thus a big slope of the voltage-position characteristic. Therefore, the uncertainty on the voltages is higher (with respect to the ones found in [67]) and thus on the measured position.
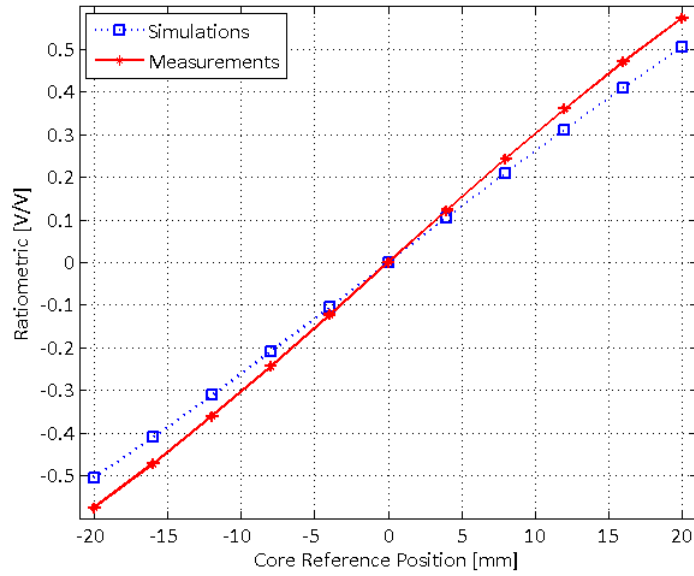
Figure 14.3: Ratiometric simulations and measurements results (voltage supply).
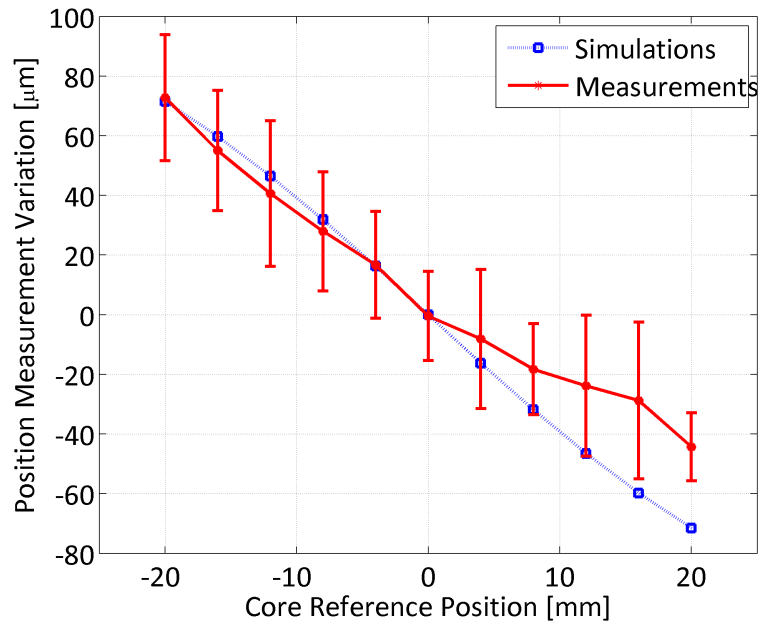
Figure 14.4: Position measurement variation simulations and measurements results (voltage supply).

14.3   Current Supply

The measurements in current supply were performed by a sine wave with a peak of 23.0 mA. This ensures a first harmonic of the primary voltage of 3.5 V when the core is in null position. This value is in agreement with the simulations regarding the primary impedance. In Fig. 14.5 (continuous line) the measured characteristic curve in current supply is shown. The measured ratios go from 0.48 (0.54 in simulations) to 1.70 (1.66 in simulations). The agreement on the amplitudes is good in this case too, more than 86 %. Such a value increases to 94 % when reducing to $[-10, 10]$ mm the core position range.

In Fig. 14.6, the behavior of the ratiometric values with respect to the core position is shown (continuous line). The ratiometric ranges from -0.57 (0.50 in simulations) to 0.57 (0.50 in simulations). In this case, the non linearity (10.2) is 1.12 % in $[-20,20]$ mm. As for the voltage supply, the ratiometric reading affects non-uniformly the match between simulations and measurements because the agreement is equal to 84 % in the worst case. For the interference, the results of the position measurement variation are depicted in Fig. 14.7 (continuous line). As for the simulations, the position measurement variation is a monotonic function of the core position and its value for null position is null on turn. In addition, the agreement with F.E.M. results is good, especially for negative positions (as already observed with voltage supply), because simulations are almost always compatible with the measurements. The secondary voltage amplitude of an LVDT can be expressed as [68]:

$$A_i \propto I_p M_{ip}(p) m(H_{ext}) \tag{14.2}$$

where I_p is the amplitude of the primary current, M_{ip} is the mutual inductance between the ith secondary and the primary, m is an adimensional factor taking into account the dependence of such mutual inductance on the external magnetic field. When an external field is applied, the voltage variation is:

$$\Delta A_i \propto I_p M_{ip}(p) \Delta m \tag{14.3}$$
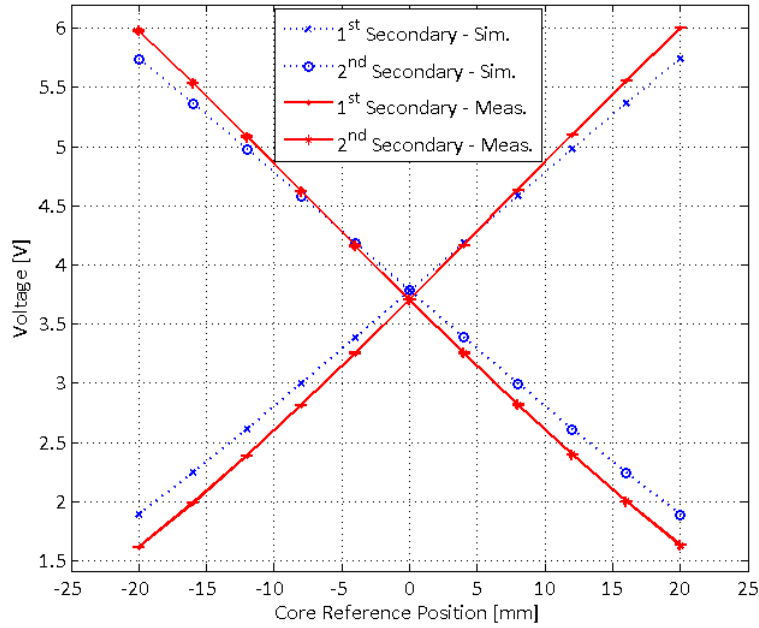
Figure 14.5: Simulations and Measurements results regarding the LVDT secondary characteristic curve (current supply).

Consequently, the dependence of the position measurement variation on the position itself will be connected with the mutual inductance (being the only factor function of the position in (14.3)). Therefore, the agreement on the slope of the variation-position curve (Fig. 14.7) has to be expected similar to the agreement on the slope already observed for the voltage-position curve
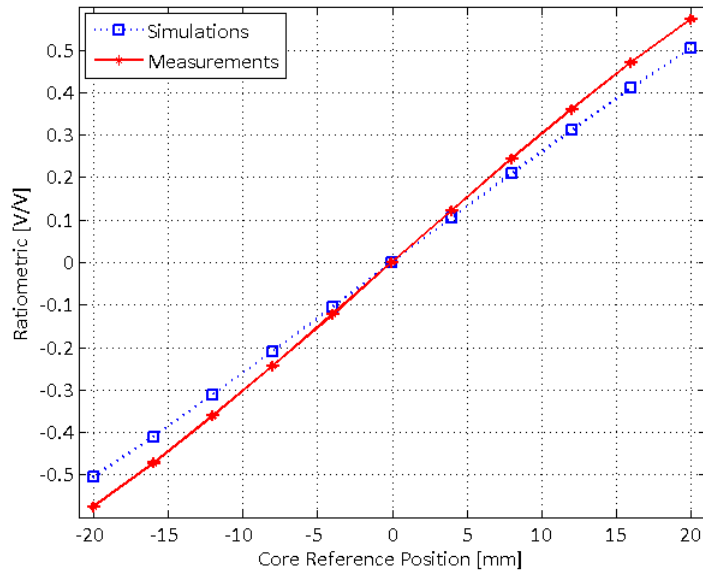
Figure 14.6: Ratiometric simulations and measurements results (current supply).
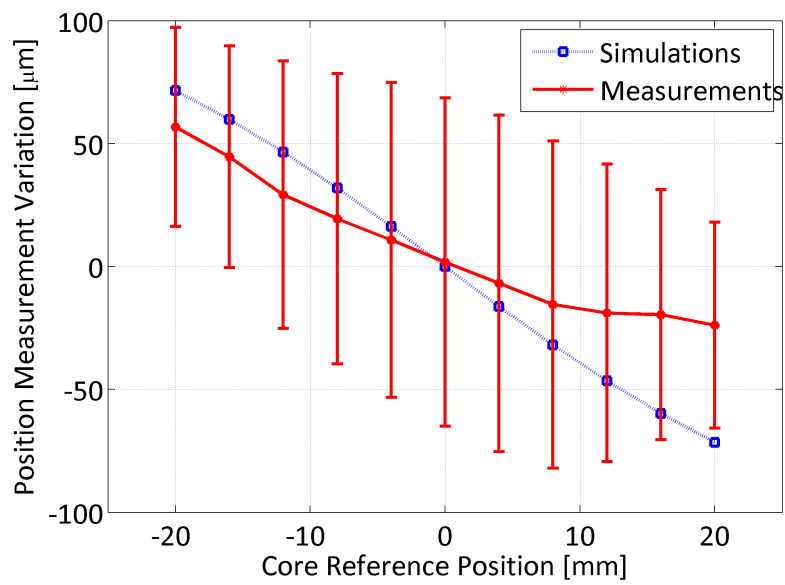
Figure 14.7: Position measurement variation simulations and measurements results (current supply).

in Fig. 14.5, namely 84 %. According to the model presented in [68], this is valid for current supply. Regarding the measurement uncertainty on the position variation, in this case it is higher than the corresponding with voltage supply. Actually, with current supply the uncertainty on the primary voltage is higher (the primary voltage is not fixed by the generator), as reported in Tab. 14.1, leading to a higher uncertainty on the secondary voltages and finally on the position measurement variation. A complete overview of the results in different supply cases and the comparison with simulations is reported in Tab. 14.1.

Item	Voltage Supply	Current Supply
Feeding Signal Amplitude	3.5 V (**3.5**)	23.0 mA (**24.0**)
Transformation ratio	from 0.48 (**0.54**) to 1.69 (**1.66**)	from 0.48 (**0.54**) to 1.70 (**1.66**)
Ratiometric Range	from -0.58 (**-0.50**) to 0.57 (**0.50**)	from -0.57 (**-0.50**) to 0.57 (**0.50**)
Voltage Swing (V)	4.30 (**3.90**)	4.35 (**3.90**)
Non Linearity Error (%)	1.11 (**0.7**) in $[-20\ mm, 20\ mm]$ 0.14 (**0.11**) in $[-10\ mm, 10\ mm]$	1.12 (**0.7**) in $[-20\ mm, 20\ mm]$ 0.15 (**0.11**) in $[-10\ mm, 10\ mm]$
Primary Voltage Repeatability (mV)	±0.8 (no interference) ±2.5 (interference)	±1.5 (no interference) ±8 (interference)
Secondary Voltage Repeatability (mV)	±1.6 (no interference) ±2.9 (interference)	±2.1 (no interference) ±8.8 (interference)
Measured Position Uncertainty (μm)	11 (no interference) 15 (interference)	13 (no interference) 52 (interference)
Position Variation Values (μm)	from 71 (**72**) to -44 (**-72**)	from 58 (**72**) to -25 (**-72**)
Position Variation Uncentainty μm	19	55
Agreement with Simulations (Characteristic Curve) (%)	> 85 in $[-20\ mm, 20\ mm]$ > 95 in $[-10\ mm, 10\ mm]$	> 86 in $[-20\ mm, 20\ mm]$ > 92 in $[-10\ mm, 10\ mm]$
Agreement with Simulations (Ratiometric) (%)	> 83	> 84

Table 14.1: Summary of Experimental Results. Position variation is intended as a short for position measurement variation.

Chapter 15

Simplified Analytical Model Experimental Validation

Simulations results reported in Chapter 9 showed that the *equivalent coil permeabilities* of Section 6.3 model the LVDT working accurately enough to be exploited for experimental validation. In order to magnify the hysteresis, a prototype according to the structure described in Section 6.3 but with non annealed materials was built.

15.1   Model Validation Technique

According to the harmonic expansion (6.17), and considering that $H_{ac} \geq 0$, the component $2f_0$ is given by:

$$A_{v_i}^{2f_0} = \pi f_0 H_{ac}^2 S_{\gamma_i} \left| \partial \mu_{dc}^{(i)} + \sum_{\substack{n>1 \\ n \text{ odd}}} \frac{H_{ac}^{n-1}}{2^{n-1}} \frac{\partial^n \mu_{dc}^{(i)}}{\left(\frac{n-1}{2}\right)! \left(\frac{n+1}{2}+1\right)!} \right| \tag{15.1}$$

By neglecting all the terms in the summation in (15.1), by differentiating (6.19) and considering that $\mu_d^{(i)}$ is nonnegative (thus the absolute value does not affect the derivative), the following approximated relationship holds:

$$\left| \frac{\partial}{\partial H_{dc}} \frac{A_{v_i}^{f_0}}{2\pi f_0 H_{ac} S_{\gamma_i}} \right| \approx \frac{A_{v_i}^{2f_0}}{\pi f_0 H_{ac}^2 S_{\gamma_i}} \qquad (15.2)$$

The main idea for the validation of the proposed model is therefore to verify that these two quantities are compatible.

15.2   Measurement Results

The configuration with current supply of the experimental setup [61], [67] described in Chapter 13 was exploited for this validation.

The first two harmonics of both the secondary voltages were measured during a complete cycle of the external magnetic field (corresponding to a magnetic flux density of ± 1 mT in air) for different positions.

In Figs. 15.1 and 15.2 the results, corresponding to a position where the two secondary amplitudes are very different (≈ -10 mm), are reported both with a typical *butterfly* shape [69]. Both the secondary voltages have the same shape; only amplitudes are different. The peaks of the first harmonics are located approximatively in the same position of the minima of the second harmonics. Their location is an effect of the hysteresis and is related to the coercive forces of the Alloy 48 of the core. The distance depends on the area of the "equivalent" hysteresis cycle. The relatively large cycle is due to the not annealed core. This usual drawback is useful for the model validation.

The model was validated by comparing the following quantities, directly related to the measurement results:
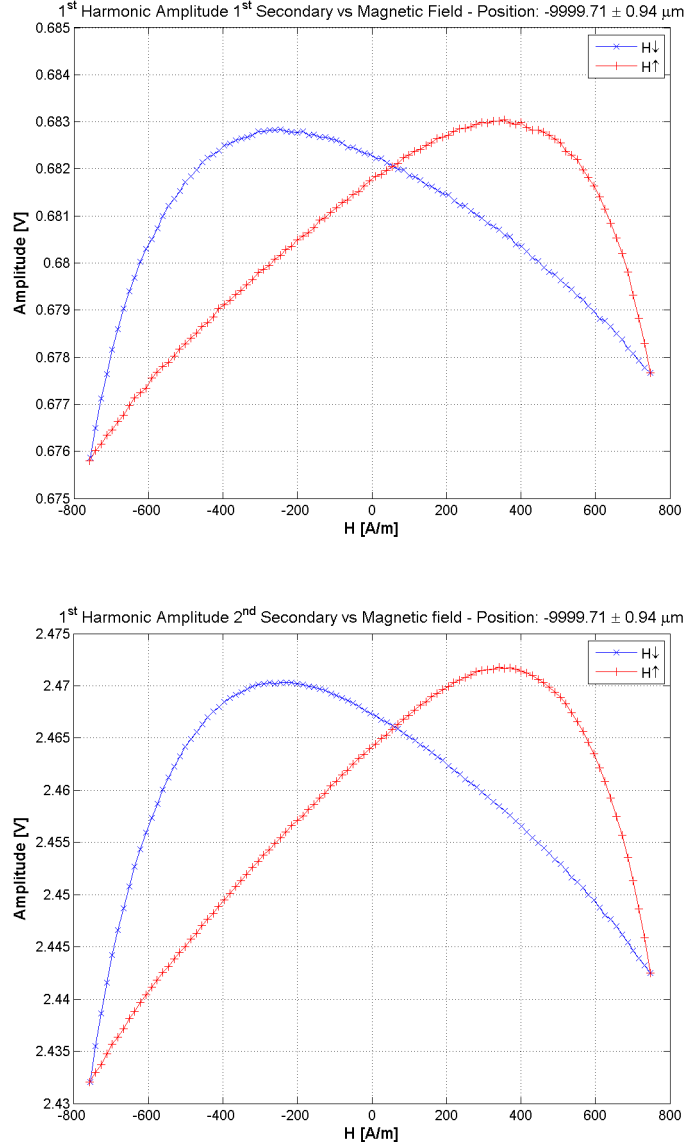
Figure 15.1: Amplitude of the first harmonic of the two secondaries (top: first, bottom: second) vs External Dc Field at $p = -9999.71 \mu m \pm 0.94 \mu m$

$$\left| \frac{\partial}{\partial H_{dc}} \frac{A_{v_i}^{f_0}}{2\pi f_0 H_{ac} S_{\gamma_i}} \right| =$$
$$= \left| \frac{\partial}{\partial H_{dc}} \left| \mu_d^{(i)}(H_{dc}) + \sum_{n \text{ even}} \frac{H_{ac}^n}{2^n} \frac{\partial^n \mu_{dc}^{(i)}}{\left(\frac{n}{2}\right)! \left(\frac{n}{2}+1\right)!} \right| \right| \quad (15.3)$$
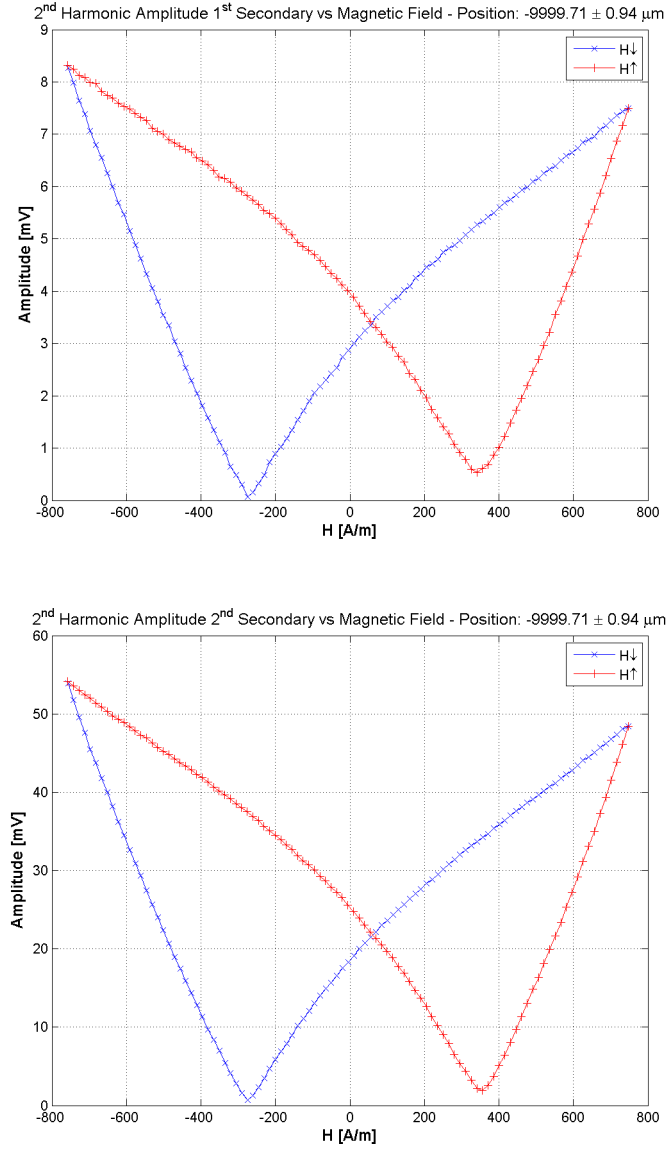
Figure 15.2: Amplitude of the second harmonic of the two secondaries (top: first, bottom: second) vs External Dc Field at $p = -9999.71\mu m \pm 0.94\mu m$

$$\frac{A_{v_i}^{2f_0}}{\pi f_0 H_{ac}^2 S_{\gamma_i}} = \left| \partial \mu_{dc}^{(i)} + \sum_{n \text{ odd}}^{n>1} \frac{H_{ac}^{n-1}}{2^{n-1}} \frac{\partial^n \mu_{dc}^{(i)}}{\left(\frac{n-1}{2}\right)! \left(\frac{n+1}{2}+1\right)!} \right|. \tag{15.4}$$

In Figs. 15.3 and 15.4, the results are reported for the first and the second secondary voltages, respectively.

The overall agreement between the absolute value of the numerical derivative of the first harmonic, scaled by $2\pi f_0 H_{ac} N_{sec} S_{sec}$ and the amplitude of the second harmonic, scaled by $\pi f_0 H_{ac}^2 N_{sec} S_{sec}$, is satisfying. For the first secondary, the numerical derivative is more noisy due to the relatively smaller amplitude of the signals with respect to the second secondary.

Once the minimum is reached, the data match when the external field increases or decreases; e.g. in the decreasing case the best match is on the left of the minimum, i.e. after the coercive force has been passed. When the field is increasing the situation is exactly dual. The lack of complete agreement in the previous phase, that is to say when the field has not reached the "equivalent" coercive force yet, needs for further investigation.

Finally, the very-small absolute value of the derivative of the "equivalent" differential permeability is due to the non negligible part of the secondary circuit made of air, and to the important demagnetization effect in the core.
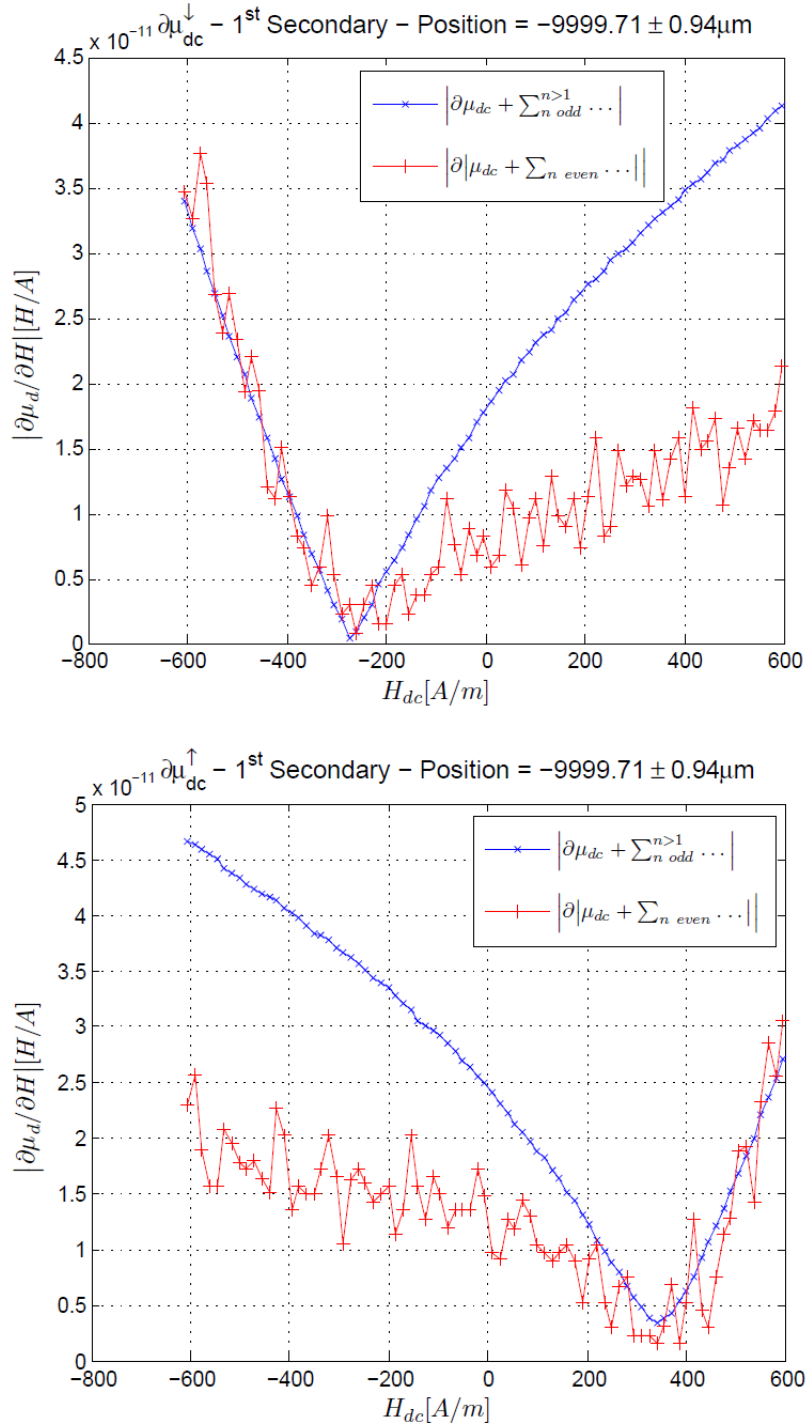
Figure 15.3: Comparison between (15.3) and (15.4) for the 1st secondary vs External Dc Field (top: decreasing, bottom: increasing) at $p = -9999.71\mu m \pm 0.94\mu m$
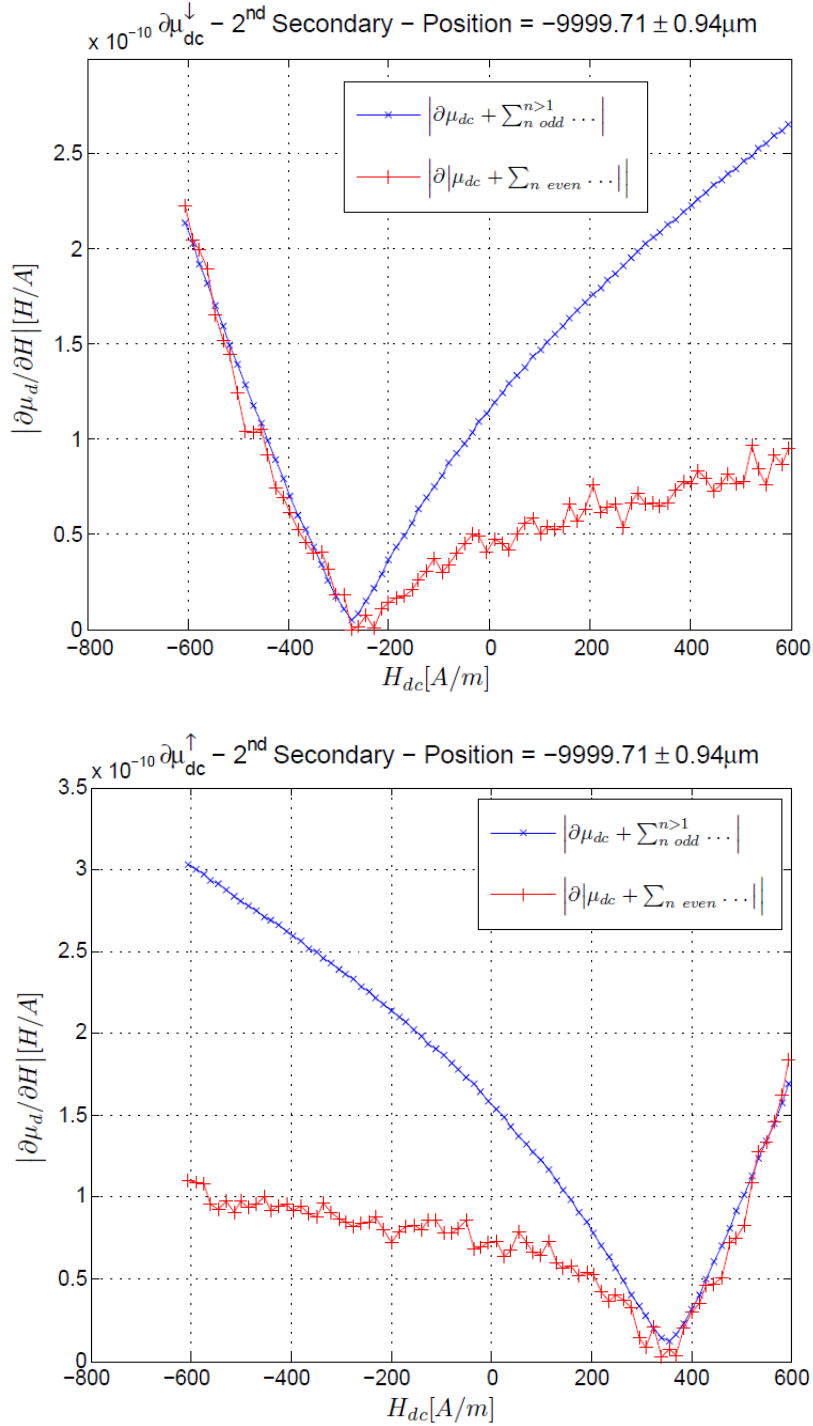
Figure 15.4: Comparison between (15.3) and (15.4) for the 2nd secondary vs External Dc Field (top: decreasing, bottom: increasing) at $p = -9999.71\mu m \pm 0.94\mu m$

Chapter 16

Preliminary on-field results of the position measurement instrument

In this Chapter, preliminary on-field operation results of the collimators' position measurement system are reported. The measurement setup comprising the *LHC* collimators' control architecture is described, then the measurement conditions and the static and dynamic test procedures, with particular attention to the synchronization issue, are illustrated. Finally, the repeatability and the stability of the instrument are evaluated.

16.1 Measurement Set up

16.1.1 LHC Collimators' Control Architecture

Since *LHC* operations start, the collimators' control has played a fundamental role. Beam collimation at *LHC* is, indeed, needed in all the operational phases, from injection to top energy (while the beams are being squeezed), as well as during the long periods physics taking data. In order to ensure optimum settings at all times, collimators are moved following predefined functions of time, or motion profiles, during each machine phase [70]. Colli-

mators' jaws must follow the variation of local beam orbit and size.

In Figs. 16.3 and 16.2, the architecture of the LHC collimators' control software and hardware, respectively, are presented. Beyond the *PRS* it is possible to identify:

- the Motor Drive Control (*MDC*) system (Fig. 16.2) responsible for the generation of the stepping pulses and the resolvers' monitoring for up to three collimators. It receives motion commands from the top level (Fig. 16.1), verifies their consistency and checks, in real-time, for lost steps during the execution of the motion profiles; the trajectory generation running on the host produces the set points, sent via a *FIFO* to the *FPGA* where a step generation loop, operating at 1 MHz actually produces the pulses for each collimator axis. Each axis' resolver is read synchronously with respect to the generated steps at up to 400 Hz.

- the *Collimator Gateway* concentrates all the data accesses from the top level application via a standard CERN middleware server and establishes one to one connections with the collimators' control systems through the Data Interchange Management *DIM* protocol [35]. A gateway is installed in each LHC collimation point [3], in order to supervise all the systems of the point and synchronize different points. The real-time actions (such as *MDC* motion start or *PRS* monitoring start) are triggered through pulses sent via optical fiber directly to the *PXI* FPGA cards. All the gateways are equipped with a timing network [3]. This provides not only LHC timestamps, but also machine status information, such as beam energy, machine cycle and so on.

- the Central Control Application (*CCA*) [71] (Fig. 16.1) is responsible

for generating and orchestrating the settings for the system as a whole, for sending them to all devices, and for monitoring the aspects relevant for beam operation.
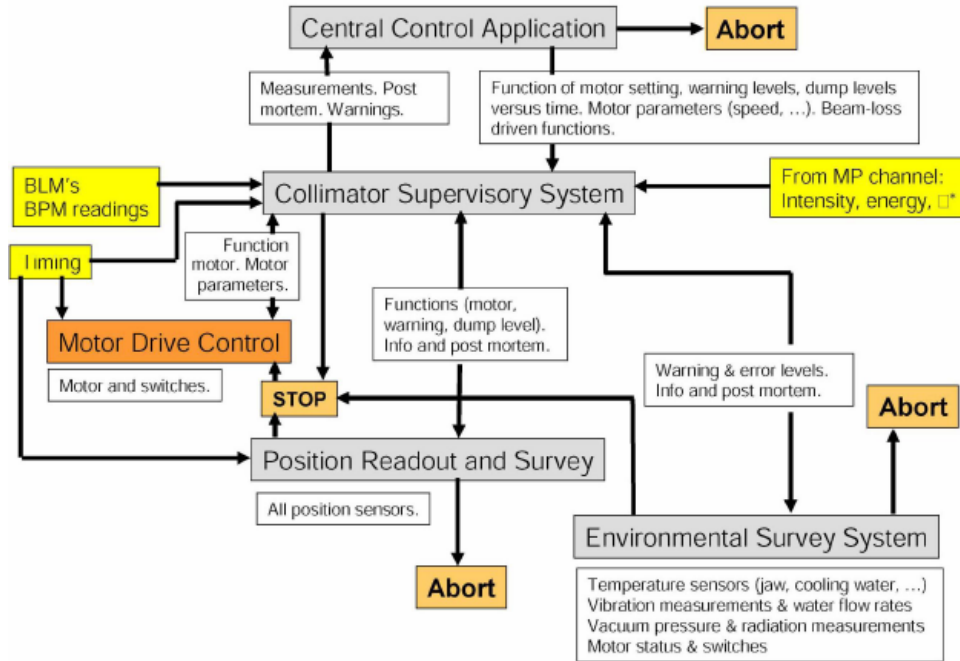
Figure 16.1: Layout of the LHC collimators control system.

16.1.2   Measurement Conditions

In the preliminary on-field tests, the nominal operating conditions of *LHC* during its different operations were considered. As a fundamental part of *LHC*, collimators are subject to the environmental conditions of the *LHC* tunnel, exhibiting rather stable values of temperature and humidity during its nominal operation. A pervasive and highly redundant diagnostic equipment is responsible for monitoring a huge number of operational parameters and for triggering opportune countermeasures whenever these parameters go out of predefined bounds.
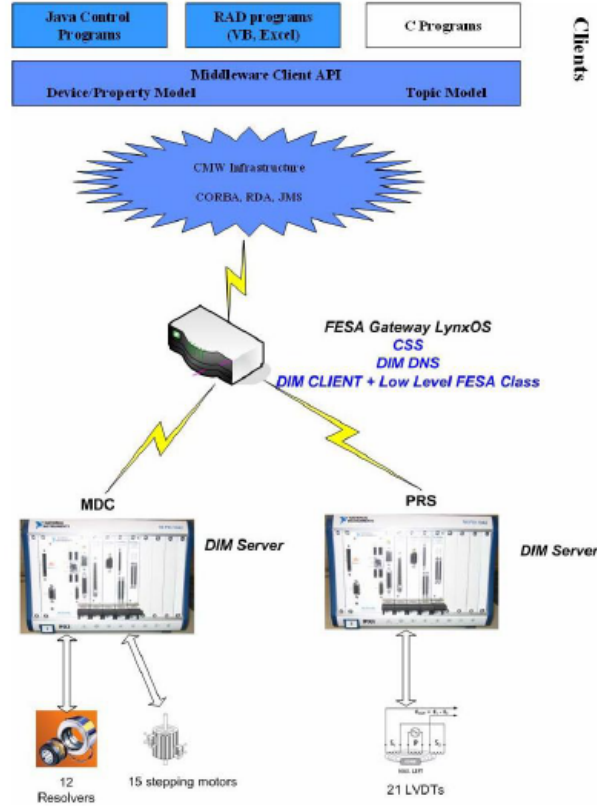
Figure 16.2: Hardware architecture of the LHC collimators control system.

The measurement conditions hereby analyzed comprise, therefore, the same measurement procedure, operators (belonging to the teams responsible for *LHC* machine operation), measuring system, and operating conditions as in the *LHC* tunnel. The metrological figures considered are, therefore, the measurement repeatability and the stability of the instrument.

16.2 Test Procedure

During the test, mainly two different operation conditions have been considered: *(i)* static conditions, where the collimators' jaws are kept fixed to given positions, and *(ii)* dynamic conditions, occurring during energy ramps, where
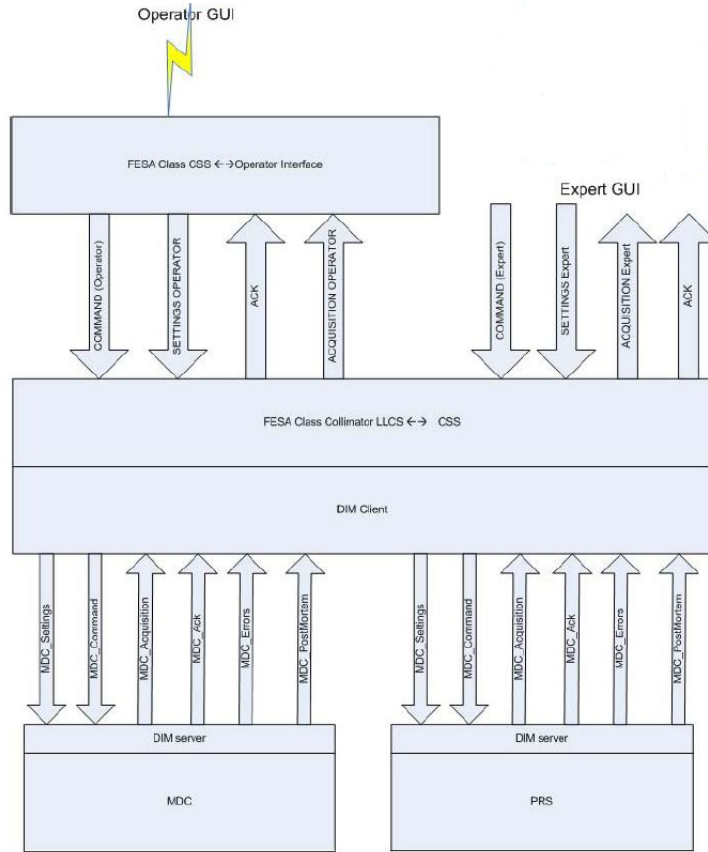
Figure 16.3: Software architecture of the LHC collimators control system.

the collimators' jaws must follow their demanded motion profiles within tight bounds.

In dynamic conditions, the quantity of interest is the difference between the demanded position at a given time and the position measured by *PRS*. Clearly this difference is determined not only by the performance of the *PRS* but also by the performance of the actuation chain governed by the *MDC*. Nevertheless, this is the relevant parameter for the correct operation of the machine. Being dynamic results greatly influenced by time, the key feature of the system is therefore its accurate synchronization.

Average trigger delay	Trigger response jitter	Profile stop jitter
120 μs	4 μs	50 μs

Table 16.1: *MDC* Timing Performance

16.2.1 *MDC* timing characterization

The *MDC* timing behavior was characterized by means of three parameters [72]:

- *trigger response delay*: the time between the trigger reception and the generation of the first pulse for the stepping motor drive;

- *trigger response jitter*: the standard deviation of the trigger response delay in the execution of different motion profiles;

- *profile stop jitter*: the standard deviation of the profile execution time due to the drift of the *FPGA* clock.

The *average trigger response delay* and the *trigger response jitter* were evaluated over 30 repeated triggered displacements 30 minutes long each. The *profile stop jitter* has been calculated as the standard deviation of the motion profile execution times evaluated as the time elapsed between the first and the last generated stepping pulse in order not to take into account the start trigger jitter. The results are shown in Tab. 16.1.

It turned out that the two axes of a single jaw are nevertheless synchronized at the μs level since the steps generation for all the axes of a single collimator is performed in the same 1 MHz *FPGA* loop [72]. More details about the operational performance of the whole *LHC* collimators' positioning system can be found in [72], [70], [71].

16.3 Experimental Results

16.3.1 Static Test Conditions

For the static operational conditions, the distribution of the $1 - \sigma$ repeatability of all jaws' positions measurements of all LHC collimators has been evaluated over 100 repeated measurements (observation time of 1 s at a reading rate of 100 $readings/s$). Only a small number of measurements exhibit repeatability greater than ±1 μm (Fig. 16.4), whereas almost all the 648 jaws' positions measurement repeatabilities are below ±0.8 μm.

A longer test aimed, at evaluating the instrumental stability, was carried out. This test lasted 3 weeks and involved a reduced number of collimators with 85 jaws' positions measurements. The distribution of the stability, assessed as the maximum deviation from the initial reading, is depicted in Fig. 16.5.
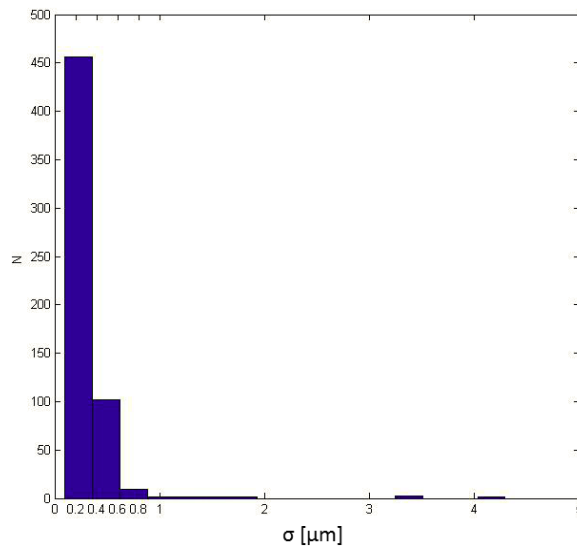
Figure 16.4: Distribution of the repeatability ($1 - \sigma$; 100 repeated measurements) of 648 jaws' position measurements.
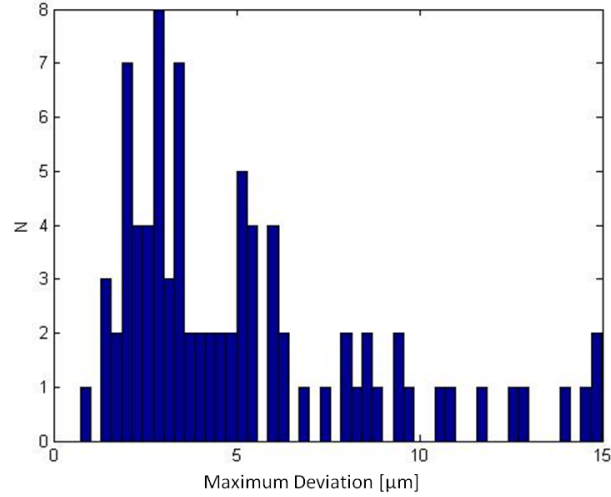
Figure 16.5: Distribution of the instrumental stability (85 jaws over 3 weeks).

16.3.2 Dynamic Test Conditions

For dynamic tests, a key parameter is the synchronization accuracy. At a given time instant, the difference between the current position measurement of a jaw and its requested position during the motion profile has sense only if the two clocks are synchronized accurately. The issues of synchronization between the motion profiles and the monitoring profiles are extensively addressed in [72].

Just after a synchronization, the maximum deviation between the general LHC and any of the installed PRS timestamps was measured less than 5 μs [72]. For the PRS jitter, a procedure involving 30 repeated execution of 30-minutes long monitoring profiles was performed analogously as in 16.2. The results are summarized in Tab. 16.2. The maximum speed allowed for any collimator's jaw is equal to 2×10^3 $\mu m/s$, i.e. a deviation of 2 μm per ms of time de-synchronization.

As an example, a single motion profile and the deviation between the

Start monitoring jitter	Stop monitoring jitter	Monitoring duration jitter
1.6 ms	2 ms	1.8 ms

Table 16.2: *PRS* Synchronization Performance

measured and the requested position are depicted in Fig. 16.6. The deviation is within $\pm 10 \ \mu m$. This testifies how both the actuation system and the position measurement instrument operate according to their specifications.

With reference to the deviation profile depicted in Fig. 16.6, the maximum deviation over the profile was then memorized for all the 648 jaws during $5 - TeV$ energy ramp profiles, subsequently, repeated 11 times in a specific test. The distribution of the $1 - \sigma$ repeatability, assessed as standard deviation of the maximum deviations, is depicted in Fig. 16.7 (Tab. 2.2 for jaws' and gaps naming convention). The distribution shows how the large majority the jaws' positions repeatabilities is below $\pm 3 \ \mu m$ and none of them exceeds $\pm 10 \ \mu m$.

This result of a worst case repeatability among all the jaws' position measurements of about $\pm 10 \ \mu m$, was recently confirmed during operations in 2011 [70]. In Figs. 16.8 and 16.9, the results of 25 *fill* profiles for high-intensity physics of one primary and one tertiary *GAP* collimators, respectively, are depicetd. The repeatability of the profiles was maintained over periods of weeks to months [70].
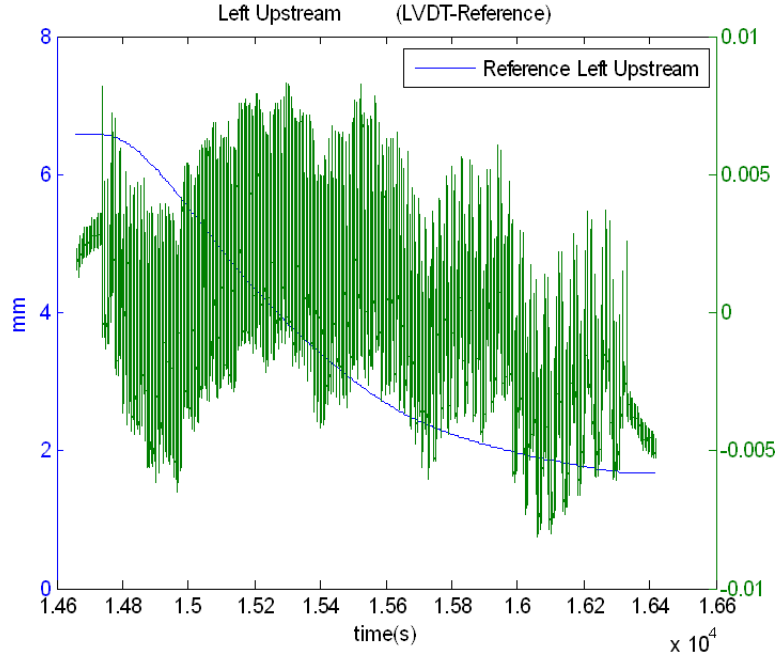
Figure 16.6: Left Upstream deviations of position measurement from the reference during the profile execution.
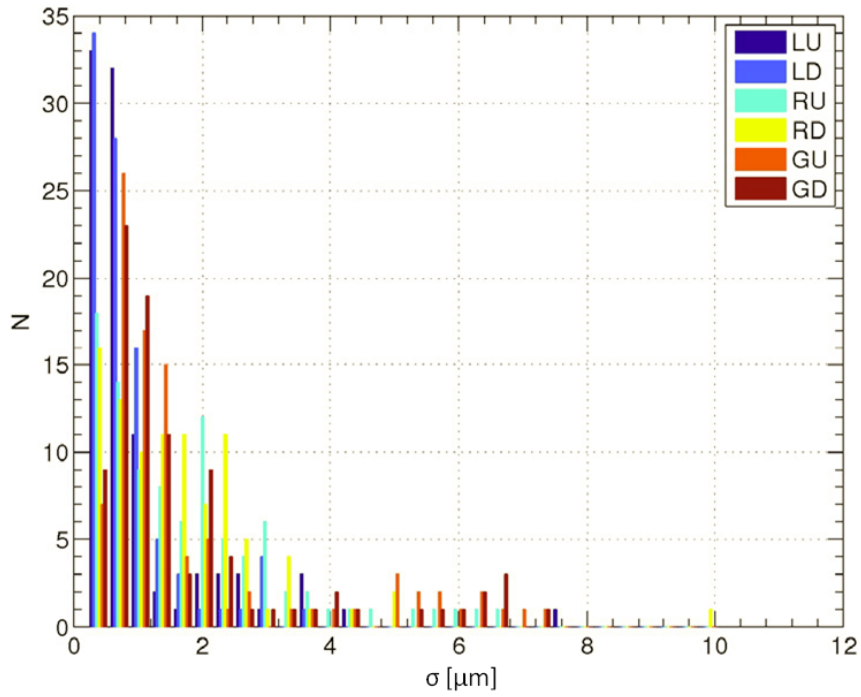
Figure 16.7: Distribution of measurement repeatability, $1 - \sigma$ over 11 ramps.
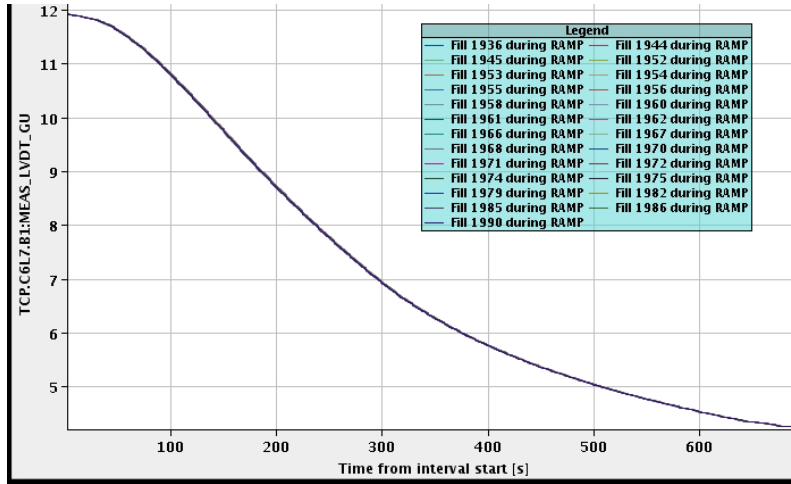
(a) First part of the profile.
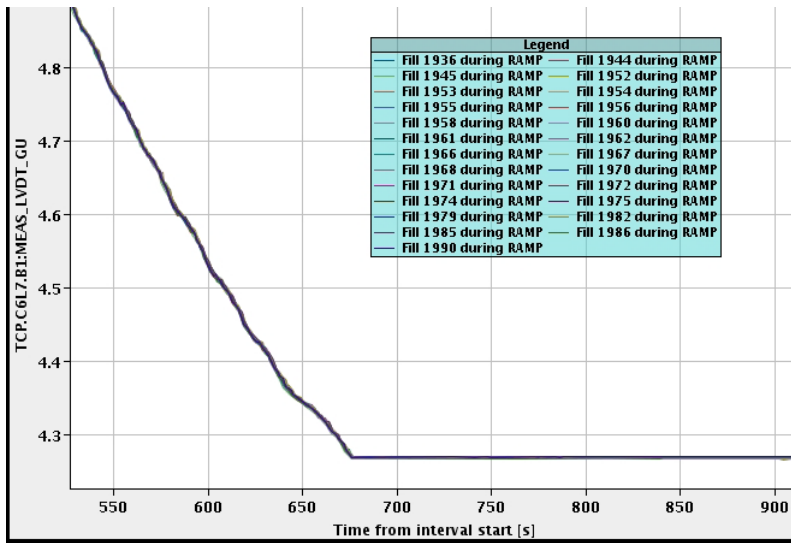
(b) Second part of the profile.

Figure 16.8: Gap of a primary collimator as a function of time. (*y-axis* in *mm.*)
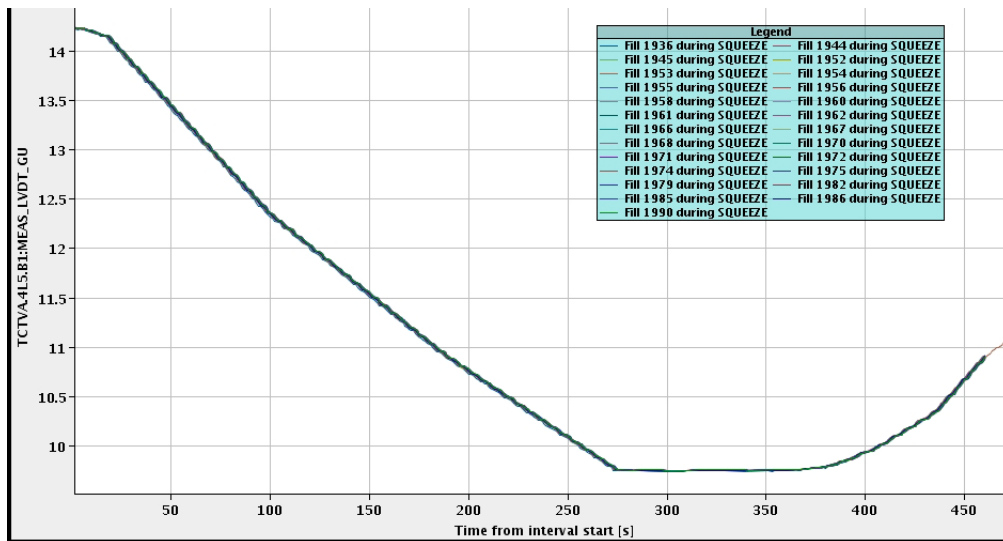
Figure 16.9: Gap of a tertiary collimator in the *LHC* experimental region as a function of time. (*y-axis* in *mm.*)

Conclusions

The purpose of this thesis is to contribute to face the more and more challenging engineering issues related to monitoring collimation of high-energy particle accelerators. In literature, a too little attention is paid to the technology involved in collimators positioning systems, more and more demanding in terms of accuracy.

A high-precision digital instrument for collimators' position measurement able to cope with the demanding *LHC* collimators control system requirements has been proposed. The original contributions that constitute the main focus of this work are twofold.

At one end of the measuring chain, at the physical layer of the instrument, external slowly-varying magnetic field is clearly identified as an influence quantity of the position of LVDT sensors. This is a critical issue for the *LHC* collimators control system, particularly in the *LHC* transfer lines, where collimators are close to cables conducting pulsed currents. Clearly, this is a more general problem for high-precision position measurement based on LVDTs, whenever the sensors are installed close to devices with significant stray magnetic fields such as motors, line transformers, and so on.

Given the novelty and the generality of the problem, an iterative process involving all the phases of modeling, measurement, and design was defined.

An analytic and an F.E.M. models have been proposed in order to capture the main physics of the interference and to accurately characterize its effects, respectively. Furthermore, an original measurement method was conceived and an actual measurement system was designed and realized with the twofold purpose of *(i)* characterizing commercial LVDTs with respect to such an influence quantity, and *(ii)* experimentally validating the proposed models by means of ad- hoc built prototypes.

The measurement system itself was characterized and exhibits a measurement uncertainty of a few μm. Whereas the variation due to the *influence quantity* external magnetic field can be up to two orders of magnitude bigger in the operating conditions of collimators in *LHC* transfer lines. Design guidelines for the solution of such a problem, in general terms, were also proposed. They consist in an innovative magnetic shielding and a DC polarization of the magnetic materials of the LVDT. They were conceived starting from the analytic modeling developed and their effectiveness was proven by means of the validated F.E.M. model.

On the opposite end of the measuring chain, at the top of the hardware/software layer, where significant literature was conversely available, the original contribution involved the design of a computationally-effective multichannel estimator of the LVDTs' secondary voltages amplitudes, constituting the computational core of the proposed instrument. The design of the estimator, based on the standard three-parameter sine fit, exploited an analytical metrological analysis, specifically developed at this aim.

On the basis of the analytical characterization of the *SNR* and frequency response of the estimator in terms of its design parameters, namely the sampling frequency and the number of samples, the problem of cross-talk due

to multi-wire cables connecting the LVDTs to the measurement electronics was efficiently solved, ab origine, by choosing up to 7 orthogonal frequencies. Whereas the potentially low SNR of the input signals was enhanced by a factor of about $N/2$, being 2000 the samples currently used by the estimator of the PRS.

In laboratory tests, the $1 - \sigma$ repeatability of the amplitude measurement resulted smaller than ± 20 ppm of full scale. This led to a position measurement $1 - \sigma$ repeatability smaller than ± 100 ppm of full scale.

Preliminary, on-field, results gathered by the teams responsible for LHC operations, during commissioning and physics test sessions along 2009 and 2011, confirmed the laboratory metrological characterization if the instrument. This, important, *third-party* validation has proven its compliance with the demanding requirements of LHC collimation system.

With a look at the future upgrade of LHC planned for the next years, further developments are going to be required, especially concerning the critical issue of external magnetic fields affecting the instrument's accuracy. By exploiting the analysis and simulation tools developed along this thesis, and by following the proposed design guidelines, several improvements are likely to be investigated such as:

- design optimization of the magnetic shielding, for reducing its dimensions in order to simplify its installation on on-field working equipment;

- development of a combined strategy including shielding of magnetic field sources in proximity of the collimators;

- analysis and design of closed loop compensation techniques by means of suitable detection logic of the external field and DC polarization of

the LVDT primary circuit;

- development of new, LVDT-like, sensors able to combine LVDT's strong points with high immunity to external magnetic fields.

Appendices

Appendix A

A.1

To minimize (5.6) it suffices to evaluate the gradient of e^2 and equate it to zero and check that the Hessian matrix is positive definite. The derivative rules are:

$$\begin{array}{rcl}
\nabla_{\mathbf{x}}\left(\mathbf{y}^T\mathbf{A}^T\mathbf{x}\right) & = & \mathbf{A}\mathbf{y} \\
\nabla_{\mathbf{y}}\left(\mathbf{y}^T\mathbf{A}^T\mathbf{x}\right) & = & \mathbf{A}^T\mathbf{x}
\end{array} \tag{A.1}$$

By applying the rules in (A.1) to (5.6) yelds:

$$\begin{array}{rcl}
\nabla_{\mathbf{x}}\left[(\mathbf{y}-\mathbf{D}\mathbf{x})^T(\mathbf{y}-\mathbf{D}\mathbf{x})\right] & = & \nabla_{\mathbf{x}}\left(\mathbf{y}^T\mathbf{y}-\mathbf{y}^T\mathbf{D}\mathbf{x}-\mathbf{x}^T\mathbf{D}^T\mathbf{y}+\mathbf{x}^T\mathbf{D}^T\mathbf{D}\mathbf{x}\right) \\
& = & -2\mathbf{D}^T\mathbf{y}+2\mathbf{D}^T\mathbf{D}\mathbf{x}
\end{array} \tag{A.2}$$

By equating (A.2) to zero the, so called, *normal equation* is derived as:

$$\mathbf{D}^T\mathbf{D}\mathbf{x} = \mathbf{D}^T\mathbf{y} \tag{A.3}$$

By differentiating now $\nabla_x e^2(\mathbf{x})$ in (A.2) with respect to $\mathbf{x}$ the Hessian is obtained and yelds:

$$\frac{\partial \nabla_{\mathbf{x}} e^2(\mathbf{x})}{\partial \mathbf{x}} = 2\,\mathbf{D}^T\mathbf{D} \tag{A.4}$$

The error is minimum, in the least squares sense, and the solution is unique if the matrix $\mathbf{D}^T\mathbf{D}$ is positive definite; in this case the Hessian matrix

2 $\mathbf{D}^T\mathbf{D}$ is therefore invertible. By pre-multiplying now left and right sides of (A.3) by $\left(\mathbf{D}^T\mathbf{D}\right)^{-1}$ eventually yields:

$$\mathbf{x} = \left(\mathbf{D}^T\mathbf{D}\right)^{-1}\mathbf{D}^T\mathbf{y} \tag{A.5}$$

A.2

The sums expressing the dot products appearing in the *core matrix* can be symbolically evaluated as:

$$
\begin{aligned}
\mathbf{c}^T\mathbf{c} = \sum_{k=0}^{N-1}\cos^2\left(2\theta\frac{k}{N}\right) &= \sum_{k=0}^{N-1}\left[\frac{1}{2} + \frac{1}{2}\cos\left(4\theta\frac{k}{N}\right)\right] \\
&= \frac{N}{2} + \frac{1}{2}\frac{\sin(2\theta)}{\sin(2\theta/N)}\cos\left(\frac{N-1}{N}2\theta\right) \quad (A.6)
\end{aligned}
$$

$$
\begin{aligned}
\mathbf{s}^T\mathbf{s} = \sum_{k=0}^{N-1}\sin^2\left(2\theta\frac{k}{N}\right) &= \sum_{k=0}^{N-1}\left[\frac{1}{2} - \frac{1}{2}\cos\left(4\theta\frac{k}{N}\right)\right] \\
&= \frac{N}{2} - \frac{1}{2}\frac{\sin(2\theta)}{\sin(2\theta/N)}\cos\left(\frac{N-1}{N}2\theta\right) \quad (A.7)
\end{aligned}
$$

$$
\begin{aligned}
\mathbf{s}^T\mathbf{c} = \mathbf{c}^T\mathbf{s} &= \sum_{k=0}^{N-1}\sin\left(2\theta\frac{k}{N}\right)\cos\left(2\theta\frac{k}{N}\right) \\
&= \sum_{k=0}^{N-1}\frac{1}{2}\sin\left(4\theta\frac{k}{N}\right) = \frac{1}{2}\frac{\sin(2\theta)}{\sin(2\theta/N)}\sin\left(\frac{N-1}{N}2\theta\right) \quad (A.8)
\end{aligned}
$$

$$
\mathbf{c}^T\mathbf{1} = \mathbf{1}^T\mathbf{c} = \sum_{k=0}^{N-1}\cos\left(2\theta\frac{k}{N}\right) = \frac{\sin(\theta)}{\sin(\theta/N)}\cos\left(\frac{N-1}{N}\theta\right) \tag{A.9}
$$

$$\mathbf{s}^T\mathbf{1} = \mathbf{1}^T\mathbf{s} = \sum_{k=0}^{N-1} \sin\left(2\theta\frac{k}{N}\right) = \frac{\sin(\theta)}{\sin(\theta/N)}\sin\left(\frac{N-1}{N}\theta\right) \tag{A.10}$$

$$\mathbf{1}^T\mathbf{1} = \sum_{k=0}^{N-1} 1 = N \tag{A.11}$$

Considering that $\sin 2\phi = 2\sin\phi\cos\phi$ it is possible to write the following equation:

$$\frac{\sin 2\theta}{\sin(2\theta/N)} = \frac{\sin\theta}{\sin(\theta/N)}\frac{\cos\theta}{\cos(\theta/N)} \tag{A.12}$$

By using the auxiliary variables introduced in (5.16) the elements of the *core matrix* can be rewritten as follows:

$$\mathbf{c}^T\mathbf{c} = \frac{N}{2} + \frac{1}{2}SC\cos 2\gamma \tag{A.13}$$

$$\mathbf{s}^T\mathbf{s} = \frac{N}{2} - \frac{1}{2}SC\cos 2\gamma \tag{A.14}$$

$$\mathbf{s}^T\mathbf{c} = \mathbf{c}^T\mathbf{s} = \frac{1}{2}SC\sin 2\gamma \tag{A.15}$$

$$\mathbf{c}^T\mathbf{1} = \mathbf{1}^T\mathbf{c} = S\cos\gamma \tag{A.16}$$

$$\mathbf{s}^T\mathbf{1} = \mathbf{1}^T\mathbf{s} = S\sin\gamma \tag{A.17}$$

The current expression of the dot products is still too complicated in order to find a symbolic expression of the eigenvalues and eigenvectors.

With the aid of the following variables:

$$\begin{cases} T = C/S \\ s = S \sin \gamma \\ c = S \cos \gamma \end{cases} \tag{A.18}$$

the *core matrix* can be symbolically expressed by the following equation.

$$\mathbf{D}^T\mathbf{D} = \begin{bmatrix} \frac{N}{2} + \frac{T}{2}(c^2 - s^2) & Tsc & c \\ Tsc & \frac{N}{2} - \frac{T}{2}(c^2 - s^2) & s \\ c & s & N \end{bmatrix} \tag{A.19}$$

Its characteristic polynomial is:

$$\begin{aligned} p(\lambda) &= \lambda^3 - 2\lambda^2 N + \left(\frac{5}{4} N^2 - \frac{1}{4} T^2 S^4 - S^2 \right) \lambda + \\ &+ \left(\frac{1}{2} S^2 + \frac{1}{4} T^2 S^4 \right) N - \frac{1}{2} S^4 T - \frac{1}{4} N^3 \end{aligned} \tag{A.20}$$

The eigenvalues, calculated by solving (A.20), after straightforward manipulations, are:

$$\begin{cases} \lambda_1 = \frac{N}{2} - \frac{TS^2}{2} \\ \lambda_2 = \frac{N}{2} + \frac{(N+TS^2) - \sqrt{(N-TS^2)^2 + 16S^2}}{4} \\ \lambda_3 = \frac{N}{2} + \frac{(N+TS^2) + \sqrt{(N-TS^2)^2 + 16S^2}}{4} \end{cases} \tag{A.21}$$

By applying again the formulas in (A.18) eventually yields (5.18); the eigenvectors can be then evaluated.

A.3

Here the properties of the eigenvalues of the *core matrix* are investigated in order to find sufficient conditions for the core matrix to be singular. It is straightforward to see that the eigenvalue λ_3 can never be smaller than the number of samples N; indeed with simple calculations the following inequality, which is always true, can be written:

$$\lambda_3 \geq N \Leftrightarrow \sqrt{(N - SC)^2 + 16S^2} \geq (N - SC) \tag{A.22}$$

This result is in accordance to the fact that $\mathbf{D}$ has to have rank equal at least to one since there is a column of elements all equal to 1.

Therefore only λ_1 and λ_2 can be equal to zero.

The case $\lambda_1 = 0$ is equivalent to the following equation:

$$SC = \frac{\sin 2\theta}{\sin (2\theta/N)} = N \tag{A.23}$$

The solutions of (A.23) can be found, remembering that $\theta = \pi (M + \alpha)$, by evaluating the following limit:

$$\lim_{(M+\alpha) \to q\frac{N}{2}} \frac{\sin 2\pi (M + \alpha)}{\sin 2\pi \frac{M+\alpha}{N}} = N \frac{\cos qN\pi}{\cos q\pi} \tag{A.24}$$

where q is a non negative integer number and l'Hopital's rule has been applied since the limit was an indeterminate form $0/0$.

The limit (A.24) is equal to N if q and N are not both odd whereas it is equal to $-N$ otherwise.

Solving the equation $\lambda_2 = 0$ is more difficult since it is equivalent to solving the following one:

$$N^2 + NSC - 2S^2 = 0 \tag{A.25}$$

In order to find the conditions for λ_2 being zero it could alternatively be noted that $\lambda_1 + \lambda_2 + \lambda_3 = 2N$ and that when both N and q are odd $\lambda_1 = N$ hence λ_2 is forced to be zero since $\lambda_3 \geq N$.

Equation (A.26) states that sufficient condition for the *core matrix* to be singular is that the number of periods recorded is an integer multiple factor

of one half of the number of samples acquired.

$$M + \alpha = q\frac{N}{2} \tag{A.26}$$

Condition (A.26) is equivalent, by means of (5.10), to the following one:

$$f_0 = q\frac{F_S}{2} \tag{A.27}$$

Bibliography

[1] Lyndon R Evans. LHC accelerator physics and technology challenges. Number LHC-Project-Report-303. CERN-LHC-Project-Report-303, page 6 p, Apr 1999.

[2] N Mokhov, J Annala, R Carrigan, M Church, A Drozhdin, T Johnson, R Reilly, V Shiltsev, G Stancari, D Still, A Valishev, X L Zhang, and V Zvoda. Tevatron beam halo collimation system: design, operational experience and new methods. *Journal of Instrumentation*, 6(08):T08005, 2011.

[3] R. W. Assmann, O. Aberle, G. Bellodi, A. Bertarelli, C. Bracco, H. Braun, M. Brugger, S. Calatroni, R. Chamizo, A. Dallocchio, B. Dehning, A. Ferrari, P. Gander, A. Grudiev, E. B. Holzer, J. B. Jeanneret, J. M. Jiménez, M. Jonker, Y. Kadi, K. Kershaw0, J. Lendaro, J. Lettry, R. Losito, M. Magistris, A. Masi, M. Mayer, E. Métral, R. Perret, C. Rathjen, S. Redaelli, G. Robert-Démolaize, S. Roesler, F. Ruggiero, M. Santana, P. Sievers, M. Sobczak, A. Tsoulou, V. Vlachoudis, T. Weiler, I. S. Baishev, and I. Kurochkin. The final collimation system for the LHC. In *10th European Particle Accelerator Conference*, page 986, Edinburgh, UK, June 2006.

[4] Luisella Lari, Leonid Rivkin, and Vasilis Vlachoudis. *Beam-Machine Interaction Studies for the Phase II LHC Collimation System. oai:cds.cern.ch:1340231*. PhD thesis, Lausanne, EPFL, Lausanne, 2010. Presented 13 Dec 2010.

[5] C Bracco, L Rivkin, and R Assmann. *Commissioning Scenarios and Tests for the LHC Collimation System. oai:cds.cern.ch:1174254*. PhD thesis, Lausanne, École Polytechnique Fédérale de Lausanne, Lausanne, 2009. Presented on 29 Jan 2009.

[6] G Robert-Démolaize and R W Assmann. *Design and Performance Optimization of the LHC Collimation System. oai:cds.cern.ch:1004869*. PhD thesis, Grenoble 1, Grenoble, 2006. Presented on 20 Nov 2006.

[7] N Catalan-Lasheras. *Transverse and Longitudinal Beam Collimation in a High-Energy Proton Collider (LHC)*. PhD thesis, Zaragoza Univ., Geneva, 1998. Presented on 16 Nov 1998.

[8] Said Hasan, Michela Prest, Walter Scandale, and Erik Vallazza. *Bent silicon crystals for the LHC collimation: Studies with an ultrarelativistic proton beam. oai:cds.cern.ch:1063071*. PhD thesis, Como Univ., Como, 2007. Presented on 16 Oct 2007.

[9] Valentina Previtali, Leonid Rivkin, and Ralph Assmann. *Performance evaluation of a crystal-enhanced collimation system for the LHC. oai:cds.cern.ch:1302274*. PhD thesis, Lausanne, École Polytechnique Fédérale de Lausanne, Lausanne, 2010. Presented on 07 Oct 2010.

[10] N V Mokhov. Beam collimation at hadron colliders. volume 693, pages 14–19, 2004.

[11] S. DeBarger, S. Metcalfe, C. Ng, T.G. Porter, J. Seeman, et al. The PEP-II movable collimators. page P1hlf04, 2001.

[12] A. Danisi. Simulation of dc interfering magnetic field effects on the LHC collimators. Master's thesis, Dept. Electron. Eng., Univ. Federico II, Naples, IT, 2009.

[13] A. Ferro. Metrological Characterization of the LHC Collimators Positioning Survey System. Master's thesis, University of Sannio, 2008.

[14] K. Ara. A differential transformer with temperature- and excitation-independent output. *IEEE Transactions on Instrumentation and Measurement*, 21(3):249–255, Aug. 1972.

[15] http://LHC-machine-outreach.web.cern.ch/LHC-machine-outreach/.

[16] J. B. Jeanneret, I. L. Ajguirei, R. W. Assmann, I. Baichev, D. I. Kaltchev, T. Kurtyka, and A. Wróblewski. Beam loss and collimation at LHC, cern-LHC-project-report-603. volume 642, pages 189–191. 6 p, Jul 2002.

[17] R. W. Assmann, I. S. Baishev, M. Brugger, L. Bruno, H. Burkhardt, G. Burtin, Bernd Dehning, C. Fischer, B. Goddard, E. Gschwendtner, M. Hayes, J. B. Jeanneret, R. Jung, V. Kain, D. I. Kaltchev, M. Lamont, R. Schmidt, Eugène B. Vossenberg, E. Weisse, and J. Wenninger. Requirements for the LHC collimation system. Number LHC-Project-Report-599. CERN-LHC-Project-Report-599, page 4 p, Jul 2002.

[18] M. Church, A.I. Drozhdin, A. Legan, N.V. Mokhov, and R. Reilly. Tevatron run-II beam collimation system. pages 56–61, 1999.

[19] A. Masi, G. Conte, R. Losito, and M. Martino. DSP-based stepping motor drivers for the LHC collimators. *IEEE Transactions on Nuclear Science*, 55(1 Part 1):341–348, 2008.

[20] M. Martino, A. Masi, R. Losito, and R. Picatoste Ruilope. Low emission, self-tunable dsp based stepping motor drive for use with arbitrarily long cables. In *Conference record of the 12th LSS symposium*, 2010.

[21] D. Still, J. Annala, M. Church, B. Hendricks, Brian J. Kramper, et al. The Tevatron Collider Run II halo removal system. *AIP Conf.Proc.*, 693:176–179, 2004.

[22] D. S. Nyce. *Linear Position Sensors*. Wiley-Intersience, Hoboken, NJ, 2004.

[23] R. Van Nieuwenhove and S. Solstad. In-core fuel performance and material characterization in the halden reactor. *IEEE Transactions on Nuclear Science*, 57(5):2683–2688, 2010.

[24] J. Marshall, J. Preble, and W. Schneider. Superconducting cavity tuner performance at cebaf. In *Proc. Particle Accelerator Conf. the 1993*, pages 1396–1398, 1993.

[25] T. Roger Billeter. Displacement measurement sensor for use in loss-of-fluid-test reactor. *IEEE Transactions on Nuclear Science*, 28(1):758–762, February 1981.

[26] S. C. Saxena and S. B. L. Seksena. A self-compensated smart LVDT transducer. *IEEE Transactions on Instrumentation and Measurement*, 38(3):748–753, June 1989.

[27] R. S. Weissbach, D. R. Loker, and R. M. Ford. Test and comparison of LVDT signal conditioner performance. In *Proc. 17th IEEE Instrumentation and Measurement Technology Conference IMTC 2000*, volume 2, pages 1143–1146, May 1–4, 2000.

[28] A. Masi, A. Brielmann, R. Losito, and M. Martino. LVDT conditioning on the LHC collimators. *IEEE Transactions on Nuclear Science*, 55(1):67–75, February 2008.

[29] J. Szczyrbak and E. D. D. Schmidt. *LVDT Signa Conditioning Techniques*. Lucas Varity, 2005.

[30] Analog Devices, Norwood, MA. *Universal LVDT Signal Conditioner - AD698 Application Note*, 1995.

[31] R. M. Ford, R. S. Weissbach, and D. R. Loker. A dsp-based modified costas receiver for lvdt position sensors. In *Proc. 17th IEEE Instrumentation and Measurement Technology Conf. IMTC 2000*, volume 3, pages 1448–1452, 2000.

[32] Analog Devices, Norwood, MA. *LVDT signal conditioner - AD598 Application Note*, 1989.

[33] R. S. Weissbach, D. R. Loker, and R. M. Ford. Test and comparison of lvdt signal conditioner performance. In *Proc. 17th IEEE Instrumentation and Measurement Technology Conf. IMTC 2000*, volume 2, pages 1143–1146, 2000.

[34] D. Crescini, A. Flammini, D. Marioli, and A. Taroni. Application of an fft-based algorithm to signal processing of lvdt position sensors. *IEEE T Instrum Meas*, 47(5):1119–1123, 1998.

[35] A. Masi and R. Losito. LHC collimators low level control system. *IEEE Transactions on Nuclear Science*, 55(1):333–340, February 2008.

[36] IEEE Standard for Terminology and Test Methods for Analog-To-Digital Converters, 2001.

[37] P. Arpaia, F. Cennamo, and P. Daponte. Metrological characterisation of analog-to-digital converters-a state of the art. In *Proc. Third Int Advanced A/D and D/A Conversion Techniques and Their Applications Conf. (Conf. Publ. No. 466)*, pages 134–144, 1999.

[38] F. C. Alegria and A. C. Serra. Uncertainty of the estimates of sine wave fitting of digital data in the presence of additive noise. In *Proc. IEEE Instrumentation and Measurement Technology Conference IMTC 2006*, pages 1643–1647, 24–27 April 2006.

[39] T. Andersson and P. Handel. IEEE Standard 1057, Cramer-Rao bound and the parsimony principle. *IEEE Transactions on Instrumentation and Measurement*, 55(1):44–53, Feb. 2006.

[40] F. C. Alegria. Bias of amplitude estimation using three-parameter sine fitting in the presence of additive noise. *Measurement*, 42:748–756, 2009.

[41] Shang-Teh Wu and Jyun-Lang Hong. Five-point amplitude estimation of sinusoidal signals: With application to LVDT signal conditioning. *IEEE Transactions on Instrumentation and Measurement*, 59(3):623–630, 2010.

[42] P. Handel. Amplitude estimation using IEEE-STD-1057 three-parameter sine wave fit: Statistical distribution, bias and variance. *Measurement*, 43(6):766–770, July 2010.

[43] Eliakim Hastings Moore. On the reciprocal of the general algebraic matrix. *Bulletin of the American Mathematical Society*, pages 394–395, 1920.

[44] R. Penrose. A generalized inverse for matrices. *Mathematical Proceedings of the Cambridge Philosophical Society*, 51(03):406–413, 1955.

[45] Athanasios Papoulis. *Probability, Random Variables and Stochastic Processes*. McGraw-Hill Companies, 3rd edition, February 1991.

[46] M. Bertocco, C. Narduzzi, P. Paglierani, and D. Petri. A noise model for digitized data. *IEEE Transactions on Instrumentation and Measurement*, 49(1):83–86, Feb. 2000.

[47] F W J Olver. *Handbook of Mathematical Functions: with Formulas, Graphs, and Mathematical Tables*. Dover books on mathematics. Dover Publications, 1 edition, June 1965.

[48] M. Martino, A. Danisi, R. Losito, A. Masi, and G. Spiezia. Design of a linear variable differential transformer with high rejection to external interfering magnetic field. *IEEE Transactions on Magnetics*, 46(2):674–677, February 2010.

[49] Giorgio Bertotti. *Hysteresis in Magnetism for physiscists, material scientists, and engineers*. Academic Press, 1998.

[50] A. Masi, A. Danisi, R. Losito, M. Martino, and G. Spiezia. Study of magnetic interference on a LVDT prototype. In *IEEE International Instrumentation and Measurement Technology Conference*, Austin, Tx, May 3–6 2010.

[51] S. Marshall. An analytic model for the fluxgate magnetometer. *IEEE Transactions on Magnetics*, 3(3):459–463, Sep 1967.

[52] R. F. Elfant. Approximations for the demagnetizing factors of hollow cylinders represented by confocal hollow prolate spheroids. *IEEE Transactions on Electronic Computers*, (6):789, 1962.

[53] CEDRAT, Meylan, FR. *Flux 9 2D/3D Applications Users Guide*, 2006.

[54] J. K. Sykulski, E. Sykulska, and S. T. Hughes. Application of finite element modelling in LVDT design. *COMPEL*, 11:73–76, 1992.

[55] M. Repetto and J. Simkin. Engineering analysis for design optimization of differential transformers. *IEEE Comput.-Aided Eng. J.*, 5(2):51–53, April 1988.

[56] M. Krizek and P. Neittaanmaki. *Mathematical and Numerical Modelling in Electrical Engineering: Theory and Applications*. Kluwer Academic Publishers, 1996.

[57] I. K. Kang, H. H. Scholefield, and A. P. Martin. Some concepts concerning the new high-permeability 50–50 nickel—iron alloys. *Journal of Applied Physics*, 38(3):1178–1183, 1967.

[58] F. F. Yassa and S. L. Garverick. A multichannel digital demodulator for LVDT/RVDT position sensors. *IEEE Journal of Solid-State Circuits*, 25(2):441–450, 1990.

[59] G. Novacek. Accurate linear measurement using LVDTs. *Circuit Cellar Ink*, (106):20–27, May 1999.

[60] D. Crescini, A. Flammini, D. Marioli, and A. Taroni. Application of an fft-based algorithm to signal processing of LVDT position sensors. *IEEE Transactions on Instrumentation and Measurement*, 47(5):1119–1123, Oct. 1998.

[61] G. Spiezia, R. Losito, M. Martino, A. Masi, and A. Pierno. Automatic test bench for the measurement of the magnetic interference on LVDTs. In *IEEE International Instrumentation and Measurement Technology Conference*, Austin, Tx, May 3–6 2010.

[62] K. Hoselitz. *Ferromagnetic properties of Metals and Alloys.* Oxford Univ. Press, Clarendon Press (Oxford), GB, 1952.

[63] S. Wu, S. Mo, and B. Wu. An LVDT–based self–actuating displacement transducer. *Sensors Actuators A*, 141(2):558–564, February 2008.

[64] The when, why and how of magnetic shielding. Westinghouse Designers Handbook, Blairsville, PA, 1966.

[65] *Metals Handbook*, volume 1. ASM International, 10 edition, 1990.

[66] A. Eisinberg and G. Fedele. Describing function-based analysis of a class of pwm feedback control systems. In *Proceedings of the 25th IASTED international conference on Modeling, indentification, and control*, pages 49–54, Anaheim, CA, USA, 2006. ACTA Press.

[67] G. Spiezia, R. Losito, M. Martino, A. Masi, and A. Pierno. Automatic test bench for measurement of magnetic interference on LVDTs. *IEEE Transactions on Instrumentation and Measurement*, 60(5):1802–1810, 2011.

[68] M. Martino, G. Golluccio, R. Losito, and A. Masi. An analytical model of the effect of external dc magnetic fields on the ac voltages of an LVDT. In *IEEE International Instrumentation and Measurement Technology Conference*, Austin, Tx, May 3–6 2010.

[69] R.M. Bozorth. *Ferromagnetism*. IEEE Press Classic Reissue. IEEE Press, 1993.

[70] S Redaelli and A Masi. Operational experience and performance of the LHC collimator control system. Technical Report CERN-ATS-2011-180, CERN, Geneva, Sep 2011.

[71] S Redaelli, R Assmann, A Masi, and R Losito. Final implementation and performance of the LHC Collimator Control System. oai:cds.cern.ch:1211049. Number CERN-ATS-2009-065, page 4 p, May 2009.

[72] A. Masi, R. Losito, and S. Redaelli. Measured performance of the LHC collimators low level control system. In *12th ICALEPCS Int. Conf. Accelerator Large Expt. Phys. Control Syst.*, Kobe, Japan, 2009.